2019

Investigations of augmented heat transfer due to elastic instabilities within low-inertia flows with streamline curvature

Mengying Su

INVESTIGATIONS OF AUGMENTED HEAT TRANSFER DUE TO ELASTIC INSTABILITIES WITHIN LOW-INERTIA FLOWS WITH STREAMLINE CURVATURE

by

MENGYING SU

A DISSERTATION

Submitted in partial fulfillment of the requirements
for the degree of Doctor of Philosophy
in
The Department of Mechanical and Aerospace Engineering
to
The school of Graduate Studies
of
The University of Alabama in Huntsvile

HUNTSVILLE, ALABAMA

2019

In presenting this thesis in partial fulfillment of the requirements for a doctoral degree from The University of Alabama in Huntsville, I agree that the Library of this University shall make it freely available for inspection. I further agree that permission for extensive copying for scholarly purposes may be granted by my advisor or, in his/her absence, by the Chair of the Department or the Dean of the School of Graduate Studies. It is also understood that due recognition shall be given to me and to The University of Alabama in Huntsville in any scholarly use which may be made of any material in this dissertation.

Ningying Su
(student signature)

05/28/2019
(date)

DISSERTATION APPROVAL FORM

Submitted by Mengying Su in partial fulfillment of the requirements for the degree of Doctor of Philosophy in Mechanical Engineering and accepted on behalf of the Faculty of the School of Graduate Studies by the dissertation committee.

We, the undersigned members of the Graduate Faculty of The University of Alabama in Huntsville, certify that we have advised and/or supervised the candidate on the work described in this dissertation. We further certify that we have reviewed the dissertation manuscript and approve it in partial fulfillment of the requirements for the degree of Doctor of Philosophy in Mechanical Engineering.

05-28-2019

Dr. Phillip Ligrani — Committee Chair (Date)

Dr. Jason Cassibry

Dr. Robert Frederick

Dr. Sarma Rani

Dr. Babak Shotorban

Dr. Keith Hollingsworth — Department Chair

Dr. Shankar Mahalingam — College Dean

Dr. David Berkowitz — Graduate Dean

ABSTRACT
The School of Graduate Studies
The University of Alabama in Huntsville

Degree Doctor of Philosophy College/Dept. Mechanical and Aerospace Engineering

Name of Candidate Mengying Su

Title Investigation of augmented heat transfer due to elastic instabilities within low-inertia flows with streamline curvature

The present investigation considers thermal transport variations from the presence of elastic instabilities within internal flows. A miniature Viscous Disk Pump (VDP) and a Couette Rotating Flow (RCF) environment are utilized to investigate flow and heat transfer characteristics for very low Reynolds numbers. The viscous disk pump heat transfer results are based upon energy balance measurements which utilize the mixed-mean temperature at the inlet and outlet of the VDP flow passage. The overall heat transfer rate is determined based upon a constant surface temperature thermal boundary condition, and upon a log-mean-temperature difference approach. Significant enhancements of mixing and transport are observed, which are associated with the onset and development of elastic instabilities. Such behavior is verified, relative to Newtonian Boger fluid solvents, using flow visualization results, pressure rise data, overall shear stress variations, increases of overall magnitudes of convective Nusselt numbers, increases of time-averaged magnitudes of mean-square temperature fluctuations, and increases of spectral energy content of unsteady temperature fluctuations. Results associated with RCF are presented which further demonstrate the remarkable ability of viscoelastic fluids to augment surface heat transfer characteristics. With this flow arrangement, the overall heat transfer rate is determined based upon a constant surface heat flux thermal boundary condition. Flow visualization results and Nusselt number data show that the onset of what is believed to be elastic instabilities is well represented using a constant Weissenberg number of 30 criterion. Variations of normalized and time-averaged magnitudes of the mean-square of flow static temperature fluctuations are also consistent with this criterion, since those values also increase substantially as Weissenberg number becomes greater than 30. Power spectral distributions of static temperature fluctuations, for the highest polymer concentrations and highest disk rotation speeds and the same experimental conditions, show broad-band characteristics, with continuous power content present at frequencies from just greater than 0.01 Hz to values of approximately 1 Hz. These spectral distributions are as much as three orders of magnitude higher than distributions which are associated either with the sucrose solvent flow, where ρ=0 ppm, or when no rotation is present and ω=0 rad/s. Magnitudes of Nusselt number enhancement, associated with increased polymer concentration and increased shear rate, are as high as 3.0, compared to zero shear rate values (obtained with zero rotation), which are in the vicinity of 1.0.

Abstract Approval: Committee Chair

Dr. Phillip Ingrani

Department Chair

Dr. Keith Hollingsworth

Graduate Dean

Dr. David Berkowitz

ACKNOWLEDGMENTS

Firstly, I would like to express my sincere gratitude to my advisor Prof. Phillip Ligrani for the professional and detailed advices on my doctoral dissertation and research conduction. On a personal level, I am inspired by his careful, meticulous, and persistent altitude, which would be life-long beneficial qualities for me.

I would also thank the rest of my committee members (Dr. Cassibry, Dr. Frederick, Dr. Rani and Dr. Shotorban) for the valuable advices on my dissertation. I would thank my friends and lab mates for their continuous support and making my research life exciting and fun.

Last but not least, I would like to thank my parents, my uncles and aunts, and my cousins for their endless love and supporting.

TABLE OF CONTENTS

List of Figures

Figure Page

List of Tables

Table Page

List of Symbols

a	index to predict viscosity
A	area
A_i	area associated with thermocouple
A_0	maximum mixing length
c	concentration of polymer solution/heat capacity
C_o	initial local dye concentration at t=0 and r=0
$C_{r,t}$	local dye concentration
C_p	heat capacity
d	diameter
D	portion of the C-shape channel perimeter where the constant temperature boundary condition is applied
Deb	Deborah number
f	frequency
F	parameter in Zimm equation, which is 0.5313
g	Mixing/diffusion rate
Gz	Graetz number
G'	elastic modulus
G''	loss modulus
h	heat transfer coefficient
H	flow passage height
i	summation notation
I	current
k	thermal conductivity
K_f	thermal conductivity of fluid
K_p	thermal conductivity of polystyrene
K_s	thermal conductivity of styrofoam
L	characteristic length of C-shape channel
L_c	characteristic length, gap height of flow passage
L_{ht}	heater thickness
L_p	thickness of the polystyrene plate
L_{pb}	distance between bottom thermocouple and bottom of polystyrene
L_{pt}	distance between top thermocouple and top of polystyrene
L_s	thickness of the Styrofoam insulation
L_{tb}	distance between bottom thermocouple and bottom of heater
L_{tt}	distance between top thermocouple and top of heater
$\dot{m}$	mass flow rate
M_{cirt}	critical transition parameter
M_w	Polymer molecular weight
n	power law coefficient/index
N	summation notation
Nu	local Nusselt number
Nu_s	Nusselt number associated with sucrose solvent flow

$\overline{\overline{Nu}}$	spatially-averaged Nusselt number
p	associated to polymer
P	power/ channel perimeter
Pr	Prandtl number
ΔP	pressure difference
$\dot{q}$	heat flux into VDP
q_{disk}	heat loss through disk
q_{bot}	heat flux lost to environment
q_{top}	heat flux entering flow
Q	Dimensional volumetric flow rate
r	radical coordinate
r_d	dye front radical coordinate location
R	gas constant/radius
Re	Reynolds number
R_1	outer radius of disk, and thermo-foil heater radius/ inner radius of C-shape channel
R_2	inner radius of cup flow container/outer radius of C-shape channel
R_3	outer radius of rotating shaft
s	gap height of C-shape channel/associated to solvent
$S^2(f)$	spectral temperature power per until Hertz
t	time
$\overline{t'^2}$	mean square of temperature fluctuation
$\overline{t'^2_s}$	mean square of temperature fluctuation associated with solvent flow
T	Absolute static temperature
T_f	local fluid temperature at thermocouple location
T_{hb}	temperature at the bottom surface of heater
T_{ht}	temperature at the bottom surface of heater
T_{in}	inlet temperature
T_{out}	outlet temperature
T_{air}	ambient temperature
T_t	thermocouple recovery temperature
T_s	static temperature
T_t	temperature at surface of polystyrene plate adjacent to the flow
U	streamwise fluid velocity at mean radius
v	flow velocity
V	voltage/velocity
Wi	Weissenberg number
x	first lateral coordinate
y	second lateral coordinate
z	third lateral coordinate

Greek symbols

β	$\mu_s/\ \mu_{o;}\ D_{eff}/(dA/dt)$
$\dot{\gamma}$	shear rate
γ_o	strain
τ'_o	stress associated to storage moduli

τ_{11}	tensile stress is estimated using the Oldroyd-B model
τ_o''	stress associated to loss moduli
μ	viscosity parameter in McKinley equation
η	viscosity
η'	viscosity associated to storage moduli
η''	viscosity associated to loss moduli
$\lvert\eta^*\rvert$	complex viscosity
η_s	viscosity associated to solvent
η_o	viscosity at zero shear rate
η_{spo}	Specific zero-shear viscosity
η_∞	viscosity at infinite shear rate
$[\eta]$	intrinsic viscosity
σ	shear stress
ρ	fluid density
ρ_s	density associated to solvent
λ	polymer relaxation time
λ_{CY}	the inverse shear rate at the onset of shear-thinning behavior
ν	dimensionless scaling exponent
ω	rotation speed in rad/s
Ω	rotation speed in RPM

CHAPTER 1

INTRODUCTION

1.1 Overview

Recent advances in electronics cooling, bioengineering, and biomedical engineering, which involve fluid flows within microscale and millimeter-scale passages, require control and augmentation of mass, momentum, and thermal transport levels. However, numerous challenges are inherent to implementing enhancements of these quantities within such small-scale environments, where length scales are very small, flows are generally laminar, local fluid shear rates are augmented, and local Reynolds numbers are on the order of 1. One solution, which is gaining increasing attention, is through the implementation and use of elastic turbulence.

Elastic turbulence is generally believed to occur subsequent to the development of elastic instability (Muller, 1989; Larson et al., 1990, 1992; Shaqfeh, 1996). Grosiman and Steinberg (2000, 2004) describe elastic turbulence flow for a polymer solution at low Reynolds number within a swirling flow between two disks. Elastic turbulence is determined by the appearance of three main features, including large-scale temporal and spatial fluid motions, significant increases in momentum and mass transfer, and appropriate characteristic scales of time and space within the flow. According to Qin et

al. (2019a), elastic turbulence exhibits features similar to Newtonian turbulence, including power-law behavior in velocity spectra, intermittent flow statistics, and irregular velocity structures. Fouxon et al. (2003) discuss spectra of elastic turbulence at small Reynolds numbers, with different power-like behavior for elastic turbulence, relative to inertial turbulence.

Elastic turbulence is associated with local flow instabilities which develop at very low Reynolds numbers, within non-Newtonian viscoelastic fluids. The phenomenon is characterized by increased local mixing and secondary flows, which are believed to develop due to local stretching and deformation of long-chain polymers, such as polyacrylamide, which are distributed throughout the viscoelastic fluid. Such polymer activity is initiated by subjecting them to local strain, which is induced by streamline curvature, or local flow velocity gradients, which result in velocity gradients normal to flow streamlines. It is important to note that such ideas are currently, partly hypothetical, because the associated polymer motions have only been observed on a microscopic level for a limited range of experimental conditions (Liu and Steinberg, 2010; Bonn et al., 2011; Tai et al., 2015). Existing theories indicate that the resulting, local polymer stretching then leads to a microscopic phenomenon called “coil stretch transition” (De Gennes, 1974; Burghelea et al., 2007). According to Burghelea et al. (2007), this occurs when the polymer molecules are strongly stretched to sizes which approximate the total polymer length. Transition then develops as the stretch rate exceeds the inverse polymer relaxation time. When this occurs, Burghelea et al. (2007), indicates that “most of the molecules are strongly stretched to sizes up to the order of the total polymer length, since stretching is limited only by nonlinear effects and back reaction of the flow. There is an

abrupt change in the polymer conformation occurring at large stretching rates, called the coil-stretch transition. The transition has remarkable macroscopic consequences." In addition, "the elasticity of the polymers itself (which manifests itself above the coil-stretch transition) is a source of nonlinearity. This explains how a chaotic state, which requires a high level of nonlinearity, can arise even at low Re in elastic turbulence." (Burghelea et al., 2007). As such, the "coupling" between the primary shear flow and the secondary polymer elongation flow is a key ingredient. Relevant theoretical descriptions from these sources (De Gennes, 1974; Burghelea et al., 2007) thus include polymer feedback to and from the surrounding flow, and to and from surrounding polymers. This leads to non-uniform distributions of elastic stresses, and additional polymer stretching, as well as enhanced development of strongly non-linear, non-Newtonian flow behavior (Burghelea et al., 2007).

The stretch rate condition is then also the basis of the definition of the Weissenberg number, Wi. This is because elastic turbulence phenomena occurs when polymer extensibility and deformation lead to a sufficient growth in the local elastic stress, a sequence of events referred to as the Weissenberg instability. This instability occurs when the Weissenberg number is greater than an onset value which depends upon experimental configuration, shear rate, polymer type, polymer concentration, and other parameters (Groisman and Steinberg, 2000, 2004). If the elastic response is slow in comparison with the stretch rate for larger velocity gradients (for example, when Weissenberg number is larger than one), the polymer is substantially stretched and elongated, which leads to a sharp growth in stress (Balkovsky et al., 2001). According to Qin et al. (2019a), elastic turbulence is different from Newtonian turbulence as it occurs

at low Reynolds numbers, with negligible inertia effects far below the dissipation scale, with polymer addition that suppresses eddies. Onset of elastic instabilities and elastic turbulence is attributed to elastic stress growth. The associated stress growth then results in highly non-linear and non-Newtonian behavior, increased local secondary flows, increased mixing, and locally chaotic fluid motions. Elastic instabilities and elastic turbulence occur in pipe flows, and channel flows, often at locations with streamwise curvature, which must be sufficient to sustain flow instabilities as it advects downstream. According to Li et al. (2017), "elastic turbulence ….. provides a great potential for the heat removal in the wide microfluidic applications."

1.2 Present Investigation

Within the present investigation, the influences of elastic turbulence on convective heat transfer, within a C-shaped passage of a Viscous Disk Pump (VDP) and a Rotating Couette Flow (RCF) environment, are investigated experimentally, as different magnitudes of shear stress and strain rate are imposed upon the flow field. The Viscous Disk Pump consists of a C-shape channel with a fluid inlet port and a fluid outlet port, which are located at opposite ends of the C-shaped flow channel. The viscous disk pump is utilized because it produces easily controlled flow rates and pressure rises. Reynolds numbers, based upon flow passage gap height and spatially-averaged velocity, range from 0.03 to 0.24, and Weissenberg numbers range from 42.5 to 2213.5. Elasticity numbers, El=Wi/Re, range from 1415 to 35134. Rotating Couette Flow includes an adjustable rotating disk, locating within a cylindrical cup flow container. Rotating Couette Flow is employed because the magnitude of shear rate is easily set by rotational speed and flow passage height. Corresponding Reynolds numbers, based upon flow passage gap height

and spatially-averaged velocity, range from 0.39 to 2.83, and Weissenberg numbers range from 8.9 to 89.7. Elasticity numbers, El=Wi/Re, range from 13.5 to 57.0. Transition and development of elastic instability and elastic turbulence are characterized, along with convective heat transfer enhancements. The resulting increased levels of mixing, transport, and diffusion from elastic instabilities give convective heat transfer coefficient enhancements which are substantial, relative to the Boger fluids at the same shear rate, rotation speed, flow passage height, and flow temperature. Variations of spectra of static temperature fluctuations, and mean-square magnitudes of fluctuating static temperature provide evidence of increased flow irregularities and unsteadiness (relative to Boger solution flows), which result from nonlinearly stress increases due to the polymer stretching and elongation.

Such data are valuable for the design of compact electronic and biomedical models and codes, as well as different analytic elastic turbulence transition models. As such, the present investigation considers the viability of different models as they represent the transition experimental conditions. With the present RCF arrangement, the overall heat transfer rate is determined based upon a constant surface heat flux thermal boundary condition. Within the present VDP arrangement, the overall heat transfer rate is determined based upon a constant surface temperature thermal boundary condition. Included are flow visualization results, and spectral analysis of flow static temperature fluctuations. Overall, substantially enhanced surface heat transfer coefficients and Nusselt numbers, due to elastic instability and elastic turbulence, are illustrated by the data. Note that the inertia effect are generally negligible or are very small for both the Viscous Disk Pump and the Rotating Couette Flow environments. The present investigation thus

provides new insight into the mechanisms of heat transfer and thermal transport associated with elastic instabilities and elastic turbulence, within environments which have never before been employed for this purpose.

1.3 Literature Survey

1.3.1 Elastic instabilities

Several studies consider the onset and the development of elastic instabilities. Of elastic instability studies, Larson et al. (1990, 1992) describe non-inertial viscoelastic instabilities in a Taylor-Couette flow with dilute polymer solutions. Shaqfeh (1996) shows that elastic instabilities are present within a wide range of flows. Larson et al. (1990) indicate that elastic instability depends on Deborah number and polymer solution, which was later confirmed experimentally by Grosiman and Steinberg (1998) using a Couette-Taylor system. The experimental effort undertaken by Larson et al. (1990) shows onset of elastic instability using a 1000 ppm polymer solution within Taylor-Couette flow. Interactions between the velocity fluctuation and the first normal stress are believed to be the driving force for the instabilities. Shaqfeh (1996) measures fluid viscometric parameters for pure elastic flow instabilities. Results indicate that polymer fluids can create bifurcation. McKinley et al. (1996) characterize the onset of pure elastic instabilities for different geometries. A dimensionless criterion, M_{crit}, is proposed to quantity the onset of pure elastic instabilities, which combines the kinetic and dynamic factors, as well as geometry influences for curvature flows. Pathak et al. (2004) consider purely elastic instability for a Poiseuille flow path, based on flow visualizations. Resulting data show that tracer partials are radially displaced and mixing is promoted, compared to Newtonian fluids. Pathak et al. (2004) indicate that augmented mixing gives

enhanced secondary flows, which promote instabilities within configurations with curved streamlines.

1.3.2 Fluid mechanics investigations involving significant streamline curvature

Most investigations characterize elastic turbulence in geometries with curved streamlines, as a variety of flow characteristics are considered. Naschie et al. (1992) observe aspects of diffusion and turbulence-like behavior in fluids from numerical predictions. Berti et al. (2008) predict elastic turbulence characteristics numerically using the Oldroyd-B model in a two-dimensional Kolmogorov flow. The numerical results show reasonable agreement with experimental data. Grosiman and Steinberg (2000, 2004) present experimental observations of elasticity-induced turbulence in flows between two rotating disks. Observations are provided of fluid motions over a broad range of spatial and temporal scales, with significant increases in momentum and mass transfer at low Reynolds numbers and Weissenberg number values larger than 1. According to these investigations, transition to elastic turbulence is induced by non-linear elasticity effects.

Burghelea et al. (2007) present results regarding structure of the velocity field within von Karmon swirling flow between two disks. According to Burghelea et al. (2004, 2007), when elastic turbulence is present in a microscopic flow, the mixing time is three to four orders of magnitude shorter compared to molecular diffusion. In addition, a wide range of length scales are excited, and significant increases in mass and momentum transport rates are present, which are equivalent to levels associated with inertial turbulence. Schiamberg et al. (2006) investigate transition to elastic turbulence within torsional parallel-plate flow. The experimental effort employs flow between rotating and

stationary disks, wherein a complex sequence of events are observed, as the flow transits from laminar behavior to elastic turbulence. According to these investigations, a rich series of secondary flow states are observed connecting simple torsional shearing flow to 'elastic turbulence', with negligible inertia. Oscillations are produced by secondary flows, which lead to chaotic flow, and then to elastic turbulence flow. Observations are made as shear stress or shear rate are incrementally increased and then held constant, which include circular and spiral roll fluid motions, as well as a progression of events from 'chaotic' flow to periodic flow to elastic turbulence flow.

Jun and Steinberg (2009) consider frequency spectral variations of pressure fluctuations within elastic turbulence flows with different polymer concentrations. Results show that spectral variations are only weakly dependent upon polymer concentration, and often resemble statistical characteristics of inertial turbulence. Another investigation using a curvilinear channel by Jun and Steinberg (2011) reveals non-uniform distributions of elastic stresses, which may be injected into the bulk fluid. Li et al. (2007, 2010) observe viscoelastic fluid instabilities and elastic turbulence within cylindrical swirling flows and microchannel flows, with curvilinear streamlines, as high-molecular-weight polymers are employed. Described are a variety of asymmetrical flow structures, as well as time-dependent vortical motions. Burnishev et al. (2014) investigate on the effects of polymer additives within von Karman swirling flows. Considered are static pressure power spectra with elastic turbulence, with frequency variations associated with different vortex structures.

1.3.3 Fluid Mechanics investigations involving other flow configurations

A few studies investigate transition and effective diffusion, and related flow phenomenon, associated with elastic instabilities and elastic turbulence, within straight channel configurations, and within channels without significant streamwise curvature. Associated theoretical investigations show that bifurcations and perturbation growth (from elastic instabilities) can arise from linearly stable solutions. Predicted results are generally consistent with experimental measurements in channel flows with cylinders, which perturb the flow. With the resulting perturbations, large velocity fluctuations and irregular flow variations are activated at large scales, which are long-lived (Qin et al., 2019a). Using numerical predictions, Meulenbroke et al. (2004) and Bertola et al. (2003) observe a non-linear subcritical instability within Poiseuille flows. The non-linear instability is confirmed by analysis, and is associated with augmentation of normal stress levels. A purely elastic subcritical instability is observed at a very small Reynold numbers within plane Couette flows by Morozov and Saarloos (2004, 2007). Results show that small perturbations are sufficient to result in secondary flows, for Weissenberg numbers greater than a critical value, as a consequence of self-enhancement of stretched polymers. Gan et al. (2006) employ polymer solutions within a microchannel with an abrupt contraction ratio of 8. With this configuration, flow instabilities are triggered, which lead to effective mixing and elastic turbulence at low Reynold numbers, with negligible diffusion and inertial effects.

Pan et al. (2013) present experimental results considering nonlinear instability in a long, straight microchannel with flow disturbances created near the entrance of the channel. Observations are made as a sudden onset of large velocity fluctuations when the

flow rates and perturbation magnitudes cross a critical value, indicating the presence of a non-linear subcritical instability. According to the authors, results verify the development of elastic instabilities of polymer solution flows, provided flow rates are sufficiently high. Arratia et al. (2006) consider elastic instabilities within a cross-channel flows, in the absence of inertia. Gan et al. (2007) and Lam et al. (2009) investigate mixing of two-fluid streams using glycerol-water based polymer solutions, using a convergent/divergent channel geometry. Mixing enhancements of two dissimilar viscoelastic fluids are also achieved with negligible diffusion and inertia influences. Gan et al. (2007) indicate that the increased mixing is due to elastic instabilities. A cross-slot device is employed to investigate elastic instabilities and elastic turbulence development by Sausa et al. (2018). According to these investigations, complex flow patterns are observed with increasing Weissenberg number, which lead to elastic turbulence.

Qin et al. (2019a) investigate viscoelastic fluids in channel flows at low Reynolds numbers. These investigators observe elastic instabilities both upstream and downstream of cylindrical obstacles above threshold Weissenberg numbers. As this occurs, flow velocity and pressure fluctuations exhibit modulations normal to the mean flow direction, evidencing onset of elastic instabilities. A transitional regime of behavior, where friction factor is proportional to Weissenberg number, and a turbulent regime of behavior, with friction factor reductions as Weissenberg number increases, are also observed. Another investigation by Qin et al. (2019b) considers viscoelastic flows around a single cylinder within a channel. Three-dimensional holographic particle velocimetry results show that upstream instabilities increase with flow rate, and propagate upstream by means of elastic instabilities, providing that Weissenberg number is above a critical value.

Tai et al. (2019) employ a 3-stream micro-channel flow configuration. According to these investigations, the presence of different power law dependence (over different frequency ranges) within velocity power spectra reveals the existence of elastic turbulence. Overall consequences include increased polymer viscosity, in some cases, by up to 3 orders of magnitude. Such polymer flows are characterized by multiple time scales, including λ, the polymer relaxation time, as well as other parameters related to elastic deformation.

1.3.4 Investigations with observations of polymer motions

Additional experiments visualize polymer motions and extensions in viscoelastic flows. Liu and Steinberg (2010b) investigate polymer stretching from shear, including the effects of increasing shear rate on polymer extensions. Results indicate that the majority of polymers are stretched in an angular direction relative to the shear plane. These investigators (Liu and Steinberg (2010a)) also study polymer stretching in elastic turbulence by visualizing polymer solutions with fluorescently stained T4 DNA molecules. An epi-fluorescent microscope is utilized to monitor the DNA molecules, with image capture using a CCD camera. The probability distribution of polymer extension at different Weissenberg numbers and different concentrations are measured based upon samples of 1000 molecules. According to these investigations, results show that elastic turbulence is not based upon feedback reactions between linearly stretched polymers. In addition, the local Weissenberg number is the only relevant quantity to characterize elastic stress.

Bonn et al. (2011) visualize polymer motions and conformations within pipe flow at low Reynolds numbers, also by seeding polymer solutions with fluorescent T4 DNA

molecules. Increased levels of velocity fluctuations are observed within polymer solutions, relative to control glycerol solutions, such that fluctuations decay with streamwise development at small Weissenberg numbers, but continue to be maintained with streamwise development at higher Weissenberg numbers. Also observed are significant polymer stretching and elongations. As such, the effect of polymer elongation depends upon local shear rate magnitude, and Weissenberg number. Results for some conditions show that polymers can be elongated as much as 50 percent of their initial length. The investigations also indicate that elastic stresses from elongation lead to ealstic turbulence, and that a prerequisite for elastic turbulence is a large initial perturbation.

Tai et al. (2015) employ high speed videography to observe extension and relaxation of polymer molecules within a 3-stream contraction-expansion micro-channel arrangement. The polymer molecules are tagged with fluorescein, which is visible using illumination at an appropriate wavelength. The authors observe that polymer molecule aspect ratio decreases significantly at certain experimental conditions, indicating strong polymer molecule stretching. Subsequent releases of elastic energy between individual polymer molecules then results in instabilities and elastic turbulence. Such release of elastic stress increases with flow rate, due to the larger extensional stress magnitudes. Results also demonstrate that inhomogeneity in polymer solutions is caused by non-uniform release of energy by stretched polymer molecules as a result of molecular aggregation.

A three-dimensional measurement approach issued by Li et al. (2016) to investigate three-dimensional structure of viscoelastic flows within curved microchannels. Solutions are seeded with fluorescent beads. Confocal-micro-partial-

image velocimetry results show that polymers oscillate and are twisted, evidencing unique features of elastic turbulence. Three-dimensional temporal positions of the polymer tracers, including local polymer elongations, are detected. Results show repeated polymer stretching events, with feedback and interactions between different flow regions, which excite local flow irregularities.

1.3.5 Thermal transport and heat transfer investigations

A few recent studies also consider enhancement of thermal transport and convective heat transfer associated with elastic instabilities and elastic turbulence. Note that only a small number of different configurations are considered, over very small ranges of experimental conditions. Hartnett and Kostic (1985) and Hartnett (1992) investigate heat transfer within viscoelastic aqueous polymer solutions in channel flows. Results indicate that viscoelastic fluids exhibit enhanced heat transfer coefficients, which are attributed to secondary motions associated with local and global normal stress variations. Whalley et al. (2015) describe an investigation which utilizes a serpentine channel. According to these investigators, convective heat transfer enhancements are as large as 200 to 380 percent, compared to Boger solution results, for solutions with relatively low concentrations of polymers and relatively high concentrations of sucrose. Traore et al. (2015) describe increases in heat transfer efficiency within von Karman swirling flows due to elastic turbulence. Results illustrate efficient heat transport at very low Reynolds numbers. More recently, Abed et al. (2016) describe rheological properties of dilute polymer solutions, as they are contained within glycerine Newtonian solvents, which are shear-thinning as shear rate varies, and within sucrose solvents, which are solutions with approximately constant-viscosity as shear rate varies. Such constant-

viscosity, dilute polymer solutions are viscoelastic, and are referred to as Boger fluids (James, 2009). Abed et al. (2016) also consider relaxation time, zero-shear viscosity, and first normal stress polymer solution data, along with different flow and thermal characteristics, which are measured within an instrumented millimeter-scale serpentine duct. Of particular importance are ratios of polymer solution Nusselt number and Newtonian flow Nusselt number, which increase substantially as Weissenberg number increases from 0 to values as high as 210. Li et al. (2017) measure Nusselt number variations within a serpentine microchannel with square flow cross section, with each side length equal to 200 μm. Substantial surface Nusselt number increases are observed, with values as high as 11, when polyacrylamide solutions are employed, as compared to values measured with Newtonian, sucrose solutions, where Nusselt numbers are approximately equal to 0.344. Also presented are numerically predicted distributions of flow and thermal characteristics, which are provided over flow cross-sectional planes. Another recent investigation by Ligrani et al. (2018) report surface heat transfer augmentations as large as 240 percent, relative to sucrose solvent flows, when compared at the same shear rate, rotation speed, flow passage height, and flow temperature, for a viscous disk pump arrangement.

1.4 Present Experimental Approach

The present investigation provides new insight into the mechanisms of viscoelastic flows, and the conditions at which it occurs, as well as the effects on convective heat transfer, within environments which have never before been employed for this purpose.

Within the present investigation, two different geometries, a miniature Viscous Disk Pump (VDP) and a Rotating Couette Flow (RCF), are utilized for experimental study of the effects of elastic instabilities and elastic turbulence with heat transfer. The experiment is undertaken using Boger solution flows, which are viscoelastic solutions with polyacrylamide (but without elastic instability or elastic turbulence), and 65 percent sucrose, as well as with these solutions when elastic instabilities or elastic turbulence are present. Comparisons are also given relative to sucrose-solvent Newtonian fluid flows. Comparisons between the different types of fluids are generally undertaken at the same rotation speed, shear rate, flow passage height, and inlet temperature. Note that Boger fluids are generally characterized by constant viscosity that is independent of shear rate. Included are flow visualization results, variations of shear stress, strain rate, and viscosity, spatially-averaged heat transfer coefficients, spatially-averaged Nusselt numbers, and spectral analysis of the temperature fluctuations. Increased levels of local transport are illustrated by fluorescein dye concentration variations and by dye variations with time. Dye front variations are determined and related to effective diffusion coefficients, both with and without advection present. Overall aims include presentation of data which illustrate enhanced diffusion, thermal transport and convective heat transfer rates due to elastic instabilities and elastic turbulence. As such, the present investigation provides new insight into the mechanisms of elastic turbulence, and the conditions at which it occurs, as well as the effects on convective heat transfer, within environments which have never before been employed for this purpose

1.5 Organization of the Dissertation

This thesis is composed of nine chapters, four appendices, and a reference list. Chapter 2 describes experimental apparatus and procedures for the Viscous Disk Pump. Chapter 3 presents results for the Viscous Disk Pump. Chapter 4 describes experimental apparatus and procedures for Rotating Couette Flow. Chapter 5 presents results for the Rotating Couette Flow environment. Chapter 6 gives results for fluorescein dye advection within the Rotating Couette Flow environment. Chapter 7 presents results for Rotating Couette Flow with different gap heights. Chapter 8 presents polymer solutions rheological properties. Chapter 9 gives a summary and conclusions. Appendix A presents thermocouple response time data. Appendix B presents a rheological measurement approach to determine polymer relaxation time for high polymer concentrations. Appendix C presents a software directory. Appendix D presents a data file directory.

CHAPTER 2

EXPERIMENTAL APPARATUS AND PROCEDURES FOR VISCOUS DISK PUMP

The present chapter focuses on the experimental apparatus and procedures for Viscous Disk Pump (VDP). Details of the experimental apparatus and procedures are described, including all relevant measurement details. This chapter consists of ten parts: (1) viscous disk pump configuration and operation; (2) polymer solution preparation; (3) pressure drop measurements apparatus and procedures; (4) flow rate measurements apparatus and procedures; (5) flow visualization apparatus and procedures; (6) heat transfer and fluctuating temperature apparatus and procedures; (7) analytic determination of Nusselt numbers and heat transfer coefficients; (8) pressure transducer calibration procedure; (9) thermocouple calibration procedure; (10) experimental uncertainty magnitudes.

2.1 Viscous Disc Pump Configuration and Operation

The viscous disk pump or VDP experimental apparatus is composed of a spinning disk and a C-shaped channel with a fluid inlet port and a fluid outlet port, located at the two ends of the C-shaped channel. The diagram of the overall viscous disk pump is

shown in Figure 2.1. The overall arrangement, coordinate system for the flow passage, and dimensions are schematically shown in Figure 2.2. Within this figure, the shaded region of the pump chamber is used for the flow analysis. The z coordinate is directed normal to the surface, and measured from the stationary flat bottom surface of the flow passage. The flow passage height for the present investigation is 640 μm. Rotation speeds range from 10.47 to 209.4 radians/sec. As the disk rotates, its edges create a seal to minimize the leakage of working fluid by contacting the fluid chamber wall. Rotating Couette-type flow is thus induced in the fluid chamber between the rotating disk and the stationary bottom of the channel. The work done on the fluid by the rotating disk then leads to a circumferential pressure gradient within the C-shaped channel. This interaction gives a static pressure rise with circumferential position ΔP through the pump chamber volume, such that a region of lower static pressure is present near the fluid inlet port, and a region of higher static pressure is present near the fluid outlet port. This static pressure variation then opposes the motion induced by the disk rotation and viscous forces. If the opposing circumferential static pressure variation is large enough, some of the fluid between the spinning disk and the top surface of the fluid chamber recirculates in a direction which is opposite to the direction of the disk rotation. For the situation when the fluid outlet port is closed (or a valve on the outlet tubing is closed), the overall volumetric flow rate is zero. However, fluid movement continues to be present within the pump chamber in directions which are coincident with and also opposed to the direction of disk rotation. With this arrangement, the resulting static pressure rise is maximum for a particular disk rotational speed.

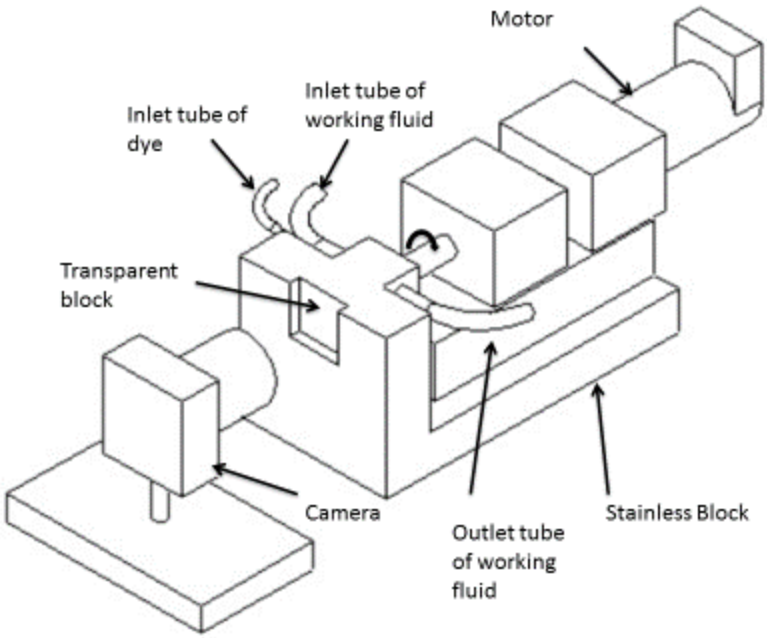

Figure 2.1 Diagram of overall viscous disk pump.

The disk pump is powered by an externally mounted Maxon EC32 #118890. The motor has a 48V winding, a power rating of 80W, a maximum speed of 25,000 rpm, and a stall torque of 0.353 Nm. The motor is controlled by a Maxon ESCON 50/5 #409510 motor controller connected to an Advanced Motion Controls model PS2X3W48 power supply. The power supply has a DC supply voltage of 48V, a peak current of 12 amperes, and a continuous current rating of 6 amps. The motor controller maintains a constant speed through a closed control loop and a Maxon HEDL 55 Encoder #110514. The speed and direction of the motor are controlled by regulating voltage to the analog and digital I/O channels on the motor controller using LABVIEW 32-bit software, version version 10.0.1, and a National Instruments USB-6003 data acquisition card. The rotational speed measurement system is calibrated using a timing light.

2.2 Polymer Solution Preparation

Four different solutions are utilized with four different polymer concentrations: 0 ppm, 80 ppm, 100 ppm, and 150 ppm, where ppm refers to polymer parts per million. As such, the 0 ppm arrangement is utilized with a 65 % sugar solution (without added polymers) to create a Newtonian solution with an approximately constant viscosity that is independent of shear rate. The viscoelastic solutions are then prepared by adding polyacrylamide powder into the sucrose solution. When each solution is prepared, the appropriate polymer concentration (as quantified using PAAm) is employed, along with 1 % NaCl, and 65 % sucrose. The procedure for mixing the stock solution is adopted from Abed et al. (2016). For example, to mix a 80 ppm solution, 0.048g of PAAm (Polyacrylamide, Mw = 18,000,000 Dalton, Polysciences Inc.) powder, 6 g of NaCl, and 390 g sucrose are dissolved in 204 g DI water, as the solution is gently combined for approximately 4 hours within a commercial mixer, with a propeller operating at moderate speed.

2.3 Pressure Drop Measurements Apparatus and Procedures

Static pressure rise is measured across the pressure ports. The overall set-up is shown in Figure 2.3. As shown in Figure 2.2, the holes for the pressure ports are 0.19 mm in diameter while holes for the fluid inlet and outlet ports are 1.40 mm in diameter. The pressure port holes are widened below the surface of the block to 1.59 mm.

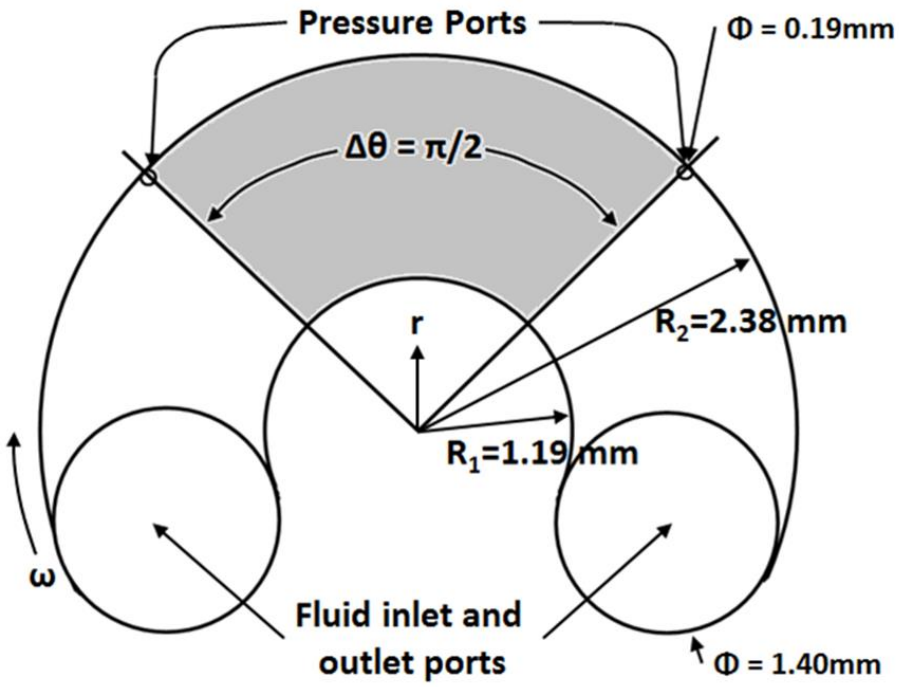

Figure 2.2 Configuration of the viscous disk pump, including coordinate system.

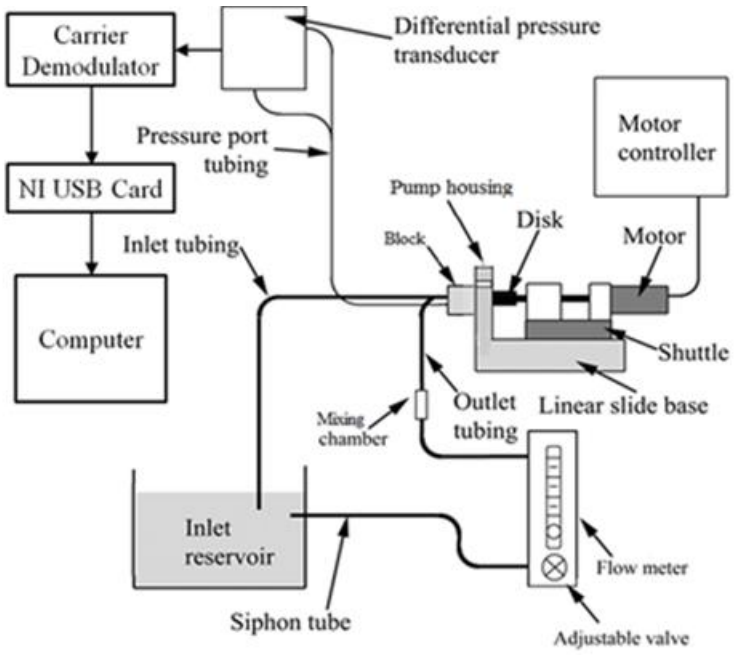

Figure 2.3 Arrangement and components for the viscous disk pump for pressure measurements.

A DP-15 Validyne differential pressure transducer is used to measure the differential pressure between the pressure ports. The transducer employs a number 20 diaphragm which can measure pressure differentials with ranges up to 872 Pa. The output signal from the pressure sensor is processed using a Celesco Model number CD15 Carrier Demodulator. This demodulator produces a voltage output that is read by a National Instruments USB-6210 data acquisition board and LABVIEW 32-bit software, version 10.0.1. All data are recorded, and then entered and processed using a Dell Precision T1700 computer workstation.

2.4 Flow Rate Measurement Apparatus and Procedures

A Key Instruments model 1XLW9 flow meter is used to measure the time-averaged fluid flow rate. This device is used for measurements of flow rate for water or for fluids with similar viscosity values, relative to water. To measure the mass flow rate of the polyacrylamide solutions, an Adam PGL 2002 scale is used. The fluid mass flow rate is determined by collecting the fluid exiting the pump on the scale and recording the change in mass of fluid over a specified time interval. To measure the time-averaged fluid flow rate, the combination of a valve, timer, and Adam PGL2002 measuring scale are thus employed.

2.5 Flow Visualization Apparatus and Procedures

The flow visualization device uses the same motor and motor controller as the flow measurement device, but does not have provision for pressure measurements. As such, the associated block does not contain pressure ports and is made from optically clear acrylic instead of stainless steel. The corresponding photograph and diagram of overall instrumentation are shown in Figure 2.4 and 2.5.

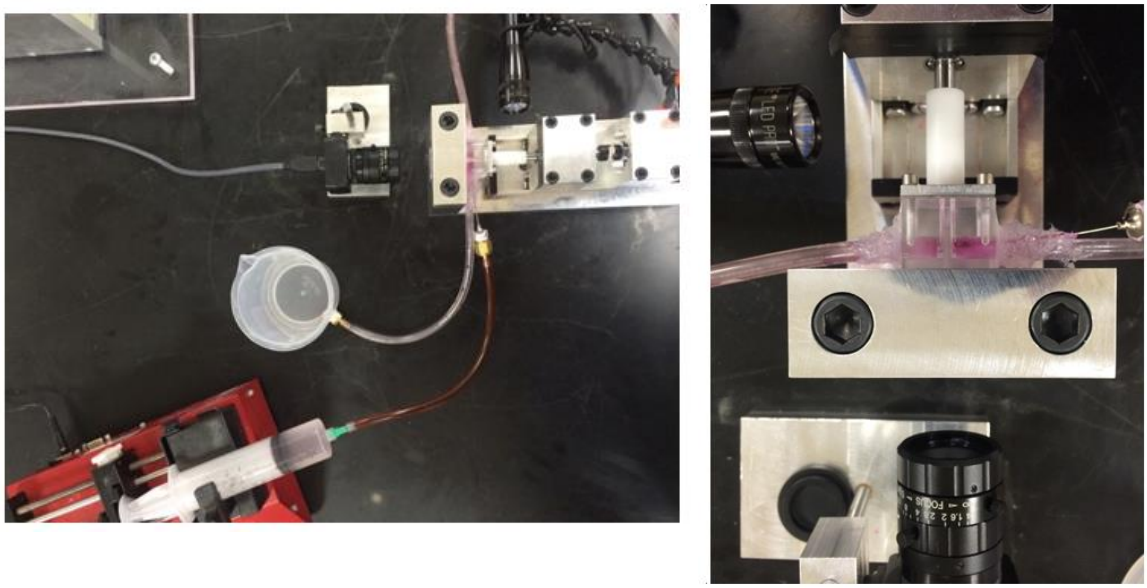

(a) (b)

Figure 2.4. Photograph of overall viscous disk pump apparatus.

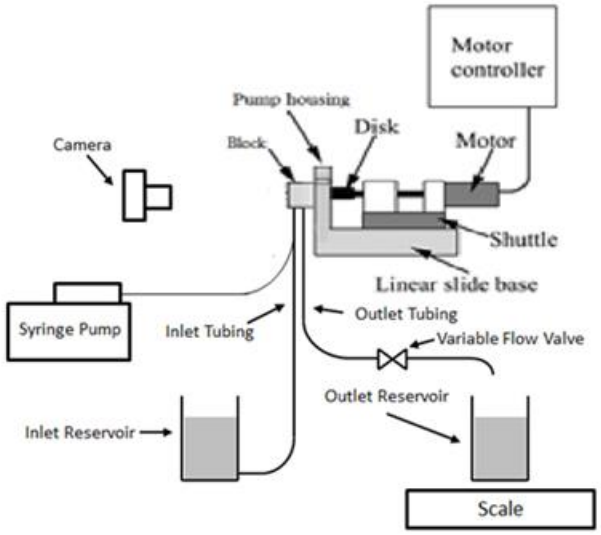

Figure 2.5 Diagram of overall instrumentation for flow visualization.

As shown in Figure 2.1, the pump assembly is mounted to the base of a linear slide. The brushless motor and disk shaft are also mounted to the shuttle of the linear

slide. The disk shaft is supported with two bearings, and the distal end of the disk shaft connects to the motor shaft. Elastic bands are employed to exert a constant force on the shuttle in the direction of the pump chamber to keep the disk surface flush against the bottom of the pump housing. An alignment fixture is used to mount the pump housing and pump chamber, such that the axis of the disk aligns with the center point of the pump chamber radius. The pump assembly is placed on a level surface to ensure that there are no height differences between the flow inlet and outlet ports or between the two pressure ports. After assembling the disk, disk shaft, and pump chamber, the fluid inlet and outlet tubing are press-fit into the top of the pump housing. Before the test start, the tubing, and pump housing are filled with the working fluid. Syringes are subsequently used to remove any air from the liquid which is contained within the system.

As shown in the photograph of the overall set-up are shown in Figure 2.4, the pump housing block is made from optically clear acrylic. Note that the flow passages turn ninety degrees toward the sides of the block, at a location which is approximately 12 to 14 mm beneath the surface of the channel, so that visualization views are not obstructed. The acrylic is polished using NOVUS plastic polish to remove any tooling marks and blemishes. An LED (light emitting diode) flashlight on a gooseneck clamp is directed at the Delrin disk to provide backlighting in the channel. A Point Gray CMLN-13S2C-CS USB camera, with a 25 mm lens, records images of the channel at a rate of 15 frames per second. The images are saved as 8-bit indexed .bmp image files. To provide contrast in the channel, Kingscote fluorescent FWT red tracer dye is injected into the channel with a New Era Pump Systems NE-1000 syringe pump at rates ranging from 0.001 to 0.065 milliliters per minute. Pure dye with 100 percent concentration is employed for this

purpose. The syringe is 28.58 mm in diameter and is connected through tubing to a needle positioned in the inlet flow passage. Throughout testing, the inlet reservoir is maintained at a constant level, which is aligned with the outlet tubing, to minimize variations due to hydrostatic pressure and gravity.

2.6 Heat Transfer and Fluctuating Temperature Apparatus and Procedures

Within the present study, the VDP is employed for measurement of spatially-averaged heat transfer coefficients and Nusselt numbers over the entire flow passage surface area, as well as measurement of the fluctuating temperature within the exit part of the flow passage. To accomplish this task, fluid temperature is measured at the inlet and outlet of the flow passage using Omega 5TC-TT-T-40-72 fine-wire copper-constantan (Type T) thermocouples. Inlet temperature is measured using one thermocouple located at the central part of the beaker which supplies the working fluid. This temperature is representative of the mixed mean temperature at the inlet of the VDP flow passage, because of the absence of any temperature gradients within the apparatus up to and upstream of that location. In general, the inlet temperature is constant at approximately 22 ºC, which is the same as room temperature. The temperature of the fluid at the outlet of the VDP is measured using the apparatus which is shown in Figure 2.6. The associated thermocouple at the outlet is fixed with glue and dried for 24 hours to insure that it is immobile as testing is underway. Because of the mixing which takes place within the flow, and the transient means whereby the fluid is displaced from the inlet to the outlet of the VDP flow passage, this measured temperature is representative of the fluid mixed mean temperature at the exit of the VDP flow passage.

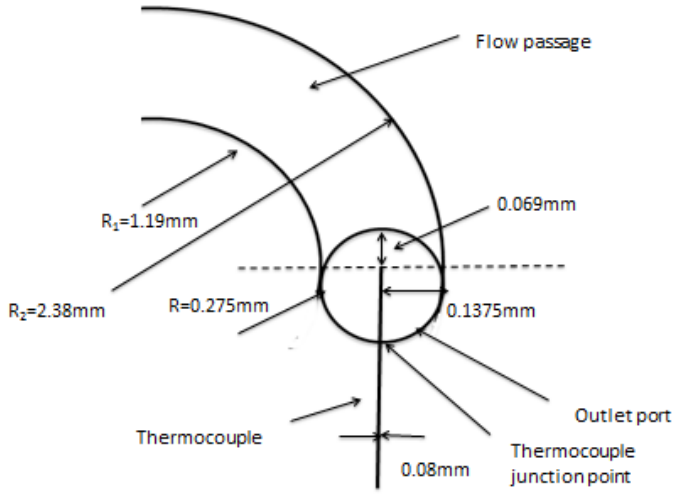

(a)

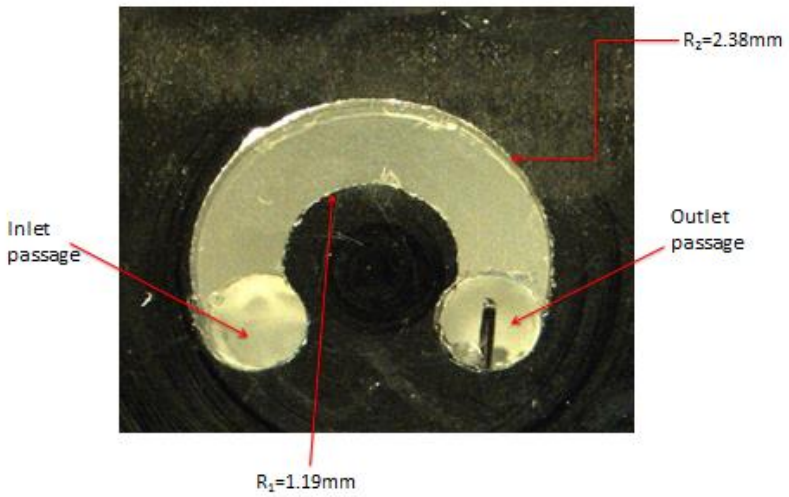

(b)

Figure 2.6. (a) Dimensions and (b) photograph of the thermocouple located at the flow passage outlet.

In order to determine time-averaged magnitudes of the mean-squared temperature fluctuation, instantaneous flow temperature variations are recorded using the inlet and

outlet thermocouples over a period of 90 s at a frequency of 100 Hz, after flow within the VDP reaches a steady-state operating condition. The mean square of fluctuating temperature, relative to the time-averaged temperature, is then determined using EXCEL software. To determine power spectra of fluctuating temperature, the MATLAB software code is employed. This code utilizes a Fast Fourier Transform (FFT) applied to instantaneous time-varying temperature data. To reduce levels of background, "white" noise, a Savitzky-Golay filter is applied. The frequency response of the thermocouple junction for these measurements is estimated to be approximately 0.12 to 0.16 milliseconds.

As temperature data are acquired, thermocouple voltages are read sequentially using a National Instruments NI 9213 thermocouple input card mounted within a National Instruments NI cDAQ-9188 chassis, connected to the computer workstation. These terminals relay the information to a Dell Precision T1700 computer. The voltage outputs from this unit are acquired by the computer through its USB port, using LABVIEW software, version 10.0.1. With the procedures employed, the thermocouples have a measurement accuracy of 0.05ºC to 0.10ºC, and are calibrated in the range 20ºC to 44ºC using an HCTB-3020 Omega Thermo-Regulator.

2.7 Analytic Determination of Nusselt Numbers and Heat Transfer Coefficients

Heat transfer measurements are based upon energy balance considerations, which utilize the mixed-mean temperature at the inlet and outlet of the viscous disk pump flow passage. The overall heat transfer rate is determined based upon a constant surface temperature thermal boundary condition, and upon a log-mean-temperature difference approach. The thermal boundary condition at the bottom surface and side walls of the

VDP passage is constant temperature, whereas the rotating disk is adiabatic. This constant surface temperature boundary condition is achieved within the VDP for the bottom flow passage surface and the side walls because they are made of stainless aluminum with relatively high magnitude of thermal conductivity (k_{Al}=205 W/(m·K)). The rotating disk is machined from PEEK plastic with a thermal conductivity of 0.252 W/(m·K), to minimize heat loss from the flow passage, and to minimize shape variations which may occur as heat transfer tests are underway.

With these considerations in mind, the bottom and side walls of VDP flow passage are maintained at constant temperature, T_s, and the rotating disk which is adjacent to the working fluid is adiabatic, such that q_{disk}=0. The log-mean-temperature difference equation is then applied between the outlet and the inlet of the VDP flow passage, as follows

$$\ln\left(\frac{T_{out}-T_s}{T_{in}-T_s}\right) = -\frac{DL}{\rho c V A}h \tag{2.1}$$

Note that both temperature and velocity fields are expected to be fully-developed at a very short streamwise distance downstream of the fluid inlet port. Within Eqn. (2.1), L is the characteristic length which is given by

$$L = \frac{\pi(R_2+R_1)}{2} \tag{2.2}$$

P is then the channel perimeter, and D is the portion of the perimeter where the constant temperature boundary condition is applied. These quantities are determined from the equations given by

$$P = 2(R_2-R_1)+2s \qquad D = (R_2-R_1)+2s \tag{2.3}$$

The total heat flux into the VDP flow passage is then expressed using

$$\dot{q} = (T_{out} - T_{in})\rho cVA \tag{2.4}$$

where T_{in} and T_{out} are inlet and outlet flow passage mixed mean temperatures, respectively. Rearranging Eqn. (2.4) then gives

$$\rho cVA = \frac{\dot{q}}{T_{out} - T_{in}} \tag{2.5}$$

After further rearrangement, the overall VDP passage heat transfer coefficient is then determined using

$$h = \frac{\dot{q}}{LD\,\frac{T_{out} - T_{in}}{\ln(\frac{T_{out} - T_s}{T_{in} - T_s})}} \tag{2.6}$$

The overall Nussult number is then given by

$$Nu = \frac{hs}{k} \tag{2.7}$$

where *h* is the overall flow passage heat transfer coefficient.

2.8 Pressure Transducer Calibration Procedure

The DP-15 Validyne differential pressure transducer is calibrated from 0 Pa to 875 Pa using a Validyne model T140K calibrator kit that includes a pressure pump. The pressure calibrator is connected to the pressure pump and the pressure transducer is connected to a Celesco Model number CD15 Carrier Demodulator, which provides a DC signal that will be proportional to the pressure at the transducer after calibration. Note that the transducer and demodulator are calibrated connected together as a system. This demodulator produces a voltage output that is read by a National Instruments USB-6210 data acquisition board and LABVIEW 32-bit software, version 10.0.1. All the recorded data are entered and processed using a Dell Precision T1700 computer workstation.

The calibration of pressure transducer includes two parameters: Zero and Span (875 pa) pressure. Firstly, zero pressure is applied to the transducer, turn the Zero adjustment until the reading on LABVIEW is 0 V_{DC}. 875 Pa (span) pressure is then applied to the transducer and turn the Span adjustment until reading is +10 V_{DC}. The above procedure is repeated to make sure each reading is correct. After the calibration, the tolerance of the reading is approximately ± 0.005 V_{DC}.

2.9 Thermocouple Calibration Procedure

Thermocouples are calibrated in the range 20^{o}C to 44^{o}C using an HCTB-3020 Omega Thermo-Regulator, which is a constant temperature water bath. The end of each thermal couple is fixed in the water bath and a Fluke Hart 1523 Thermometer and stainless steel sheathed thermistor (which is accurate within ±0.01 ^{o}C) are employed to measure bath temperature. The other end of the thermocouple is connected to a National Instruments 9213 thermocouple card, which is connected to a NI USB-9162 high speed USB carrier data acquisition card. Both of these devices are mounted within a National Instruments NI cDAQ-9188 chassis. Information from these terminals is acquired using a Dell Precision T1700 computer through its USB port, using LABVIEW 32-bit software, version 10.0.1. The temperature of the water bath is then adjusted to 20^{o}C to 44^{o}C in temperature steps of 2 ^{o}C. The temperature of the water bath and the voltage are recorded for each test point. The results are recorded by the LABVIEW software, version 10.0.1.

2.10 Experimental Uncertainty Magnitudes

Experimental uncertainty magnitudes associated with measured quantities are provided in Table 2.1. Uncertainty magnitudes for different heat transfer related quantities are then provided in Table 2.2. Within this latter table, values are given for the

sucrose-based Newtonian fluid, as well as for solutions with three different polymer concentrations.

Table 2.1. Experimental uncertainties associated with experimental data.

Variable	Maximum percent uncertainty
ΔP	5.00
$\dot{\mathbf{v}}$	2.50
s	2.75
Ω	1.50
R_1,R_2	1.10

Table 2.2. Uncertainty values of experimental parameters associated with heat transfer measurements, as they vary with polymer concentration.

Concentration (ppm)	Temperature	Mean square of fluctuating temperature	Nusselt number
0 (Sucrose Solution)	8.34%	11.79%	9.18%
80	6.53%	9.24%	7.78%
100	5.27%	7.43%	6.28%
150	4.91%	6.09%	5.04%

CHAPTER 3

EXPERIMENTAL RESULTS: VISCOUS DISK PUMP

Presented are results which illustrate transition from laminar Boger solution flow to elastic instability flow to elastic turbulence flow, along with the associated variations of surface convective heat transfer. Included are flow visualization results, heat transfer coefficient values, Nusselt numbers, and time-averaged magnitudes of the mean square of instantaneous temperature fluctuation. Viscous disk pump rotation speeds of 500 rpm, 1000 rpm, 1500 rpm and 2000 rpm are utilized. For most conditions of the present study (with the exception of viscosity), property values for 80 ppm, 100 ppm, 150 ppm and 300 ppm polyacrylamide solutions with 65% sucrose, are within a few percent of values for the 65% sucrose solution by itself.

3.1 Experimental Conditions

Table 3.1 provides information on experimental conditions and parameters which are employed within the viscous disk pump. Included are values of fluid molecular thermal conductivity, specific heat, and static density. Fluid flow mass flow rate, absolute viscosity, kinematic viscosity, molecular Prandtl number, Reynolds number, and flow passage average velocity are then provided for different disk rotational speeds, and different polymer concentrations. Note that some of the property values presented within

Table 3.1 are from Abed et al. (2016). Table 3.2 then provides data obtained using the Anton Paar Rheometer MCR 302, including magnitudes of absolute fluid viscosity, as it varies with shear rate, and shear stress. Associated values of shear rate and rotational speed, which are associated with the viscous disk pump, are then included in this latter table for comparison. From Table 3.1, Reynolds numbers, based upon flow passage gap height and spatially-averaged velocity, range from 0.033 to 0.240, and Reynolds numbers, based upon flow passage gap height and rotation speed at the flow passage centerline, range from 0.110 to 0.874.

Table 3.1 Experimental conditions and parameters within the viscous disk pump.

ρ (kg/m^3)	k (W/m·K)	c (J/kg·K)
1315	0.368	2600

ρ_c (ppm)	$\dot{m}$ (kg/s)	V (m/s)	μ (Pa·s)	ν (m2/s)	Re_ω	Re	Pr
52.3 rad/s							
0	0.000035	0.035	0.179	0.000136	0.220	0.165	1265
80	0.000033	0.033	0.194	0.000148	0.206	0.143	1371
100	0.000023	0.023	0.235	0.000179	0.167	0.083	1662
150	0.000020	0.020	0.347	0.000264	0.113	0.048	2450
104.7 rad/s							
0	0.000041	0.040	0.179	0.000136	0.439	0.188	1265
80	0.000040	0.040	0.192	0.000146	0.410	0.175	1357
100	0.000039	0.039	0.233	0.000177	0.337	0.141	1647
150	0.000020	0.020	0.346	0.000263	0.227	0.049	2446
157.1 rad/s							
0	0.000051	0.051	0.179	0.000136	0.659	0.240	1265
80	0.000045	0.045	0.191	0.000145	0.618	0.197	1350
100	0.000021	0.021	0.232	0.000276	0.508	0.076	1640
150	0.000017	0.017	0.345	0.000262	0.342	0.041	2438
209.4 rad/s							
0	0.000047	0.047	0.180	0.000137	0.874	0.220	1272
80	0.000028	0.028	0.190	0.000144	0.828	0.124	1342
100	0.000025	0.025	0.232	0.000176	0.678	0.091	1639
150	0.000026	0.021	0.345	0.000262	0.456	0.063	2438

Table 3.2 Fluid properties for the 80 ppm polymer solution (with 65 percent surcrose), as determined using the Anton Paar rheometer.

Rheometer data			VDP data		
$\dot{\gamma}$ (1/s)	μ (Pa·s)	τ (Pa)	$\dot{\gamma}$ (1/s)	ω (rad/s)	Re_ω
0	0.253	0	0	0	0
30	0.219	6.57	30	10.76	0.03
51	0.197	10.0	51	18.32	0.07
102	0.195	19.9	102	36.57	0.14
153	0.194	29.7	153	54.86	0.22
204	0.193	39.4	204	73.14	0.28
255	0.193	49.2	255	91.43	0.36
306	0.192	58.8	306	109.71	0.43
357	0.192	68.5	357	128.00	0.50
408	0.192	78.3	408	146.29	0.57
459	0.191	87.7	459	164.57	0.65
510	0.191	97.4	510	182.86	0.72

3.2 Visualizations of Flow Characteristics

Flow visualization images for sucrose and 100 ppm polymer solution are presented in Figure 3.1, with a flow passage height of 640 μm. Visualization images in Figure 3.1a are shown for a range of rotation speeds for the sucrose Newtonian solution from 100 RPM or 10.47 radians/sec. to 1000 RPM or 104.7 radians/sec., and shear rates from 29.21 1/s to 292.1 1/s. Visualization images in Figure 3.1b are shown for 100 ppm viscoelastic polyacrylamide solution at the same rotation speeds and shear rates. As the dye is injected near the middle of the inlet flow passage, dye trajectories and distributions illustrate the mixing and agitation from the elastic turbulence. The pathlines as presented in Figure 3.1a are smooth, narrow and well defined with little distortion as the rotation speed increases, following the trajectory of laminar flow streamlines. The pure laminar distribution of the dye indicates that only minimal secondary flow and no augmented mixing occurs within the channel.

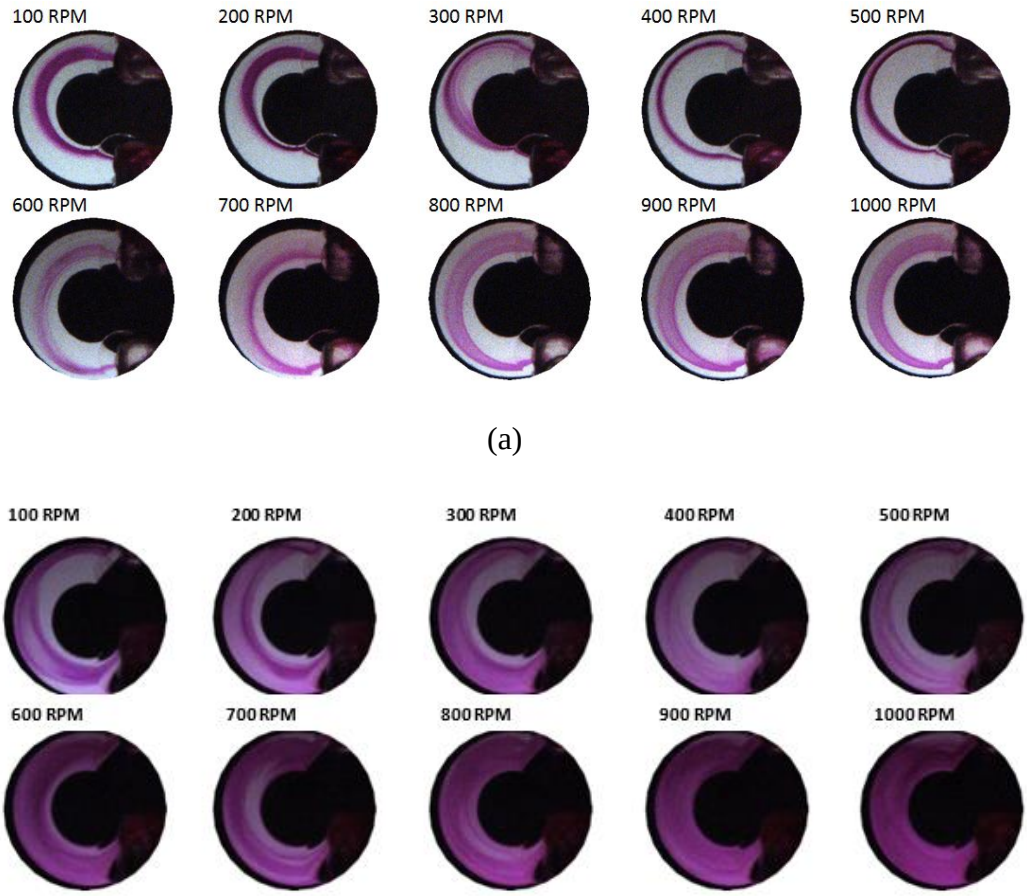

Figure 3.1 Flow visualization images. Sucrose solutions with (a) 0 ppm polyacrylamide concentration, and (b) 100 ppm polyacrylamide concentration.

When the 100 ppm polymer solution is employed, flow behavior, which is illustrated by the results in Figure 3.1b, is dramatically different compared to the sucrose solution results. Images within Figure 3.1b show that mixing is significantly enhanced, since dye begins to spread immediately at or near the inlet of the flow passage. In some cases, this spreading may occur initially within the flow passage near the VDP inlet. Afterwards, dye is spread throughout the entire flow passage, and over the entire radial extent of the passage. These events are believed to result in initial polymer agitation, as

well as increased stretching in the circumferential direction. The dramatic dye spreading is associated with the onset and development of elastic instabilities.

The differences in flow visualization images between Figures 3.1a and 3.1b are not due to increased viscosity values alone, because the natural tendency of increased viscosity (with or without polymers present) is suppression of flow fluctuations. In addition, centrifugal instabilities associated with streamline curvature are not responsible for the observed variations, because associated Dean numbers are not large enough to allow development of the associated centrifugal-instability induced secondary flows. The experimental conditions associated with transition also cannot be characterized by one Dean number, and associated Dean numbers do not vary with polymer concentration. Within the present investigation, Reynolds numbers, based upon flow passage gap height and spatially-averaged velocity, range from 0.033 to 0.240. Reynolds numbers, based upon flow passage gap height and rotation speed at the flow passage centerline, range from 0.110 to 0.874. Because the radius of the convex surface is the same as the radial extent of the flow channel, associated Dean numbers cover the same range of values.

Elastic instabilities are also not induced by streamline curvature and the associated flow strain which is imposed on the flow as streamlines turn from the fluid inlet port into the C-shaped channel. Local secondary flows, small-scale vortical regions, and regions of augmented shear adjacent to small-scale flow separation zones, also probably contribute to locally augmented magnitudes of flow strain. Here, the formation of centrifugally-induced Dean vortex pairs is unlikely because streamwise curvature from the turn is not imposed over sufficient streamwise distance to induce the development of centrifugal instabilities (Ligrani et al., 1988; 1996; 2004). However, even if such Dean

vortex pairs were present (which they are not), they do not have sufficient magnitudes of local vortex circulation to produce the augmentations of local flow mixing and spatially-averaged Nusselt numbers which are observed within the VDP (and discussed later) (Ligrani et al., 1988; 1996; 2004). As such, the only phenomena present which can induce the observed variations are elastic instabilities and elastic turbulence.

Diffusion velocities provide information in regard to the transport of dye distributions associated with experimental data, such as are shown in Figures. 3.1a and 3.1b. Such velocities are presented in Figure 3.2, as they vary with polymer concentration and viscous disk pump rotational speed. Here, dimensional diffusion velocities are given by the ratio of kinematic viscosity to flow passage gap height, or ν/s. As such, this parameter represents variations of transport *only from molecular effects*. Figure 3.2 shows that diffusion velocity values increase with polymer concentration for each value of disk rotational speed, and increase with rotational speed for each value of polymer concentration. For each value of disk rotational speed, minimum diffusion velocity is then always associated with the 0 ppm polymer concentration, for the associated Newtonian, sucrose solution fluid.

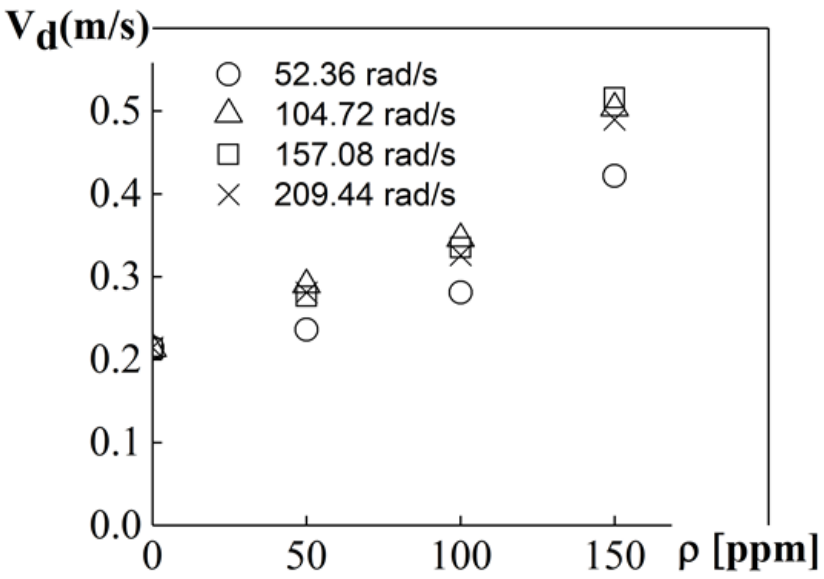

Figure 3.2 Diffusion velocity as it varies with polymer concentration and viscous disk pump rotational speed.

The observed increases of molecular transport diffusion velocity with polymer concentration and with disk rotational speed can help increase overall transport levels, but only by relatively small amounts. To counter such transport level increases, higher dimensional molecular-based diffusion velocities probably contribute to the suppression of the onset and development of elastic turbulence. This is because associated increases in absolute viscosity and kinematic viscosity generally suppress unsteady flow fluctuations and chaotic fluid motions, relative to Newtonian fluids, and Boger fluids, where viscosity values are lower.

3.3 Flow Conditions For Transition to Elastic Turbulence

The experimental conditions for transition to elastic instability for different polymer concentrations and different shear rates at 20^{o}C are given in Figure 3.3. These transition data are determined from visualization images at a gap height of 640 μm, when

the disk rotational speed Ω is between 100 RPM (or 10.47 radians/s) and 2000 RPM (or 209.4 radians/s). Associated shear rates are 29.21 1/s and 584.2 1/s, respectively. The transition onset is evidenced as dye becomes more spread out and more diffuse throughout the viscous disk pump flow passage, as shown in Figure 3.1. Figure 3.3 shows that this transition onset occurs at lower shear rates as the concentration of polyacrylamide increases. This is speculated to be due to increased interactions between the polymer chains within the flow, as polymers per unit volume become more numerous.

Note that the changes illustrated by the data in Figure 3.3 cannot be attributed to secondary flows from centrifugal instabilities. This is because the experimental conditions associated with transition cannot be characterized by one Dean number, and because associated centrifugal instabilities (and associated Dean numbers) do not vary with polymer concentration. In addition, sufficient streamwise development length is not provided to induce the development of Dean vortex pairs, for the curved streamlines which are present as flow advects from the inlet port to the C-shaped channel, as mentioned earlier.

To characterize the onset of elastic instabilities, McKinley et al. (1996) propose the relationship which is given by

$$[\frac{\lambda U}{R}\frac{\tau_{11}}{(\mu_0\dot{\gamma})}]^{1/2} \geq M_{crit}$$

The τ_{11} tensile stress is estimated using the Oldroyd-B model (McKinley et al., 1996), which is of the form

$$\tau_{11} = 2\,\mu_p\,\lambda\,\dot{\gamma}^2$$

Here, $\mu_0 = \mu_p + \mu_s$ and $\beta = \mu_s/\mu_o$, so that $1 - \beta = \mu_p/\mu_o$. When these parameters are substituted into the original relationship, the expression becomes

$$[\frac{2U\lambda^2\dot{\gamma}(1-\beta)}{R}]^{1/2} \geq M_{crit}$$

For the VDP, the characteristic velocity and shear rate are then given by

$$U = \omega R/2$$

$$\dot{\gamma} = \frac{\omega R}{s}$$

With these substitutions employed, the expression to characterize the onset of elastic instabilities within the VDP is then given by an equation of the form

$$\left[\frac{\omega^2 R\lambda^2(1-\beta)}{s}\right]^{\frac{1}{2}} \geq M_{crit} \tag{3.1}$$

Equation (3.1) can also be expressed in terms of the Weissenberg number, Wi, given by $\dot{\gamma}\lambda$, and the Deborah number, Deb, given by $\omega\lambda$

$$[Wi.Deb.(1-\beta)]^{1/2} \geq M_{crit} \tag{3.2}$$

According to the results in Figure 3.3, the onset of elastic instabilities depends upon polymer concentration. This dependence is included within Eqn. (3.1) by means of the (1-β) term, as well as by λ the relaxation time term. Using magnitudes of relaxation time from Abed et al. (2016), Eqn. (3.1) is compared to the present transition data within Figure 3.3. This is accomplished by first determining the M_{crit} value of 87.7 for a polymer concentration of 100 ppm. With this approach, Figure 3.3 shows that Eqn. (3.1) provides

a reasonable match to the present elastic instability transition onset conditions, especially for the higher concentrations of polyacrylamide which are considered.

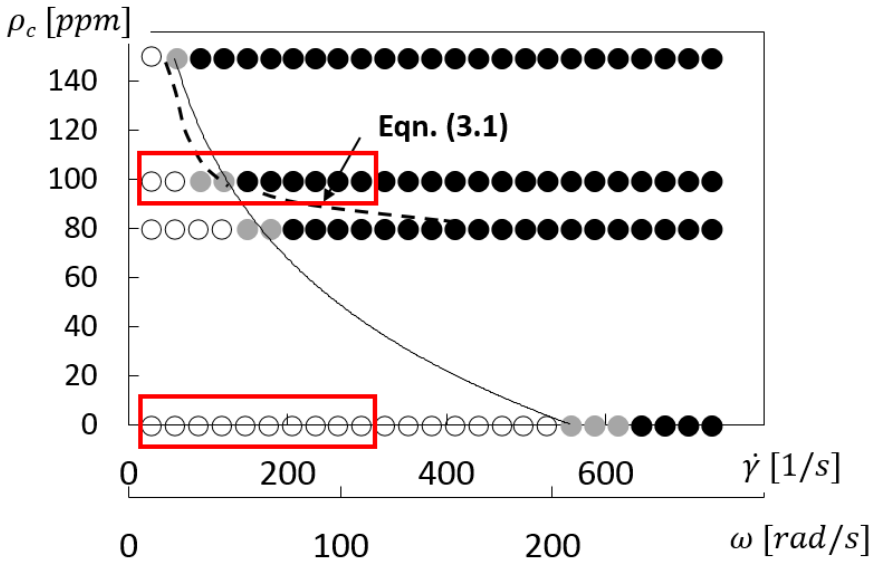

Figure 3.3. Elastic instability transition onset within the viscous disk pump from flow visualization images. Red rectangles show data range for Figure 3.1. Associated range of $\dot{\gamma}$ is 29.21 1/s to 292.1 1/s.

According to Burghelea et al. (2007), the microscopic phenomenon responsible for macroscopic elastic turbulence flow is called “coil-stretch transition”. This occurs when the polymer molecules are strongly stretched to sizes which approximate the total polymer length. This occurs when the stretch rate exceeds the inverse polymer relation time. This stretch rate condition is then also the basis of the definition of the Weissenberg number. When greater than some threshold value, higher Wi values, and sufficiently high stretch rates, then evidence the onset and presence of elastic turbulence. Timewise variations of a fluid with long polymer molecules are thus important because the polymers allow the fluid to store stresses. This storage capability gives the fluid a memory, which makes them non-Newtonian. Within curvilinear shear flows, the overall

result is complicated and irregular local fluid motions. Additional consequences include polymer feedback to and from the surrounding flow. This leads to non-uniform distributions of elastic stresses, and additional polymer stretching, as well as enhanced development of strongly non-linear, non-Newtonian flow behavior (Burghelea et al., 2007).

Note that, when the stretching rate of the flow is smaller than the inverse polymer relaxation time, deformation of the polymers is moderate. With this situation, the polymer solution flows are closer to Newtonian, with no memory. As a result, the influence of polymers on the flow is negligible.

3.4 Variations of Overall Pressure Rise and Shear Stress

Variations of dimensional pressure rise with dimensional volumetric flow rate (and dimensional mass flow rate) are illustrated by the data given in Figure 3.4 for a rotation speed of 2000 RPM (or 209.4 radians/s), and a shear rate of 584.2 1/s. Here, dimensional pressure rise generally decreases with dimensional mass (or volume) flow rate in an approximately linear fashion, for the sucrose solution, as well as for the 100 ppm polymer solution. As a result, the maximum dimensional pressure rise is obtained for zero volumetric flow rate (for each polymer concentration). When compared at the same mass flow rate, volumetric flow rate, shear rate, and disk rotational speed, Figure 3.4 shows that dimensional pressure drop is significantly larger for the 100 ppm polymer solution flows, with larger slope variation as mass flow rate varies, relative to the Newtonian sucrose solutions. Here, the decrease of static pressure rise with increasing flow rate indicates that the present VDP behaves similarly to a radial flow pump with backward curved impeller blades.

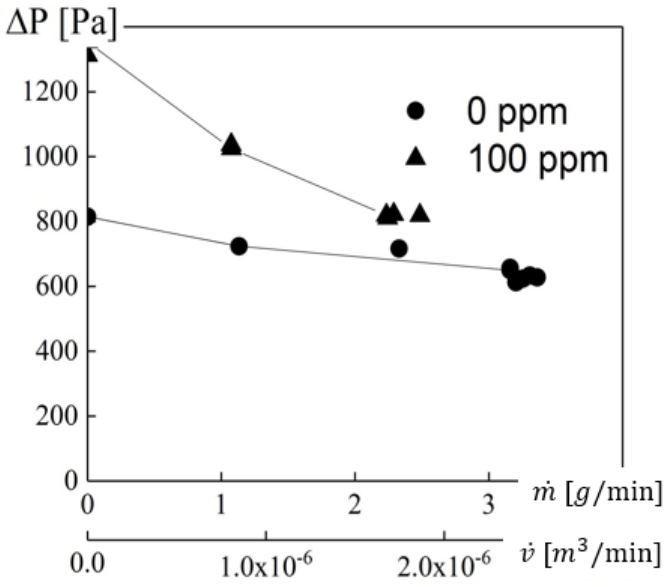

Figure 3.4. Dimensional pressure rise variations with dimensional mass and volumetric flow rates.

The relationship between dimensional pressure rise and overall dimensional shear stress within the viscous disk pump is given for the sucrose solution, as well as for the 100 ppm polymer solution, in Figure 3.5. These data are also provided for a rotation speed of 2000 RPM (or 209.4 radians/s), a shear rate of 584.2 1/s, and a flow passage height of 640 μm. All data show that pressure rise increases as dimensional shear stress increases, regardless of the type of fluid. In general, higher magnitudes of overall shear stress and pressure rise are present for the combination polymer/sucrose solutions, relative to the sucrose only solutions, with data for both solutions approximately following similar trend.

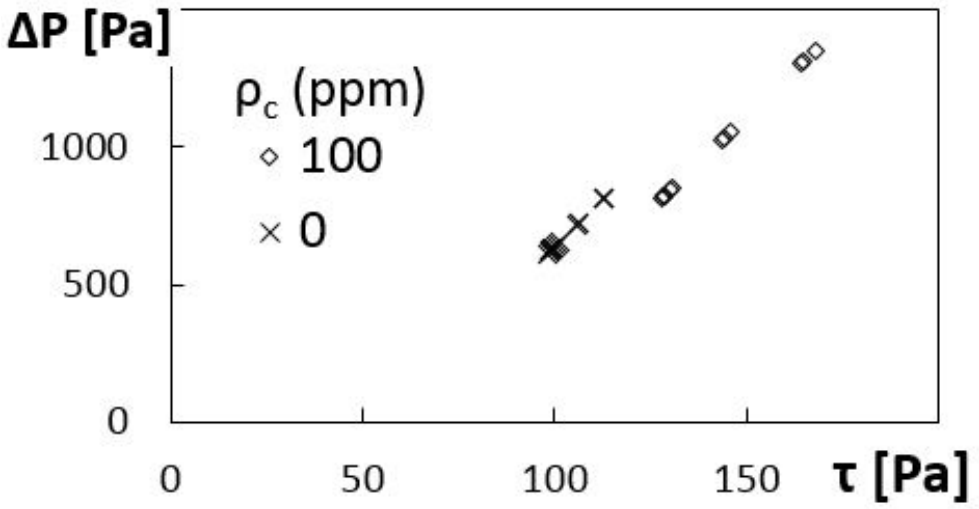

Figure 3.5. Dimensional pressure rise variations with dimensional overall shear stress.

Larger elastic turbulence effects are generally associated with larger magnitudes of local and spatially-averaged shear stress. Figures 3.4 and 3.5 indicate the most important polymer agitations associated with elastic turbulence generally occur as the dimensional volumetric flow rate becomes smaller. As such, the present data show that polymer solutions can cause sharp growth in flow resistance, as elastic instability or elastic turbulence develop.

As a result, secondary flow develop in the viscoelastic flow due to the normal stresses, which are tied to streamline curvature within the C-shaped channel, leading to the onset and development of elastic turbulence (Whalley et al., 2015). According to Burghelea et al. (2007), the mixing and secondary flows associated with elastic turbulence are driven by the "coupling" between the primary circumferential shear flow and the secondary radial polymer elongation flow. This "coupling" between radial and shear flows within the VDP is believed to lead to increased polymer stretching in the

circumferential direction, increased polymer agitation, higher shear stresses, and larger static pressure rises.

Associated values of overall shear stress, are given in Figure 3.6 as they vary with dimensional mass and volumetric flow rates. These data are provided for the same experimental conditions as the data in Figures 3.4 and 3.5. Here, for each polymer concentration (0 ppm and 100 ppm), overall shear stress declines (approximately) linearly with dimensional volumetric (and mass) flow rate. Here, shear stress values include contributions from both Couette flow and Poiseuille flow, which depend separately, and respectively, upon shear rate and pressure rise. Overall, the results in Figures 3.4, 3.5, and 3.6 show that the largest polymer agitations associated with the polymer solution flows occur at higher pressure rises, higher shear stress values, and lower volumetric flow rates within the viscous disk pump.

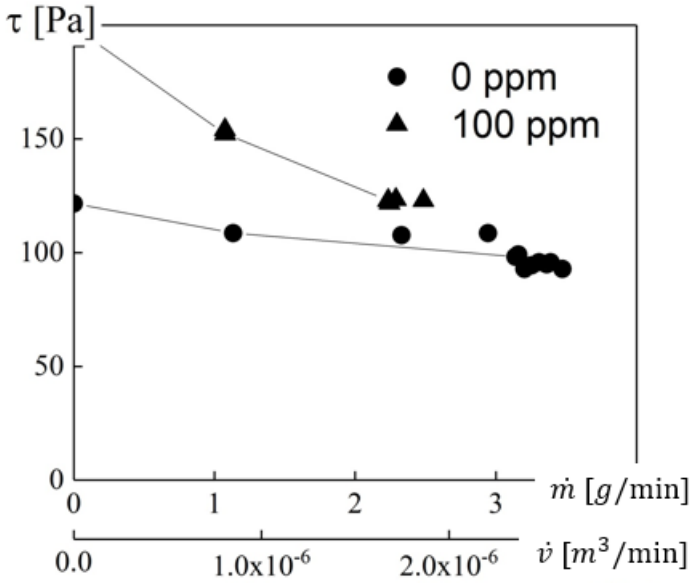

Figure 3.6 Dimensional overall shear stress variations with dimensional mass and volumetric flow rates.

3.5. Convective Heat Transfer Characteristics

Variations of convective heat transfer characteristics for the polyacrylamide/sucrose solutions and the Newtonian sucrose solutions are determined from measurements and analysis, and are given in Figures 3.7 and 3.8. Results are given for disk rotational speeds of 500 RPM, 1000 RPM, 1500 RPM, and 2000 RPM, or 52.3 radians/s, 104.7 radians/s, 157.1 radians/s, and 209.4 radians/s, respectively, with respective overall shear rates of 146.0 1/s, 292.1 1/s, 438.1 1/s and 584.2 1/s

Figure 3.7 shows that spatially-averaged Nusselt numbers increase with increasing polymer concentration for each of the four shear rates considered (and for each of the four disk rotational speeds). Figure 3.8 then shows that spatially-averaged Nusselt numbers increase with disk rotational speed for each polymer concentration employed. When compared for a particular shear rate or disk rotation speed, the minimum Nusselt number is always associated with the 0 ppm sucrose solution, which is the Newtonian sucrose fluid. Spatially-averaged Nusselt numbers thus show significant variations as polyacrylamide concentration is changed, which are tied to different extents of elastic instability development. Associated variations within the viscous disk pump flow passage are thus associated with increased polymer interactions and agitation, and enhanced local mixing, which results in overall increases in local and global thermal transport.

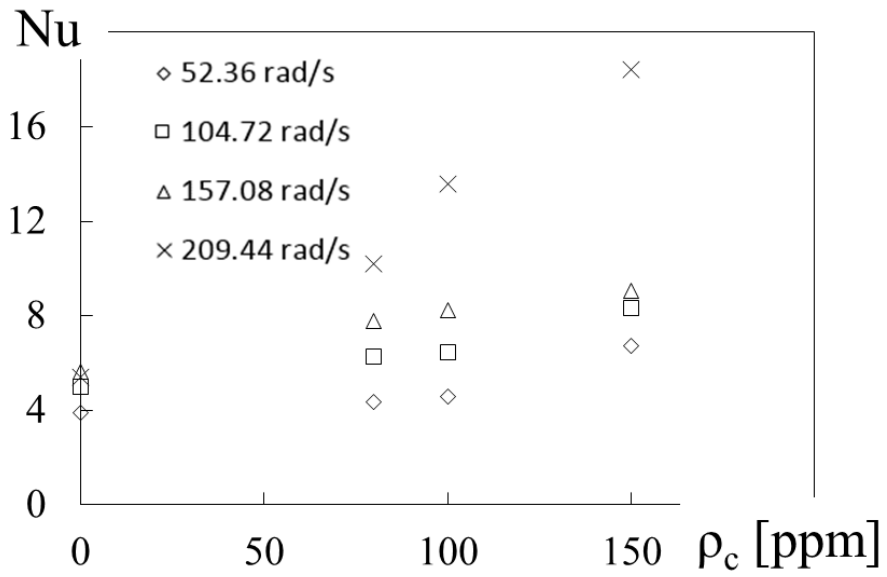

Figure 3.7. Overall Nusselt number variations with polymer concentration for different viscous disk pump rotational speeds.

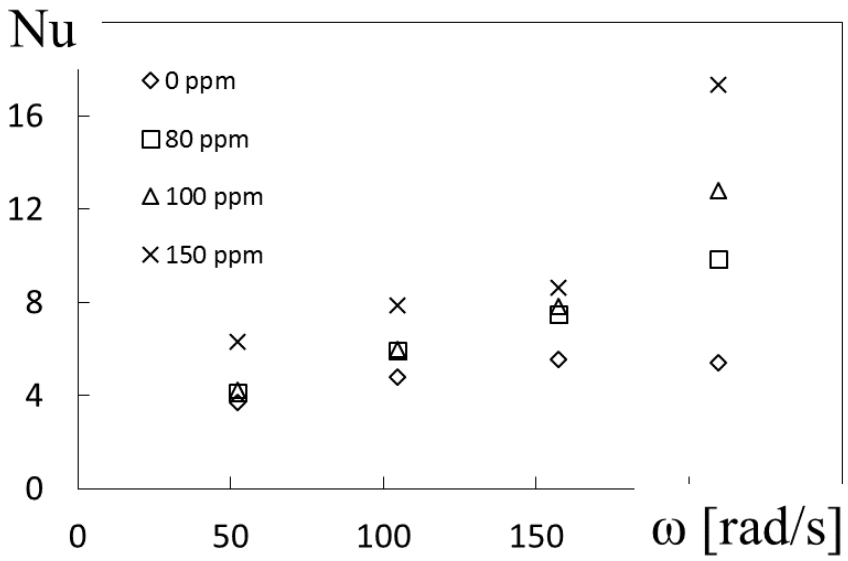

Figure 3.8. Overall Nusselt number variations with viscous disk pump rotational speed for different polymer concentrations.

As such, the elastic instabilities increase heat transfer by approximately 240 percent for the sucrose solution with a 150 ppm polymer concentration (relative to the Newtonian, sucrose solution with ρ_c=0 ppm, when compared at the same disk rotational

speed). Abed et al. (2016) describe enhancements as large as 380 percent for sucrose solutions with 500 ppm polymer concentrations. Those investigators attribute such enhancements to the elastic turbulence generated by non-linear interactions between elastic normal stresses created within the flowing high-molecular-weight polymer solution, and the streamline curvature of a serpentine channel.

3.6 Variations of Mean-Square of Temperature Fluctuations

Such increased mixing, and speculated increases of polymer interactions and agitation, are further illustrated by variations of mean square magnitudes of flow temperature fluctuations (measured at the viscous disk pump passage exit). These data are given in Figures 3.9 and 3.10. Within Figure 3.9, these data are given as they vary with polymer concentration for rotational speeds Ω of 500 RPM, 1000 RPM, 1500 RPM, and 2000 RPM (or 52.36 radians/s, 104.7 radians/s, 157.1 radians/s, and 209.4 radians/s), and respective shear rates of 146.0 1/s, 292.1 1/s, 438.1 1/s, and 584.2 1/s. Figure 3.10 then presents data as they vary with disk rotational speed for the viscous disk pump for polymer concentrations of 0 ppm, 80 ppm, 100 ppm, and 150 ppm. As such, unsteady temperature fluctuations offer an appropriate means to characterize flow mixing and small-scale interactions because, like dye concentrations, temperature is a passive scalar. Consequently, both quantities are influenced by similar advection and diffusion transport phenomena.

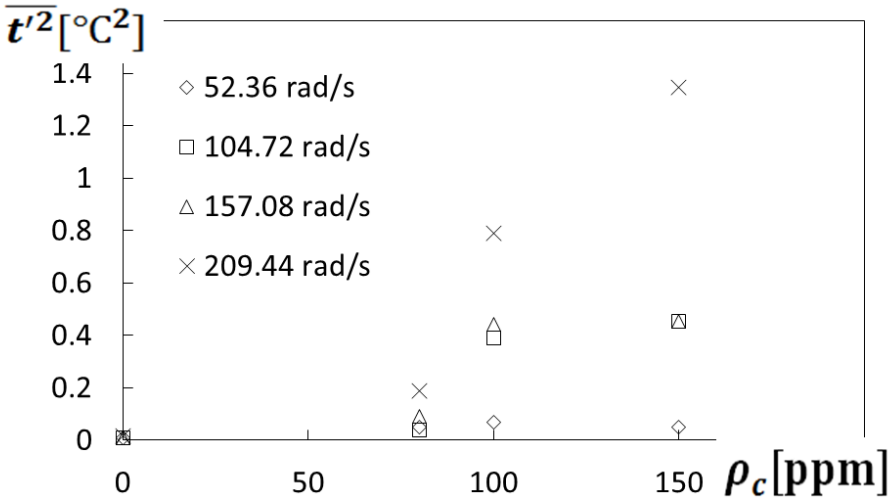

Figure 3.9. Variations of mean-square magnitudes of flow temperature fluctuations with polymer concentration for different viscous disk pump rotational speeds.

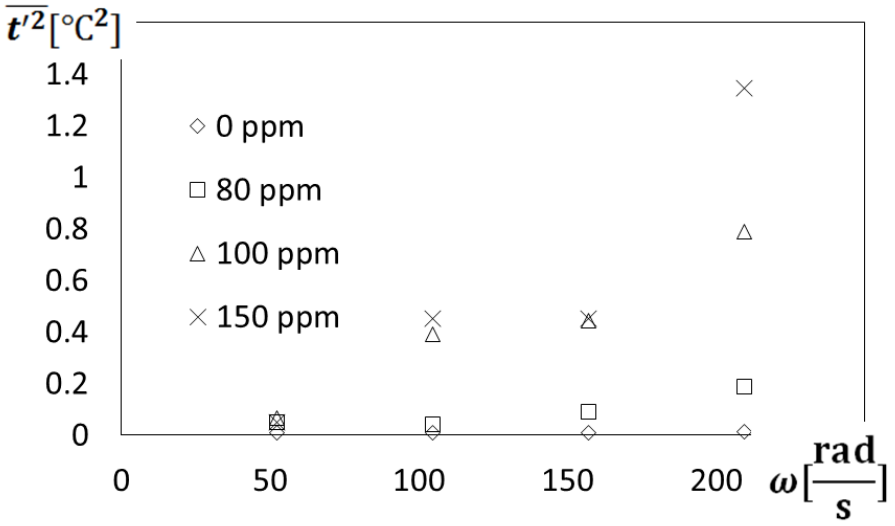

Figure 3.10 Variations of mean-square magnitudes of flow temperature fluctuations with viscous disk pump rotational speed for different polymer concentrations.

.

Dramatic $\overline{t'^2}$ increases are evident in Figure 3.9 as polymer concentration increases, especially for disk rotation speeds greater than 100 radians/s. These changes to

$\overline{t'^2}$ with ω and ρ_c are further confirmed by the results which are presented in Figure 3.10. Regardless of the rotational speed of the disk, and the associated shear rate, the lowest dimensional magnitudes of $\overline{t'^2}$ are always associated with the Newtonian, sucrose solution fluid, wherein ρ_c=0 ppm. As such, the changes resulting from increasing ω and ρ_c are associated with increased flow irregularities and unsteadiness, which are believed to result from polymer twisting and convolutions. As such, the present $\overline{t'^2}$ data illustrate local chaotic fluid motions associated with the onset and development of elastic instabilities.

3.7 Power Spectra of Fluctuating Temperature

The frequency content of the unsteady temperature fluctuations is illustrated by the results in Figure 3.11. These data are given for a rotational speed Ω of 1500 RPM (or 157.1 radians/s), a shear rate of 438.1 1/s, and for different polymer concentrations. Included is one data set for a Newtonian, sucrose solution fluid, wherein ρ_c=0 ppm. From these data, it is evident that the polymer solutions exhibit higher spectral magnitudes over broad-band frequencies. In addition, wider and more pronounced spectral peaks are present at different frequencies, especially in the vicinity of 10^{-1} Hz. The dramatic differences in the power spectra between polymer solutions and Newtonian, sucrose solution are believed to be caused by flow fluctuations over a range of frequencies resulting from elastic instabilities.

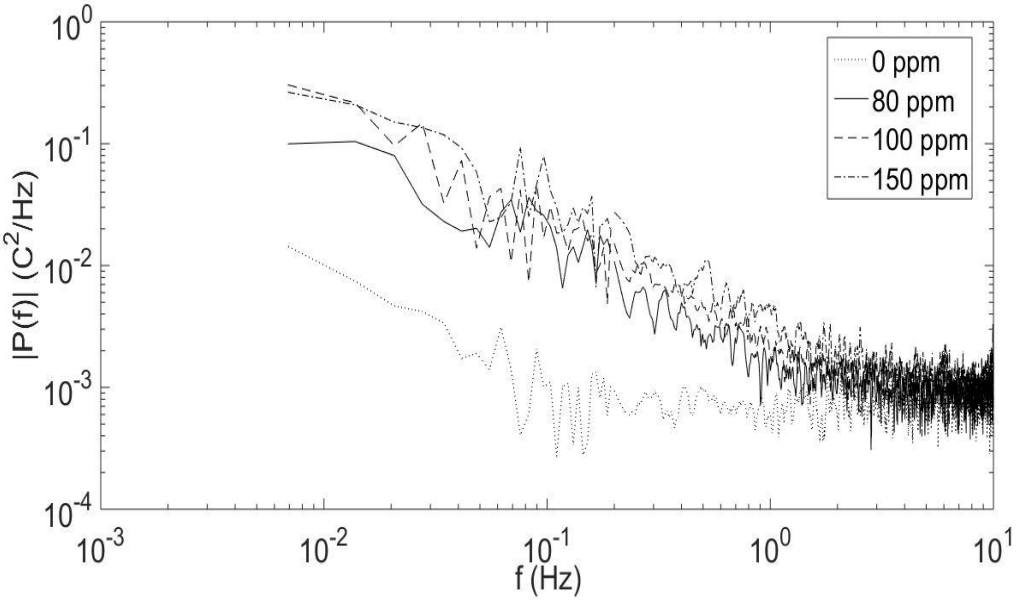

Figure 3.11 Power spectra of temperature fluctuations as they vary with polymer concentration at a shear rate of 438.1 1/s.

CHAPTER 4

EXPERIMENTAL APPARATUS AND PROCEDURES FOR ROTATING COUETTE FLOW

This chapter consists of six parts: (1) rotating Couette flow configuration and operation; (2) polymer solution preparation; (3) flow visualization apparatus and procedures; (4) heat transfer and fluctuating temperature measurement apparatus and procedures; (5) analytic determination of Nusselt numbers and heat transfer coefficients; and (6) experimental uncertainty magnitudes. Details on the experimental apparatus and procedures are described, including all relevant measurement details.

4.1 Rotating Couette Flow Configuration and Operation

The experimental device developed to investigate Rotating Couette flow is shown schematically in Figures 4.3a and 4.3b. The associated cylindrical coordinate system is then presented in Figures 4.3a and 4.4. Here, the z coordinate is directed in a normal direction from the bottom surface of the cup flow container, and the r coordinate is directed from the center of rotation. Included is an adjustable rotating disk, manufactured from PEEK plastic, with a radius of 38.1 mm. The disc is located within a cylindrical cup flow container, with an inner radius of 43.5 mm, which is contained within a custom-made aluminum housing. The height of the disk, or the distance between the disk bottom surface and the top surface of the cup flow container, is measured using a Mitutoyo

absolute depth gauge. This gauge is mounted onto the vertical surface of the sliding part of the assembly, as shown within the photograph of the experimental apparatus in Figure 4.1. The disk height is the same as the depth of the Rotating Couette Flow passage, H, which is set to 5.0 mm for the present investigation. The Rotating Couette Flow arrangement is employed because magnitudes of shear rate imposed on the flow (at a particular radial location) are readily selected by setting disk rotational speed and the height of the flow passage. In addition, with RCF, shear is applied to the flow without any streamwise pressure gradient.

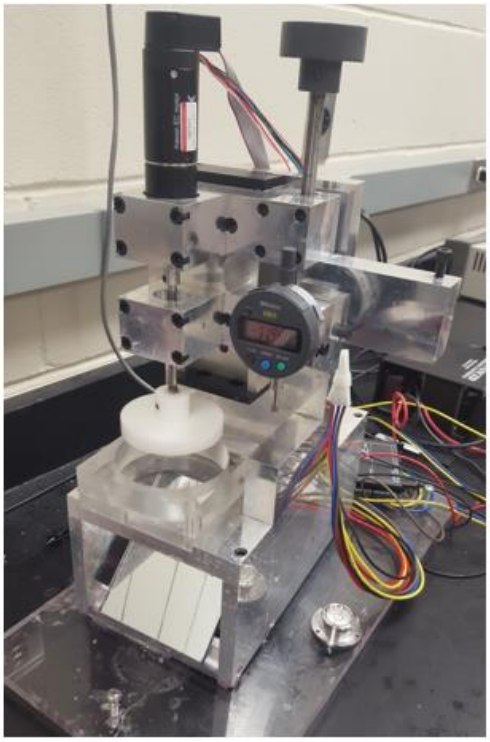

Figure 4.1 Photograph of visualization set-up for Rotating Couette Flow.

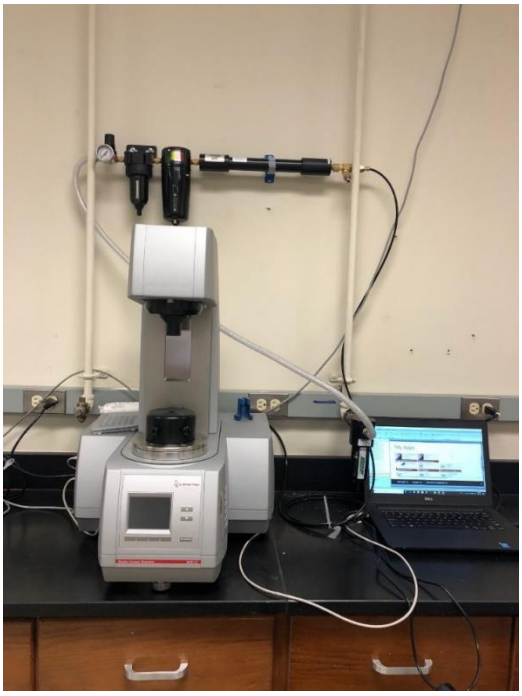

Figure 4.2 Photograph of Anton-Paar 92002 MCR 302 Modular Compact Rheometer.

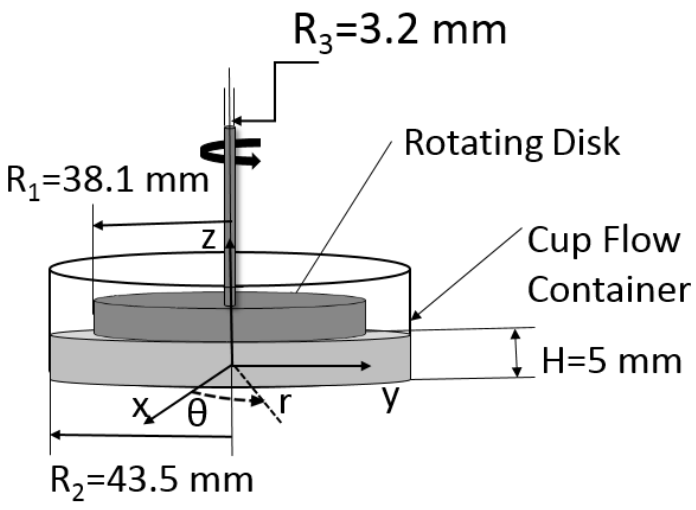

(a)

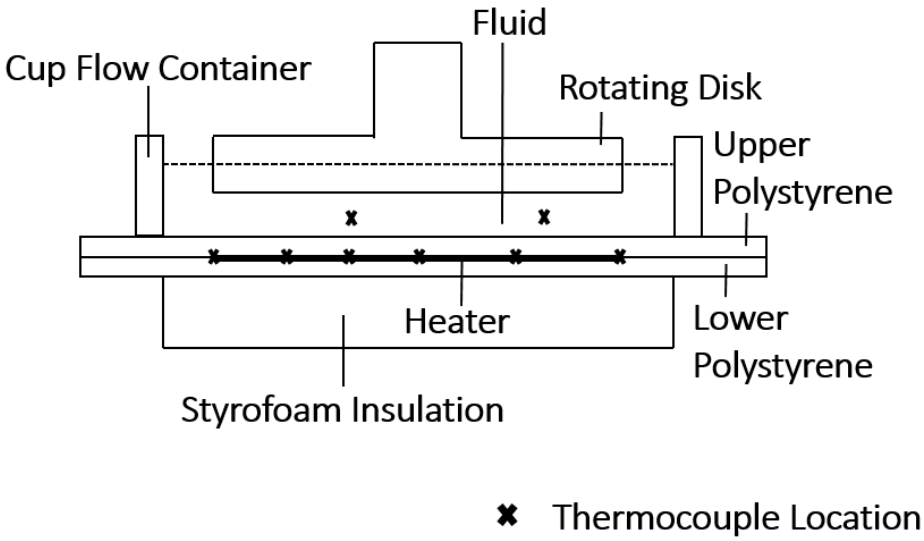

(b)

Figure 4.3 (a) Overall concept and dimensions of Rotating Couette Flow device. (b) Arrangement of heat transfer measurement apparatus, including thermocouple and heater locations. Note that thermocouples are located both above and below the heater at each surface location.

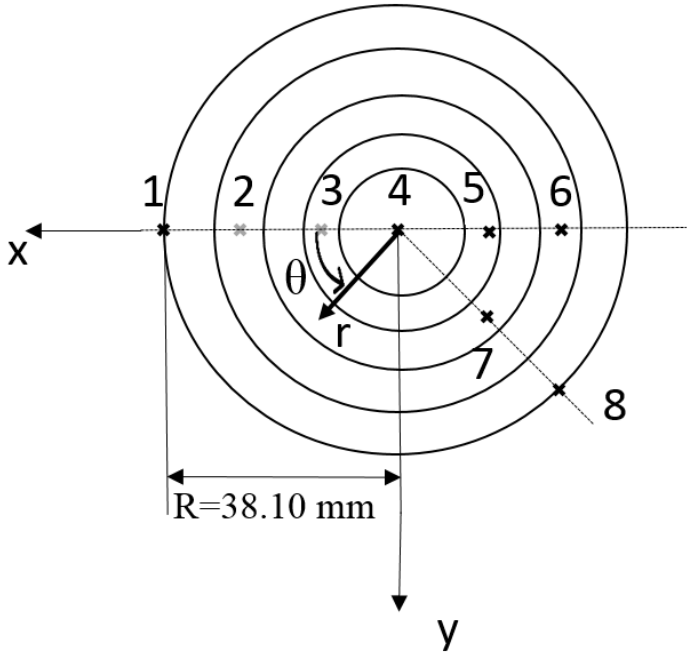

Thermocouple Location		Radial Location r (mm)	Circumferential Angle θ (º)
Surface Temperature	1	38.10	0
	4	0.00	180
	5	12.70	180
	6	25.40	180
	7	17.96	135
	8	38.10	135
Flow Temperature	2	25.40	0
	3	12.70	0

Figure 4.4 Thermocouple measurement locations. Note that thermocouples are located both above and below the heater at surface locations 1, 4, 5, 6, 7, and 8.

The rotation of the disk is powered by an externally mounted Maxon EC32 #118890 motor. The motor has a 48V winding, a power rating of 80W, a maximum speed of 25,000 RPM, and a stall torque of 0.353 Nm. The motor is geared to allow for disk rotation speeds ranging from approximately 1 to 250 RPM or 0.105 to 26.180 radians/sec. The motor is controlled by a Maxon ESCON 50/5 #409510 motor controller connected to

an Advanced Motion Controls model PS2X3W48 power supply. The power supply has a DC supply voltage of 48V, a peak current of 12 amperes, and a continuous current rating of 6 amps. The motor controller maintains a constant speed through a closed control loop and a Maxon HEDL 55 Encoder #110514. The speed and direction of the motor are controlled by regulating voltage to the analog and digital I/O channels on the motor controller using LABVIEW 32-bit software, version 10.0.1, and a National Instruments USB6003 data acquisition board. The rotational speed measurement system is calibrated using a timing light.

4.2 Polymer Solution Preparation

Five different solutions are utilized with four different polymer concentrations: 0 ppm, 80 ppm, 100 ppm, 150 ppm, and 300 ppm, where ppm refers to parts per million. As such, the 0 ppm arrangement is utilized with a 65 percent sucrose solution (without added polymers) as a solvent solution. The viscoelastic solutions are then prepared by adding polyacrylamide powder into the sucrose solution. When each solution is prepared, the appropriate polymer concentration (as quantified using PAAm) is employed, along with 1 percent NaCl, and 65 percent sucrose. The procedure for mixing the stock solution is adopted from Abed et al. (2016). For example, to mix an 80 ppm solution, 0.048g of PAAm powder (Polyacrylamide from Dalton, Polysciences Inc. with molecular weight MW of 18,000,000 g/mol), 6 g of NaCl, and 390 g sucrose are dissolved in 204 g DI water. After each solution is prepared, it is gently combined for approximately 1 hour to provide a homogeneous mixture, using a JJ-1 Accurate Electronic Overhead 100 W Stirrer Mixer, with a propeller operating at very low rotational speed.

Polymer mixture rheological data are obtained using a state-of-the-art commercial Anton Paar 92002 MCR 302 Modular Compact Rheometer with a sample-adaptive motor controller and normal force sensor, as shown in Figure 4.2. These data are employed to provide information regarding absolute viscosity properties of the different fluids which are used for testing at different magnitudes of shear rate. The resulting measured values are given in Table 4.1, and are generally in quantitative agreement with values from Abed et al. (2016). Note that, within Table 4.1, several thermophysical properties are obtained from Abed et al. (2016). Within Table 4.1, it is evident that absolute viscosity values at zero shear rate are slightly larger than values associated with higher, non-zero shear rates (where absolute viscosity is approximately constant with shear rate). As such, the present polymer solutions exhibit mild shear-thinning behavior (near zero shear rate), which is consistent with results presented by Abed et al. (2016).

Table 4.1 Physical properties of working fluids.

ρ (ppm)			**0**		**80**		**100**		**150**		**300**	
ρ_d (kg/m^3)			1311		1315		1315		1315		1316	
k_f (W/m·K)			0.368		0.368		0.368		0.368		0.368	
c_p (J/kg·K)			2600		2600		2600		2600		2600	
η_0 (Pa·s)			0.187		0.220		0.287		0.345		0.439	
η_∞ (Pa·s)			-		0.200		0.200		0.280		0.330	
a			-		0.200		0.300		0.100		0.050	
λ_{CY}			-		0.546		0.490		0.655		0.230	
n			0.000		0.421		0.564		0.305		0.310	
λ (s)			0.000		1.120		1.415		1.893		2.809	
Ω (RPM)	ω (rad/s)	$\dot{\gamma}$ (1/s)	μ (Pa·s)	Re	μ (Pa·s)	Re	μ (Pa·s)	Re	μ (Pa·s)	Re	μ (Pa·s)	Re
0	0.000	0.000	0.187	0.00	0.220	0.00	0.287	0.00	0.345	0.00	0.439	0.00
15	1.571	7.980	0.185	0.71	0.204	0.64	0.221	0.59	0.280	0.47	0.336	0.39
20	2.094	10.640	0.185	0.94	0.203	0.86	0.215	0.81	0.280	0.63	0.335	0.52
25	2.618	13.299	0.185	1.18	0.202	1.08	0.214	1.02	0.279	0.78	0.335	0.65
30	3.142	15.959	0.185	1.41	0.201	1.31	0.213	1.23	0.279	0.94	0.334	0.79
40	4.189	21.279	0.185	1.89	0.201	1.75	0.212	1.65	0.279	1.25	0.333	1.05
50	5.236	26.599	0.185	2.36	0.200	2.19	0.211	2.07	0.281	1.56	0.333	1.32
60	6.283	31.919	0.185	2.83	0.199	2.64	0.209	2.51	0.281	1.87	0.332	1.58

ρ (ppm)			**0**		**80**		**100**		**150**		**300**	
Ω (RPM)	ω (rad/s)	$\dot{\gamma}$ (1/s)	Wi	Gz	Wi	Gz	Wi	Gz	Wi	Gz	Wi	Gz
0	0.000	0.000	0.0	0.0	0.0	0.0	0.0	0.0	0.0	0.0	0.0	0.0
15	1.571	7.980	0.0	22.8	8.9	29.2	11.3	29.0	15.1	25.6	22.4	26.1
20	2.094	10.640	0.0	30.4	11.9	39.2	15.1	40.0	20.1	34.2	29.9	34.8
25	2.618	13.299	0.0	38.0	14.9	49.1	18.8	50.0	25.2	42.8	37.4	43.6
30	3.142	15.959	0.0	45.6	17.9	59.2	22.6	60.2	30.2	51.4	44.8	52.3
40	4.189	21.279	0.0	60.8	23.8	79.1	30.1	80.8	40.3	68.6	59.8	70.0
50	5.236	26.599	0.0	76.0	29.8	99.2	37.6	101.2	50.4	85.2	74.7	87.7
60	6.283	31.919	0.0	91.2	35.7	119.6	45.2	122.8	60.4	102.3	89.7	105.5

4.3 Flow Visualization Apparatus and Procedures

Figure 4.5 shows the arrangement and dimensions of flow visualization measurement apparatus. The pump housing block and cup flow container are made from optically clear acrylic. A mirror is placed at an angle of 45^o under the cup to reflect the

images of the flowing solution. The acrylic is polished using NOVUS plastic polish to remove any tooling marks and blemishes. A Point Gray Research Inc. CMLN-13S2C-CS USB digital camera, with a 25 mm video lens, captures images of the channel at a rate of 1.0 frame per second for a period of 10 minutes. The images are saved as 8-bit indexed .bmp image files. The entire device is placed on a piece of horizontal stainless plate, such that the entire rotating Couette flow experimental assembly is placed on a level surface to ensure that there are no height variations throughout the flow passage.

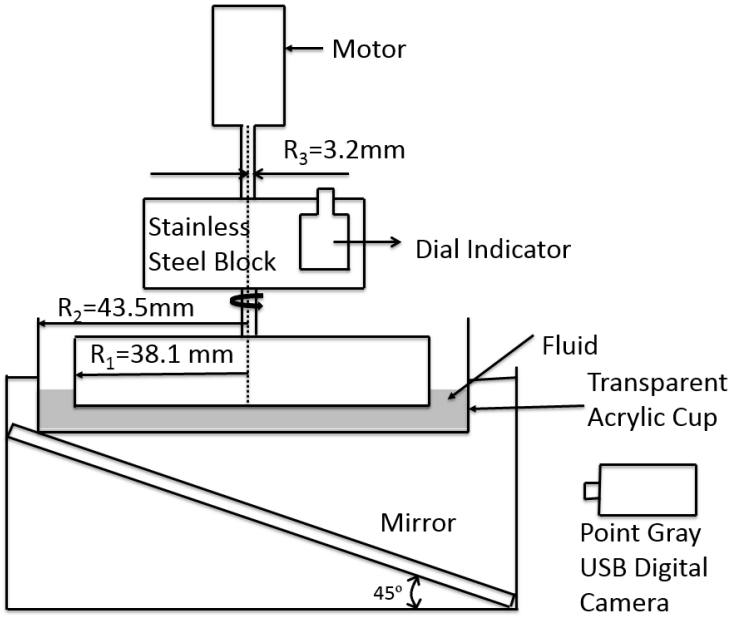

Figure 4.5 Arrangement and dimensions of flow visualization measurement apparatus.

To provide contrast in the channel, Kingscote Inc. flourescein FWT red tracer dye is injected into the channel with a New Era Pump Systems NE-1000 syringe pump at rates ranging from 0.001 to 0.065 milliliters per minute. Dye with 5 percent concentration is employed for this purpose, within the same polymer/sucrose solution which is used for testing. The flourescein particles which constitute this dye, have a molecular weight MW

of 332 g/mol, and an average hydrodynamic radius of 5.02×10^{-10} m. The syringe employed is 28.58 mm in diameter, and is connected through tubing to a needle, which is then inserted into the hole, with a diameter of 0.5 mm, which is located within the sidewall of the cup flow container. Silicone sealant is added around the outside edge of the hole, as needed, to prevent flow leakage.

As flow visualization data are collected, the first step is to place the empty cup flow container within the flow fluid apparatus. The cylindrical disk (with no rotation imposed) is lowered until it touches the bottom of the cup. The height gage is then zeroed, with the disc touching the cup, to provide an appropriate reference for the gap height measurement. The disk bottom surface is then adjusted to a specific height, slowly, after filling the cup with an appropriate amount of fluid solution. As this is done, great care is taken to prevent any air bubbles from being trapped on the underside of the disc. Note that the prepared flow solution is initially held in a separate dry and clean container which is free of contaminants. With this arrangement and process completed, the co-axial rotating disk is just touching the surface of the fluid solution, which is contained within the cup flow container. To provide flow contrast, an appropriate amount of dye is then injected into the center of the RCF passage, at a height of approximately 2 mm from the surface of the cup flow container. This process is undertaken so that no air bubbles are trapped within the needle or syringe pump assembly. This needle is then removed quickly and smoothly without imposing any disturbances or streaking to the initial dye distribution. Motor and disk rotation and camera data acquisition are then started simultaneously. Subsequent visualization data, for a particular experimental configuration and condition, are then recorded.

4.4 Heat Transfer and Fluctuating Temperature Measurement Apparatus and Procedures

Within the present study, the RCF configuration is employed for measurement of spatially-averaged heat transfer coefficients and Nusselt numbers over portions of the flow passage surface area. As for the flow visualization apparatus, the facility consists of a rotating disk and a stationary cylindrical cup flow container, with a round flat commercially-manufactured thermo-foil heater at the bottom, which is mounted between two polystyrene layers. The rotating disk is machined from PEEK plastic, with a thermal conductivity of 0.252 W/(m·K) to minimize heat loss from the top of the Rotating Couette flow passage. PEEK plastic is also selected for this application because minimal shape variations occur as the material is subject to temperature gradients. The two polystyrene layers are also designed to contain and mount a number of thermocouples for measurement of solid material and surface temperatures. Each polystyrene layer is machined with channels for installation of thermocouple wires which lead to thermocouple junctions, which are positioned at different test surface locations. The polystyrene layers are attached to an acrylic holder which is designed to be tightly held on top of a steel mounting block. There are two thread holes at the corners of the polystyrene layers so that each one is tightly secured to the block. The cup flow container is comprised of a copper ring, with a low-conductivity, white Derlin/Acetal AF100 plastic ring positioned just above it. The copper ring is attached to the facility mounting block using epoxy. A total thickness of 19 mm of Styrofoam is attached at the bottom of the apparatus, beneath the bottom polystyrene layer, to minimize associated heat transfer losses. A photograph of the apparatus employed for heat transfer measurements and

analysis is presented in Figure 4.6. Thermophysical property values of component materials, employed within the heat transfer test surface, are given in Table 4.2.

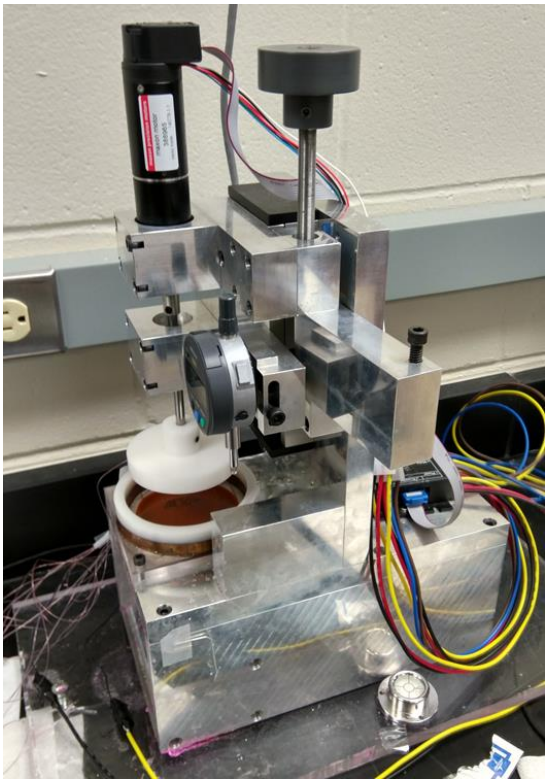

Figure 4.6 Photograph of experimental apparatus employed for heat transfer measurements and analysis.

Table 4.2 Thermophysical property values of component materials.

	Density (g/cm^3)	Specific Heat (kJ/kg·K)	Thermal Conductivity (W/m·K)
PEEK Plastic	1.31	0.32	0.252
Copper	8.93	0.385	385.0
Polystyrene	1.03 – 1.07	1.50	0.170
Styrofoam	0.035	1.13	0.033

Local surface Nusselt numbers are measured on the heated and instrumented plate. Arrangement and dimensional details of a cross-section of this plate are shown in Figure 4.7. Here, each polystyrene layers is 1.248 mm thick, and the attached, internal heater is approximately 0.127 mm thick, giving a total target plate thickness of 2.623

mm. The radius of the circular heater is 38.1 mm. The Omega Inc. Kapton/polyamide, KHR-315-P thermo-foil heater provides an approximately constant surface heat flux boundary condition on the bottom surface of the Rotating Couette Flow passage. The heater is supplied by a BK precision XLN15010 DC power supply, which is directed by a switchboard, covered in a clear plastic box (for safety), where the voltage is read by a Keysight 34401A Digital Multimeter, and amperage is read by both a Simpson 260 Series 8p Ammeter and a Fluke 8845A Digital Precision Multimeter.

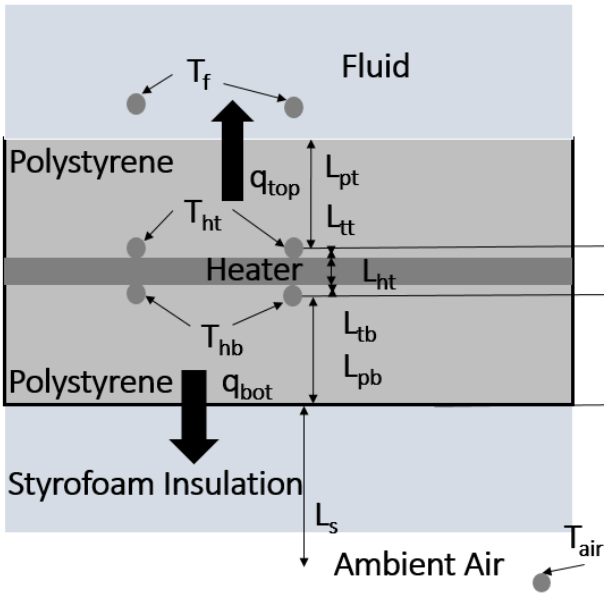

L_{pt}	1.208 mm
L_{tt}	0.040 mm
L_{ht}	0.127 mm
L_{tb}	0.040 mm
L_{pb}	1.208 mm
L_s	19.000 mm

Figure 4.7. Arrangement and dimensions of test surface of heat transfer measurement apparatus.

Thermocouple locations for measurement of flow and surface temperatures, along with areas employed for heat transfer analysis, are shown in Figure 4.4. Flow and component surface temperature measurements are made using Omega 5TC-TT-T-40-72 fine-wire copper-constantan (type T) thermocouples. The diameter of the thermocouple insulation is 0.4 mm. Each thermocouple wire is 0.08 mm in diameter. With the procedures employed, the thermocouples have a time-averaged measurement accuracy of 0.05ºC to 0.10ºC, and are calibrated in the range 20ºC to 44ºC using an HCTB-3020 Omega Thermo-Regulator, which is a constant temperature water bath. A Fluke Hart 1523 Thermometer and stainless steel sheathed thermistor (which is accurate within ±0.01 oC) are employed to measure bath temperature. As shown in Figure 4.4, twelve of these thermocouples are located adjacent to the top and bottom surfaces of the heater (with six on each side), and two thermocouples are located within the flow at mid-passage height. Four additional thermocouples are located within the copper side wall of the cup flow container, to determine side wall heat loss. These thermocouples are positioned at 5.66 mm and 8.99 mm locations, relative to the bottom surface of the flow passage. Figure 4.4 shows that the two thermocouples used to measure flow static temperature are positioned at $1/3R_1$ and $2/3R_1$, where R_1 is the heater radius, equal to 38.10 mm. Each flow thermocouple location is positioned using a thin, rigid steel rod, which is installed and oriented to prevent thermocouple junction movement, and to insure that each flow thermocouple is installed precisely at the mid-height of the flow passage. The frequency response of each thermocouple junction, which is employed for the flow static temperature measurements, is estimated to be approximately 3×10^{-3} seconds, which is approximately equivalent to 334 Hz.

Each thermocouple is connected to a National Instruments 9213 thermocouple card, which is connected to a NI USB-9162 high speed USB carrier data acquisition card. Both of these devices are mounted within a National Instruments NI cDAQ-9188 chassis. Information from these terminals is acquired using a Dell Precision T1700 computer through its USB port, using LABVIEW 32-bit software, version 10.0.1 software. In order to determine time-averaged and fluctuating temperatures in the flow, the system is allowed to reach steady state, and instantaneous flow temperatures are recorded over a period of 10 minutes at a frequency of 50 Hz, giving a total of 30,000 data points. Steady-state conditions are indicated by flow and surface temperature levels which are invariant with time, within associated experimental uncertainty magnitudes. The mean square of fluctuating temperature, relative to the time-averaged temperature, is determined using EXCEL Version 2013 software. To determine power spectra of fluctuating static temperature, the FFT subroutine of MATLAB Version R2017a software code is employed. Utilized is a Fast Fourier Transform (FFT) applied to instantaneous time-varying temperature data. A central-moving average filter is used to smooth the resulting spectral data at frequencies greater than 10^0 Hz, and an anti-aliasing, low-pass filter is also applied to the time sequence of digital data. In addition, magnitudes of background, electronic "white" noise are removed from spectral amplitudes over all measured frequencies. With these procedures, accurate information is provided of the frequency content of fluctuating flow static temperature, for all frequencies which are associated with significant unsteady temperature energy content.

4.5 Analytic Determination of Nusselt Numbers and Heat Transfer Coefficients

Figure 4.7 shows the arrangement and dimensional details of a cross-section of the plate which is employed to measure surface magnitudes of heat transfer coefficients and Nusselt numbers. As a first step, the heater power P is adjusted to be 2.314 Watts, as measured and verified using the procedures described in the previous section. All of the associated heat power is transferred upwards into the flow, or downwards through the layers of polystyrene and Styrofoam, and then, into the surrounding laboratory environment. The magnitude of heat power (transferred downwards) to the environment is determined using the expression given by

$$q_{bot} = \frac{T_{hb} - T_{air}}{(\frac{L_p}{K_p A} + \frac{L_s}{K_s A})} \tag{4.1}$$

The magnitude of heat power transferred upwards from the test surface, and then, into the flow is subsequently determined using the equation given by

$$q_{top} = P - q_{bot} \tag{4.2}$$

Within these equations, T_{hb} is the heater temperature at the bottom of the heater, T_{air} is ambient air temperature (note that associated thermocouple locations are shown in Figure 4.7), L_p is the thickness of the polystyrene plate, L_s is the thickness of the Styrofoam insulation, K_p is the thermal conductivity of the polystyrene, K_s is the thermal conductivity of the Styrofoam, and A is the area of the heater, equal to 4.56×10^{-3} m^2. As mentioned, thermophysical property values of these component materials are given in Table 4.2.

The temperature measured at the top of the heater, T_{ht}, is then employed to determine T_t, the temperature of the polystyrene surface which is adjacent to the Rotating

Couette Flow. As mentioned, associated thermocouple locations, relative the heat transfer surface cross-section, are shown in Figure 4.7. The expression employed for this purpose is of the form

$$T_t = T_{ht} - \frac{L_p q_{top}}{K_p A} \tag{4.3}$$

Local static fluid temperature at the mid-height of the flow passage is then denotedT_f. Locations for measurement of T_f and T_t, relative to the plane of the heat transfer surface, are then shown in Figure 4.4. With this information, the local heat transfer coefficients are determined using

$$h = \frac{q_{top}}{A(T_t - T_f)} \tag{4.4}$$

The characteristic length for the Nusselt number is the flow passage height, H, which is 5 mm. Local Nusselt numbers are then given by

$$Nu = \frac{hH}{K_f} \tag{4.5}$$

Within this equation, K_f is then the thermal conductivity for the polymer solution which is employed.

4.6 Experimental Uncertainty Magnitudes

Experimental uncertainty magnitudes associated with experimentally measured temperature, Nusselt number, and mean-square of temperature fluctuations are presented in Table 4.3. Within this table, values are given for the sucrose-based solvent fluid, as well as for solutions with four different polymer concentrations. Values are obtained using an nth-order uncertainty analysis, with a constant-odds combination method, based on a 95% confidence level, using procedures which are described by Moffat (1988).

Table 4.3 Uncertainty values of experimental parameters associated with heat transfer measurements, as they vary with polymer concentration.

Concentration (ppm)	Time-averaged temperature	Mean-square of fluctuating temperature	Nusselt number
0 (Sucrose Solution)	8.4%	5.6%	5.1%
80	6.9%	9.2%	7.8%
100	6.6%	7.4%	6.3%
150	5.9%	6.1%	5.5%
300	5.4%	5.9%	5.1%

CHAPTER 5

EXPERIMENTAL RESULTS: ROTATIONAL COUETTE FLOW

This chapter consists of six parts: (1) analytic characterization of elastic instability onset; (2) flow visualization results and conditions for the onset of elastic instabilities; (3) overall viscosity data and polymer relaxation time; (4) transition onset of elastic instabilities; (5) Nusselt number and flow static temperature variations; (6) Nusselt number variation with Reynolds number, Graetz number, Weissenberg number, and McKinley transition number.

The remarkable ability of viscoelastic fluids to augment local and global surface heat transfer characteristics is demonstrated by new experimental results, which are provided for a Rotating Couette Flow (RCF) environment (also referred to as von Karman swirling flow) with convective heat transfer. The overall heat transfer rate is determined with a specially-constructed heat transfer test surface, with a constant surface heat flux thermal boundary condition. Included are Nusselt number variations, flow visualization results, and spectral analysis of flow static temperature fluctuations. Augmented surface Nusselt numbers are measured for sucrose-based, viscoelastic solutions with polyacrylamide (as they are subject to different magnitudes of flow strain), relative to viscoelastic, Boger solution flows, without significant Nusselt number augmentations present. The resulting Nusselt number enhancements are related to the experimental

conditions which are believed to be associated with the onset and development of elastic instabilities. Four different analytic instability onset parameters (Reynolds number, Graetz number, Weissenberg number, McKinley et al. parameter) are then employed to predict these experimental conditions, in order to determine their viability to represent the associated flow physics. Resulting comparisons show that the Weissenberg number is the parameter which best correlates and characterizes Nusselt number augmentations, which are strongly correlated with pronounced redistributions of fluorescein FWT red tracer dye fronts, obtained from flow visualizations. As such, the present investigation provides new insight into thermal transport of viscoelastic fluids, and new experimental data which illustrate the utility of different analytic and numerical models for predicting experimental conditions associated with significant Nusselt number augmentations.

5.1 Analytic Characterization of Elastic Instability Onset

The McKinley et al. (1996) model is employed to characterize the onset of elastic instabilities, when streamline curvature is present, within different flow configurations and different polymer concentrations. The associated criterion applies to the onset of pure elastic instability, rather than the onset of elastic turbulence. Additional discussions of flow characteristics associated with pure elastic instability are provided by De Gennes (1974) and Larson (1992). Within the latter of these two investigations, Larson (1992) describes non-inertial viscoelastic instabilities in a Taylor-Couette flow with dilute polymer solutions. Pathak et al. (2004) consider purely elastic instability for a Poiseuille flow path, based on flow visualizations. Resulting data show that tracer partials are radially displaced and mixing is promoted, compared to Newtonian fluids. According to these investigators, augmented mixing gives enhanced secondary flows, which promote instabilities within

configurations with curved streamlines. Within such pure shear flows, the major non-linear elastic effect shows up in the appearance of negative normal stress along the flow direction. The result is purely elastic instabilities when inertial effects are either minimal or non-existent.

Within the present study, the McKinley et al. (1996) criterion is expressed using an equation given by

$$[\frac{\lambda U}{R}\frac{\sigma_{11}}{(\eta_0\dot{\gamma})}]^{1/2} \geq M_{crit}$$

Within this equation, the σ_{11} tensile stress value, or first normal stress difference, is estimated using the Oldroyd-B model and is of the form

$$\sigma_{11} = 2\,\eta_p\,\lambda\dot{\gamma}^2$$

Here, each of the following viscosity quantities η_0, η_p, and η_s represent zero-shear-rate property values. Also note that the shear stress for steady simple, shear flow is given by

$$\tau_{12} = (\eta_p + \eta_s)\dot{\gamma}$$

where η_p is the polymeric contribution to the viscosity and η_s is the solvent contribution, so that

$$\eta_0 = \eta_p + \eta_s$$

β is defined as

$$\beta = \frac{\eta_s}{\eta_0}$$

so that

$$\frac{\eta_p}{\eta_0} = 1 - \beta$$

When these are substituted into the original elastic instability onset equation, the expression becomes

$$[\frac{2U\lambda^2\dot{\gamma}(1-\beta)}{R}]^{1/2} \geq M_{crit}$$

For the present Rotating Couette Flow arrangement, the conditions at which elastic instabilities begin to develop, are characterized by fluid velocity and shear rates, which are defined using the following equations

$$U = \frac{\omega R}{2}$$

$$\dot{\gamma} = \frac{\omega R}{H}$$

With these substitutions the elastic instability onset equation becomes

$$\left[\frac{\omega^2 R\lambda^2(1-\beta)}{H}\right]^{\frac{1}{2}} \geq M_{crit}$$

Weissenberg number, Wi, and the Deborah number, Deb, are then defined using

$$Wi = \dot{\gamma}\lambda$$

$$Deb = \omega\lambda$$

Note that the critical Wissenberg number, Wi, at the onset of elastic instability, is based upon the flow condition wherein the polymer stretch rate exceeds the inverse polymer relation time. The above elastic instability onset equation can then be expressed in terms of Wi and Deb using the equation given by

$$[Wi.Deb.(1-\beta)]^{1/2} \geq M_{crit} \quad (5.1)$$

For the present RCF arrangement, M_{crit}=9.288 is employed so that results from Eqn. (5.1) provide the best match to the experimental data given in Figure 5.4, which characterize the onset of elastic instabilities.

5.2 Flow Visualization Results and Conditions for the Onset of Elastic Instabilities

Used as a basis of comparison are: (i) sucrose solvent fluids (with no polyacrylamide present), and (ii) increased-viscosity, viscoelastic, Boger fluids, which generally do not change viscosity as shear rate varies (James, 2009). Comparisons between fluids with different magnitudes of surface Nusselt number augmentation, and these two types of fluids are undertaken as flow location, flow passage height H of 5 mm, and inlet temperature are maintained the same. Comparisons are then generally undertaken either as polymer concentration varies and shear rate is constant, or as shear rate varies and polymer concentration is constant.

Figure 5.1 presents two time-sequences of photographs of visualized flow images, for a sucrose solution with 0 ppm and for a 150 ppm polyacrylamide solution. The first collection of data is provided for a rotational speed ω of 1.57 rad/s and shear rate $\dot{\gamma}$ of 7.98 1/s, and the second is provided for a rotational speed ω of 6.29 rad/s and shear rate $\dot{\gamma}$ of 31.92 1/s. Different distributions of fluorescein red tracer dye are evident within the two time-sequences of data. For the 0 ppm arrangement, dye continues to be concentrated near the center of the disk flow passage, as time increases from 0 minutes to 10 minutes. Here, the dye moves radially outward only very slowly and smoothly, always with an approximately circular distribution, which evidences pure laminar flow. With the 150 ppm polyacrylamide solution, the dye is then dispersed over a much larger area, relative to the center of the flow passage, with progressively increased spatial distributions, which are increasingly irregular and dispersed, as time increases from 0 to 60 seconds (1 minute). With this arrangement, the effective radial diffusion rate of the dye is notably enhanced as flow advects through the flow passage. Here, effective diffusion is used as a descriptive

label, to also account for the presence of circumferential advection. This label is also used because polymer motions associated with elastic instabilities are not a result of true molecular diffusion or Brownian motion.

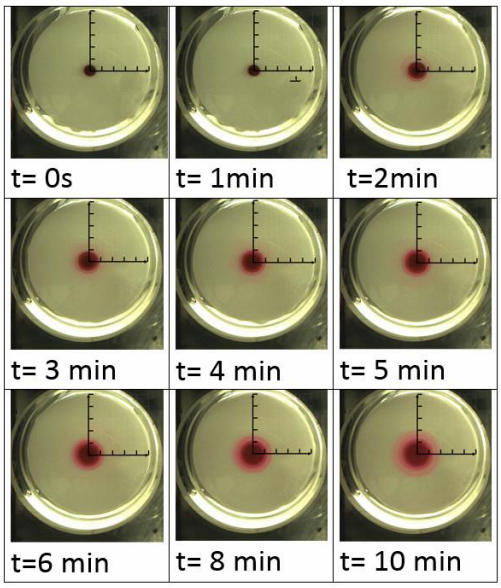

(a)

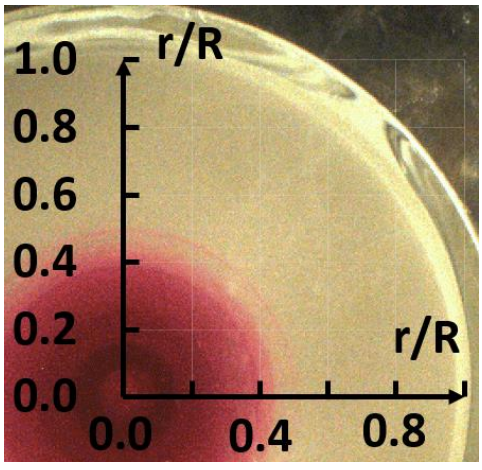

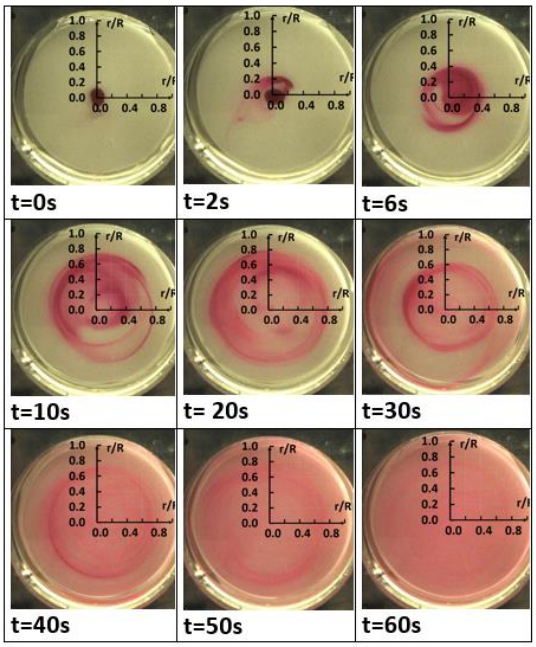

(b)

Figure 5.1 Flow visualization images. (a) Sucrose solution with 0 ppm at a rotational speed ω of 1.57 rad/s and shear rate of 7.98 1/s. (b) 150 ppm polyacrylamide solution at a rotational speed ω of 6.29 rad/s and shear rate of 31.92 1/s.

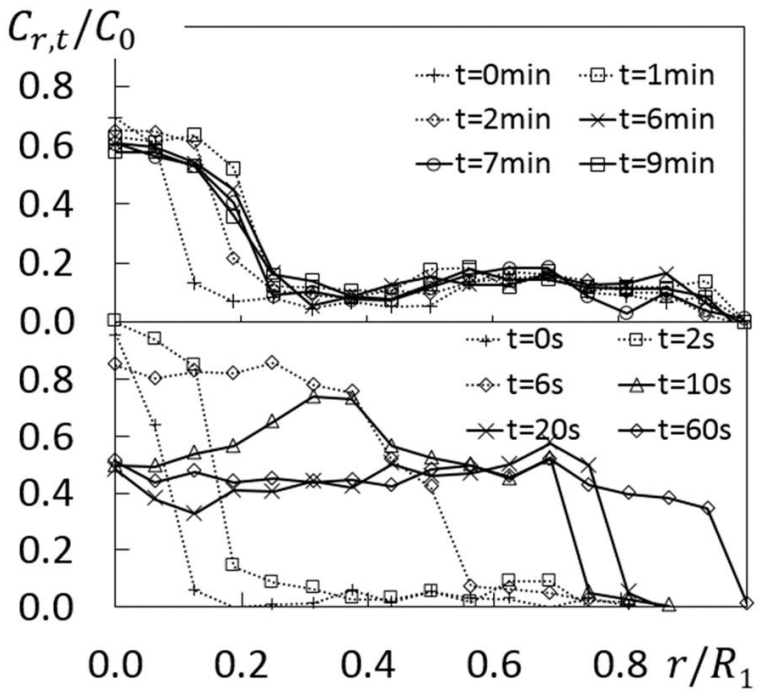

Figure 5.2 Non-dimensional concentration of flourescein red tracer dye as it varies with non-dimensional radius location, for the experimental conditions associated with the data in Fig. 6 for sucrose solutions with 0 ppm and 150 ppm polyacrylamide concentrations.

Experimental data, such as are presented within Figure 5.1, are utilized to construct an experimental domain distribution to illustrate the experimental conditions associated with the onset of elastic instabilities. The first step in the process is determination of the normalized concentration of fluorescein red tracer dye as it varies with non-dimensional radius location, for different times, and for different polymer concentrations. Resulting data are shown in Figures 5.2a and 5.2b, which correspond to the data in Figures 5.1a and 5.1b, respectively, with the 0 ppm and 150 ppm polyacrylamide concentrations. Dye front locations at particular times are then determined from these data where the gradient of fluorescein dye concentration is largest. Resulting non-dimensional dye front location variations with time are then presented in Figure 5.3a.

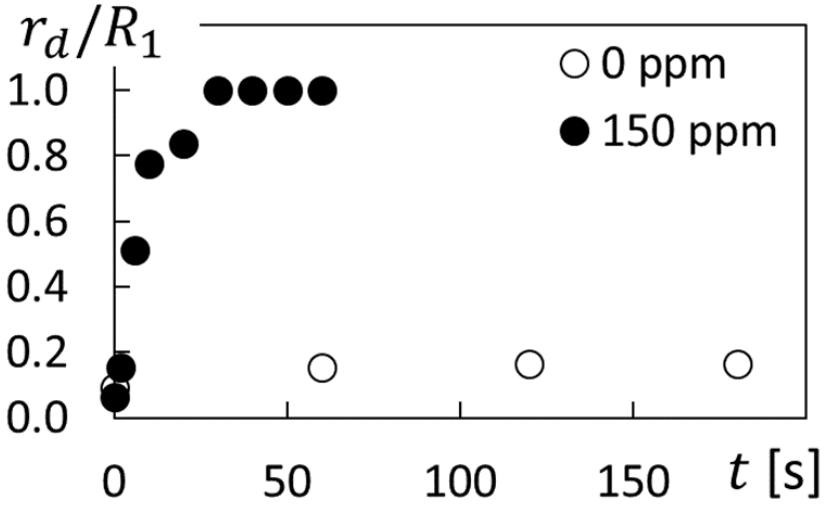

(a)

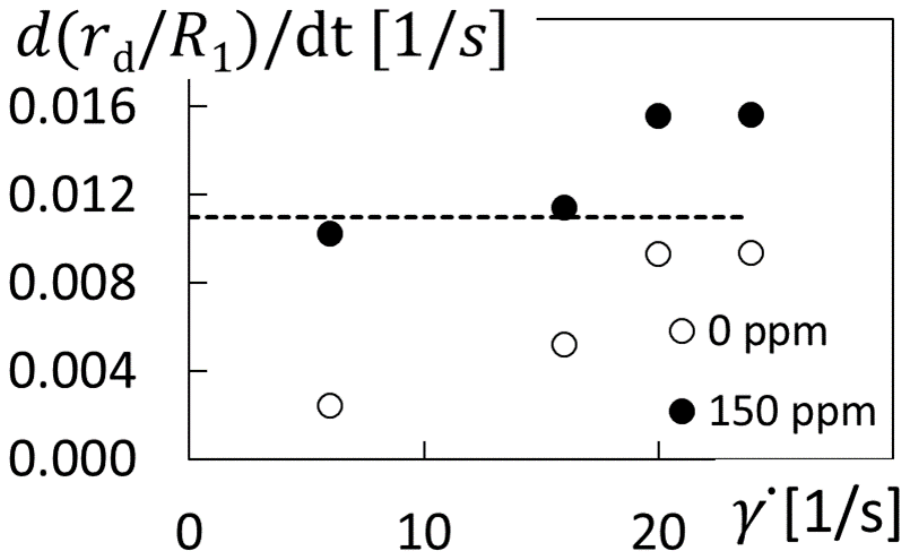

(b)

Figure 5.3 Fluorescein red tracer dye front characteristics for sucrose solutions with different polyacrylamide concentrations. (a) Non-dimensional radial dye front location variations with time for the experimental conditions associated with the data in Fig. 6 for sucrose solutions with 0 ppm and 150 ppm polyacrylamide concentrations. (b) Maximum derivative of non-dimensional radial dye front location variations with shear rate, including threshold of elastic instability onset.

Note that similar data are obtained for all of the experimental conditions illustrated by the data within Figure 5.4, for all polymer concentrations, shear rates, and rotational speeds, which are considered. Maximum derivative magnitudes of non-dimensional location variations are then given in Figure 5.3b for different shear rate values. Onset of elastic instabilities is indicated by derivative magnitudes which exceed 0.011 1/s, because the resulting associated flows are characterized by spectra of flow static temperature fluctuations with broad-band frequency behavior, and significantly higher spectral magnitudes, compared to data obtained at the same shear rate, but with 0 ppm polymer concentrations. Additional discussion of the associated spectra is provided later within the present dissertation.

The resulting experimental domain distribution, which shows experimental conditions which are believed to be associated with the onset of elastic instabilities, is presented within Figure 5.4. Here, data points associated with different types of flow behavior are given as they depend upon shear rate and polymer concentration. Transition conditions, determined from flow visualization data, based upon the $d(r_d/R)/dt=0.011$ dye front threshold, are shown. Resulting data indicate that smaller polymer concentrations are required at higher shear rates to induce the observed increases in flow mixing and chaotic motions. Also included are: (a) the transition conditions associated with a constant Weissenberg number Wi of 30, and (b) the transition conditions associated with the McKinley et al. elastic instability model (McKinley et al., 1996), with viscosity values determined using the present experimental rheometer data.

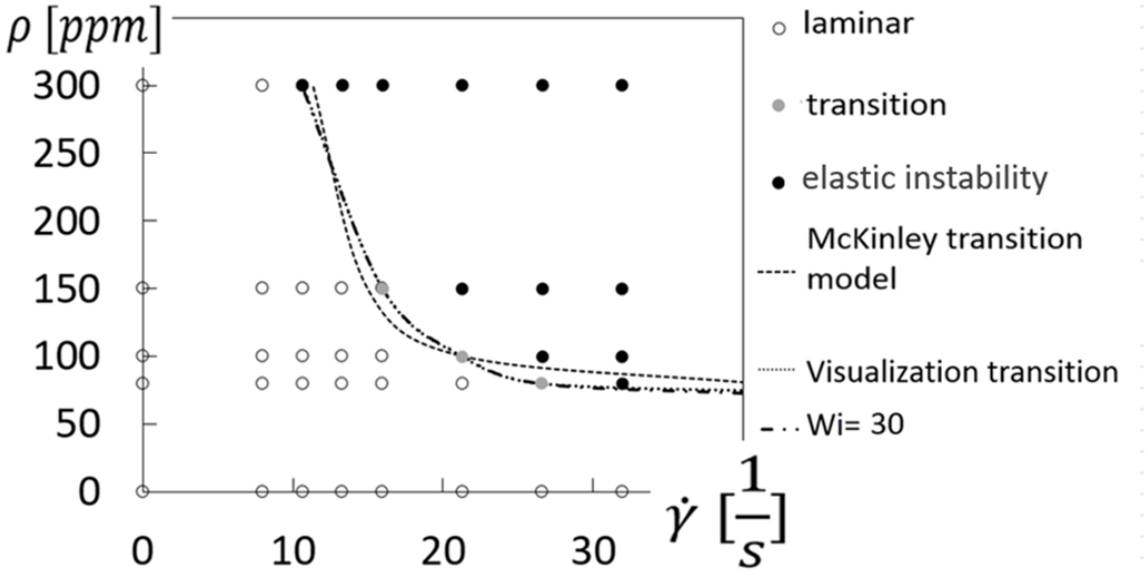

Figure 5.4 Laminar, transition, and elastic instability flow conditions at different shear rates and different polymer concentrations within the Rotating Couette Flow device.

5.3. Overall Viscosity Data and Polymer Relaxation Time

Figure 5.5 presents overall viscosity η data for different polymer concentrations from Anton-Paar rheometer analysis, which compare favorably with viscosity values determined using the Carreau—Yasuda model (Yasuda et al., 1981). These data are generally also in quantitative agreement with results from Abed et al. (2016). Results in Figure 5.5 are presented as they vary with shear rate, and are given for shear rates which are greater than zero. Here, magnitudes of overall viscosity increase with polymer concentration at each value of shear rate. In addition, values are approximately constant as shear rate varies, which is consistent with viscoelastic, Boger fluid behavior (James, 2019) for ρ values of 80, 100, 150, and 300 ppm. A similar trend is evidenced by the sucrose solvent solution, with a ρ value of 0 ppm, which is consistent with Newtonian fluid behavior. The Carreau-Yasuda viscosity model (Yasuda et al., 1981), used to determine overall viscosity values for comparisons with results in Figure 5.5, is given by

$$\eta = \eta_\infty + \frac{\eta_o - \eta_\infty}{[1 + \lambda_{CY}\dot{\gamma}^a]^{n/a}}$$

where a is a fitting parameter, n is a power law index, and λ_{CY} is a parameter representing the inverse shear rate at the onset of shear-thinning behavior.

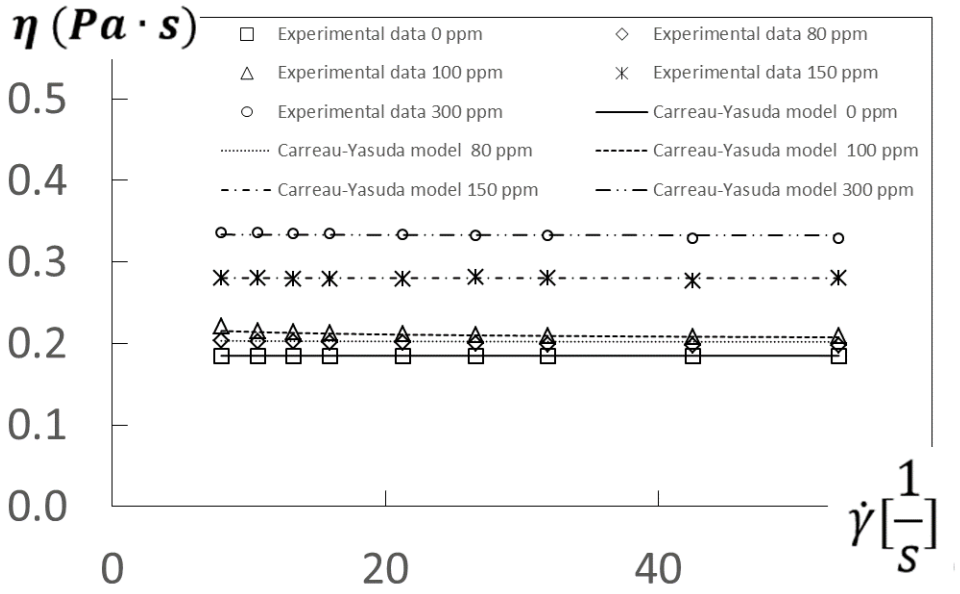

Figure 5.5 Overall viscosity data for different polymer concentrations from Anton-Paar rheometer analysis, including comparisons with the Carreau-Yasuda model (Yasuda et al., 1981).

According to Del Giudice et al. (2017), relaxation time, λ, is an observable time scale, which is an important characteristic of polymer solutions. Relaxation time is related to the elastic energy absorbed by the polymer solution, depending on the relaxation process within and outside the polymer chain. Relaxation time is associated with large scale microscopic motions, which are generally associated with the elastic character of the polymer solutions (Sunthar, 2010). Relaxation time depends on the relaxation process within and outside the polymer chain. The relaxation process occurs from multiple processes related to the entire polymer chain, including the polymer sub-chains (Del

Guidice et al., 2017). When the equilibrium state of a polymer microstructure is deformed, the chain tends to back to the equilibrium state through the elastic energy stored during the deformation process. As polymer solutions are not ideal elastic material, dissipative processes also occur at the same time. For relatively small deformations, system response are often considered linear. Linear viscoelastic behavior allows determination of the relaxation time using frequency sweep rheometer methods, however, the determination of the relaxation time by measurement is generally challenging for dilute polymer solutions.

Within the present investigation, polymer relaxation time, λ, is determine using the Zimm model (De Gennes, 1974; Del Guidice et al., 2017; Zim, 1956). This theoretical approach describes the relaxation time analytically for smaller polymer concentrations below the concentration that polymer coils start to interact with each other. Included within this theoretical model is dependence upon intrinsic viscosity, polymer molecular weight, universal gas constant, absolute temperature, and a dimensionless scaling exponent. The intrinsic viscosity is determined based upon theoretical models from Del Giudice et al. (2017). The zero shear rate viscosity, which is required for this calculation, is determined using the Carreau-Yasuda viscosity model (Yasuda et al., 1981). Within such dilute polymer solutions, with no elastic instability present, polymer coils are believed to have sufficient space without contacting and interacting with each other. The resulting viscoelasticity then depends upon the behavior of individual polymer coils. With no significant interactions between polymer chains, the viscosity is then approximately constant for dilute polymer solutions, even when the chains attain maximum length (Sunthar, 2010; Rao and Tattiyakul, 1999) behavior which is consistent with characteristics associated with Boger fluids (James, 2009).

5.4. Transition Onset of Elastic Instabilities

Figure 5.5 shows that the transition conditions associated with the McKinley et al. model (McKinley et al., 1996) with viscosity values determined using experimental rheometer data. Here, McKinley et al. model values deviate from the present onset conditions by greater amounts, as shear rate magnitudes increase beyond 18 sec^{-1}. An improved and more accurate match to the present elastic instability onset conditions, over the complete range of tested shear rates, is provided by

$$Wi=30$$

This constant Weissenberg number criterion is then consistent with elastic instability phenomenological models described by De Gennes (1974) and Pan et al. (2013). Note that this value of onset Wi depends upon determination of $\dot{\gamma}$ for the present RCF environment. A different determination of $\dot{\gamma}$ (for example, based upon local velocity gradient, instead of overall velosity gradient) of course provides a different value of onset Wissenberg number. Determination of the constant Weissenberg number criterion, given by the above equation, is based upon measurements at different expeirmental conditions, as polymer concentration, shear rate, and rotational speed are varied.

5.5. Nusselt Number and Flow Static Temperature Variations

Figure 5.6 shows Nusselt number variations with shear rate and disk rotational speed for different polymer concentrations. Part a results within this figure are presented for the $1/3R_1$ location, and part b results within this figure are presented for the $2/3R_1$ location. As such, associated data are given for two different circumferential test surface segments shown in Figure 4.4: the $1/3R_1$ location data are associated with flow thermocouple 3 and surface thermocouple 5, whereas the $2/3R_1$ location data are associated

with flow thermocouple 2 and surface thermocouple 6. Because larger flow strain rates are present at larger radial locations, Nusselt numbers in Figure 5.6b are generally higher than values in Figure 5.6a, when compared at the same polymer concentration ρ and rotational speed ω. Consequently, all subsequent discussions consider Nusselt number data associated with the $2/3R_1$ circumferential test surface segment. Associated Nusselt numbers within Figure 5.6b then generally increase with polymer concentration, when compared at particular values of shear rate and disk rotational speed. With the exception of data presented for shear rates less than about 12 sec^{-1}, associated Nusselt number data then also generally increase with shear rate and disk rotational speed, for each polymer concentration. The largest increases are associated with higher concentrations of polymers, and the lowest are associated with the sucrose solvent flows. Resulting Nusselt numbers are then as high as 3.0, compared to zero shear rate values (obtained with zero rotation), which are in the vicinity of 1.0.

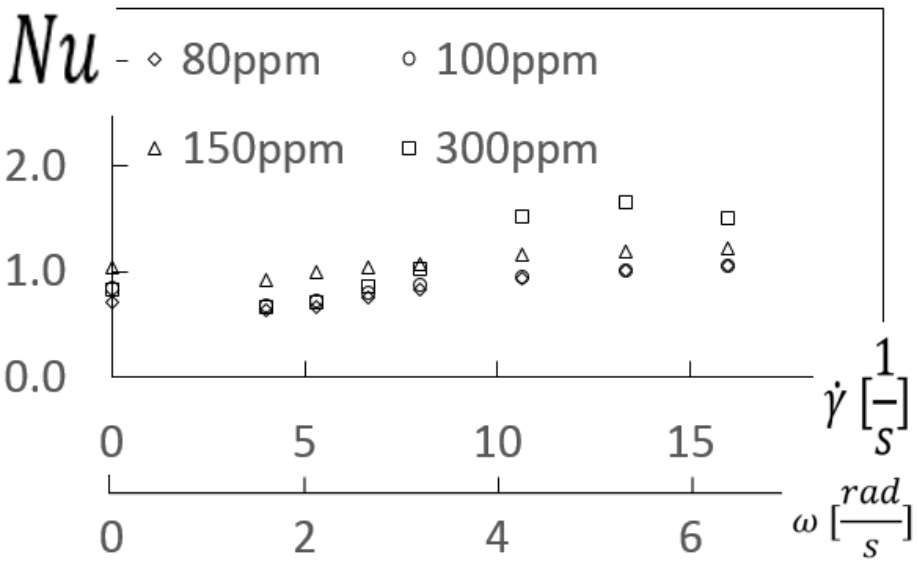

(a)

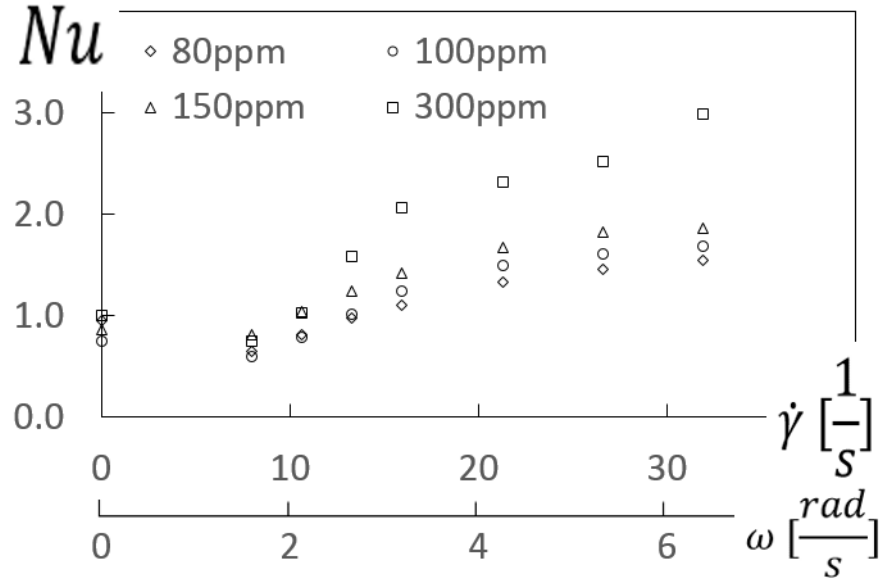

(b)

Figure 5.6. Nusselt number variations with shear rate and disk rotational speed for different polymer concentrations, for the (a) $1/3R_1$ and (b) $2/3R_1$ locations.

With no elastic instabilities present, the data in Figure 5.6b show that Nusselt numbers for shear rates less than approximately 12 sec^{-1} are about the same as, or slightly lower than, values associated with zero shear rate. Here, Nusselt number variations with shear rate are about the same, regardless of the value of polymer concentration. Note that the zero shear rate condition is produced with the disk stationary, without rotation. Resulting zero-shear-rate Nusselt number variations are then a result only of diffusion-related phenomena. When shear rates then become greater than 0 sec^{-1} because of disk rotation (but continue to be less than 12 sec^{-1}), Nusselt numbers are then a result of both advection and diffusion-related effects. Because these particular flows involve viscoelastic, Boger fluids, intricate interactions between polymers and surrounding, adjacent flows are also believed to also have some influence on local thermal transport.

When shear rates then become higher than 12 sec^{-1}, Figure 5.6b shows that Nusselt number values begin to increase as shear rate increases. Note that Nusselt number dependence upon shear rate changes as polymer concentration varies.

These same data are also presented in Figure 5.7 as Nu/Nu_s Nusselt number ratios, such that Nusselt numbers are normalized by sucrose solvent values associated with ρ=0 ppm. Associated ratio variations for the $2/3R_1$ location are then shown as they vary with polymer concentration for different flow shear rate magnitudes. Here, Nusselt number ratios are approximately equal to 1.0, regardless of polymer concentration, whenever shear rates are lower than 12 sec^{-1}. Nusselt number ratios then increase substantially as polymer concentration increases, for higher shear rate values which are greater than 12 sec^{-1}.

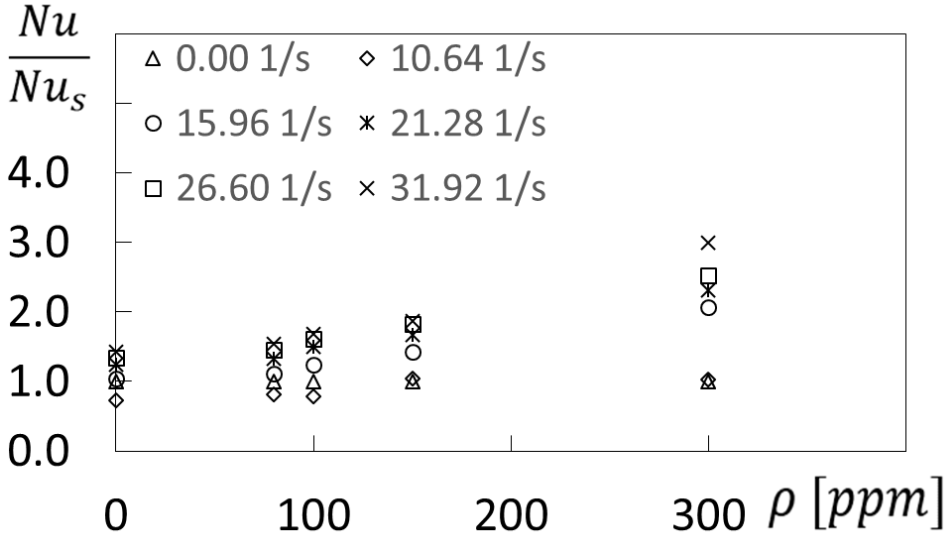

Figure 5.7 Nusselt number ratio variations with polymer concentration for the $2/3R_1$ location, for different flow shear rates.

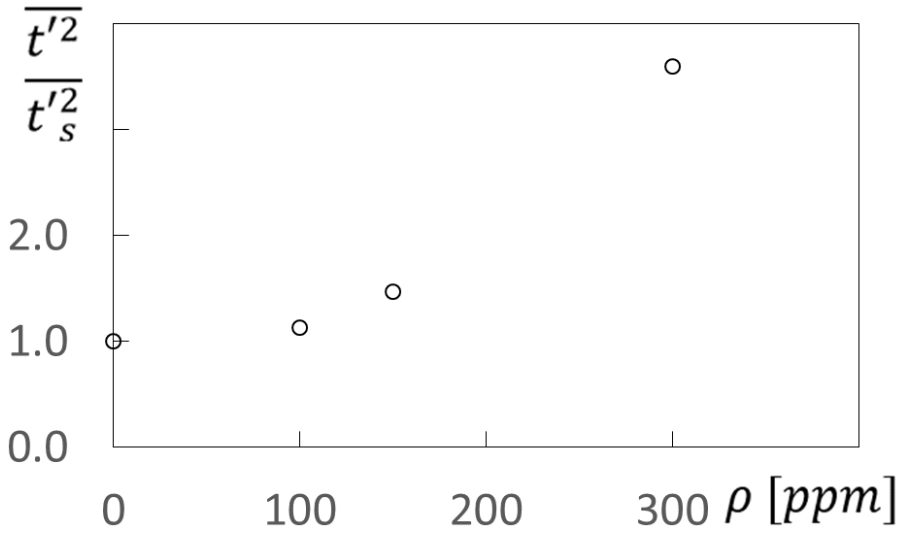

Figure 5.8 Normalized and time-averaged magnitudes of the mean-square of flow static temperature fluctuations as they vary with polymer concentration, for a 4.19 rad/s disk rotational speed and a shear rate of 21.28 1/s for the $2/3R_1$ location.

Time-averaged magnitudes of the mean-square of flow static temperature fluctuations are presented in Figure 5.8, as they vary with polymer concentration. These data are provided for $\dot{\gamma}$=21.28 sec^{-1} for the $2/3R_1$ location. Within this figure, magnitudes

are normalized by sucrose solvent values. Because the shear rate associated with these data is higher than the observed instability onset value (which is about 12 sec^{-1}), normalized $\overline{t'^2}$ magnitudes increase substantially with polymer concentration, as ρ values because greater than 100 ppm.

Power spectral distributions of static temperature fluctuations are presented in Figures 5.9a and 5.9b, again for the $2/3R_1$ flow location, including data which are associated with the four normalized $\overline{t'^2}$ data points, which are shown in Figure 5.8. Figure 5.9b compares data for a 4.19 1/s disk rotational speed and $\dot{\gamma}$=21.28 sec^{-1} for different polymer concentrations, whereas Figure 5.8b shows 300 ppm polymer concentration data for different shear rates and different disk rotational speeds.

Within Figure 5.9a, data for ρ=300 ppm, and within Figure 5.9b, data for ω of 3.14 rad/s and 4.19 rad/s show broad-band characteristics, with continuous power content present at frequencies from just greater than 0.01 Hz to values of approximately 1 Hz. The cascade power variation with frequency illustrates behavior which is similar to many turbulent flows. Such broad-band frequency behavior evidences the presence of chaotic local polymer motions, including aggressive, local flow fluctuations. Such behavior is consistent with observations of elastic instabilities in other investigations, with secondary flows generated above an instability threshold and turbulent-like flow features, including irregular fluid motions over a broad range of temporal and spatial scales (Pathak et al., 2004; Arratia et al., 2006; Pan et al., 2013). Associated spectral distributions are then substantially higher than distributions which are associated either with the sucrose solvent flow, where ρ=0 ppm, or when no rotation is present and ω=0 rad/s. Power spectral magitudes for these latter situations are of the order of background instrumenation noise.

As a result, the higher spectral power levels shown in Figs. 14a and 14b are as much as three orders of magnitude higher than the ρ=0 ppm and ω=0 rad/s arrangements, when compared at specific frequencies.

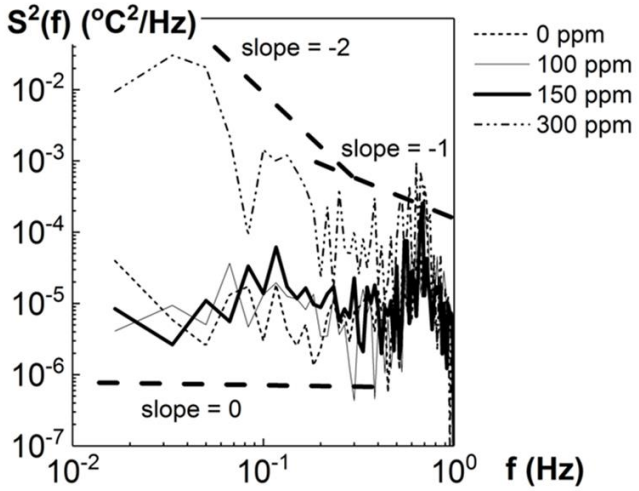

(a)

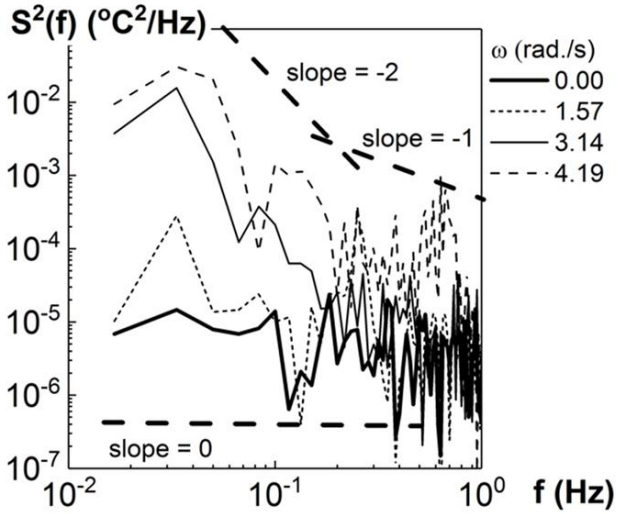

(b)

Figure 5.9 Spectra of flow static temperature fluctuations at the $2/3R_1$ location. (a) Comparison of 4.19 rad/s disk rotational speed and shear rate of 21.28 1/s for different polymer concentrations. (b) Comparison of 300 ppm polymer concentration data for different shear rates and different disk rotational speeds.

Flow temperature fluctuation data are also presented and discussed by Li et al. (2017). With elastic instabilities present, their temperature power spectral data also show broad-band behavior, with portions which are well represented with a -1.1 power law dependence upon frequency. Portions of the present data in Figures 5.9a and 5.9b show power law dependince (indicated by slope values) either of approximately -2 for the lower frequencies, or -1 for the higher frequencies. Note that each magnitude of dimensional $\overline{t'^2}$, determined from the integral of each power spectral distribution, is in agreement with mean-square magnitudes of static temperature fluctuations, determined directly from time-series data. In addiiton, many of the spectra within Figures 5.8a and 5.8b show a broad local peak near 0.67 Hz, which corresponds to the rotation frequancy of the disk.

5.6. Nusselt Number Variations with Reynolds Number, Graetz number, Weissenberg number, and McKinley transition Parameter

Figure 5.10 shows Nusselt number ratio variations with Reynolds number for the $2/3R_1$ location, for different polymer concentrations. Here, Reynolds number is determined using the equation given by $Re = \rho_d H\omega R/2\eta$, where $R = (2/3)R_1$. From this definition, it is evident that fluid shear rate is directly proportional to Reynolds number. Within Figure 5.10, Nusselt number ratios are again presented, which are determined by normalization with sucrose solvent values associated with ρ=0 ppm. Closed symbols within Figure 5.10 indicate Nusselt number ratios associated with experimental conditions which correspond with the onset of elastic instabilities. For each polymer concentration, each closed symbol ratio is determined for the shear rate (and other experimental conditions) associated with transition, as discerned from flow visualization images.

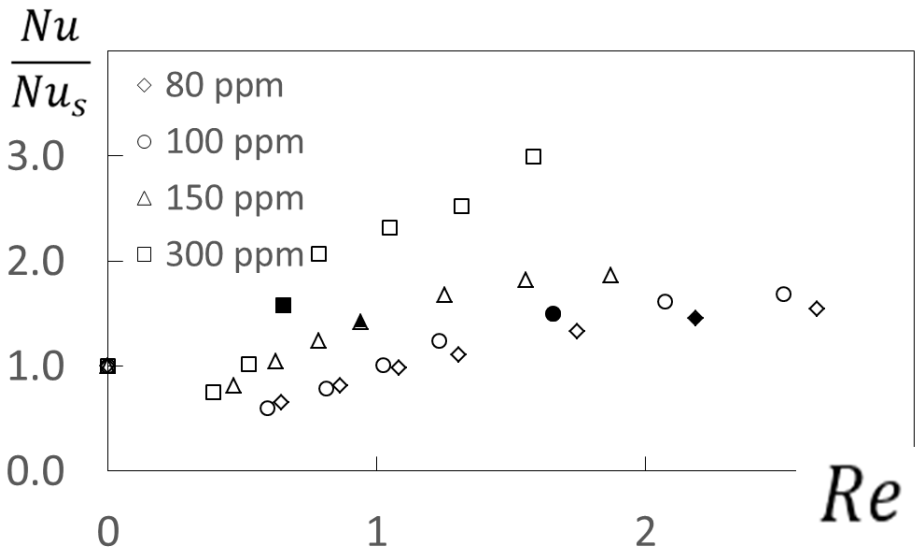

Figure 5.10 Nusselt number ratio variations with Reynolds number for the $2/3R_1$ location, for different polymer concentrations. Closed symbols indicate transition experimental conditions for onset of elastic instabilities.

Considering data in Figure 5.10 *for a particular value of polymer concentration*, it is evident that ratios decrease slightly, relative to $Nu/Nu_s=1$ at Re=0, as Re becomes just greater than 0. As Reynolds number increases further, ratios then increase continually, to eventually become equal to, and then, greater than closed-symbol transition values. Increasing Reynolds numbers are then associated with increasing fluid shear rates, and increasing polymer concentrations are associated with larger polymer relation times. For a particular polymer concentration, Nusselt number ratios less than the closed symbol, transition value, then correspond with viscoelastic, Boger fluid flows, whereas ratios greater are believed to correspond with flows with elastic instabilties. From Figure 5.10, it is evident that onset and development of elastic instability transition occurs at significantly different Reynolds number values as polymer concentration varies.

Figure 5.11 then shows that transition onset also occurs at significantly different Graetz number values as polymer concentration varies. Within this figure, Nusselt number

ratios are again presented for different polymer concentrations, but provided as they vary with Graetz number, which is employed because of the pronounced streamline curvature which is present within the RCF device. Graetz number is defined using $Gz = Re\,\mathrm{Pr}(H/\pi R_1)$ to characterize internal flow within curved ducts. Larger Graetz numbers are then associated with more significant effects of streamline curvature on flow structural characteristics.

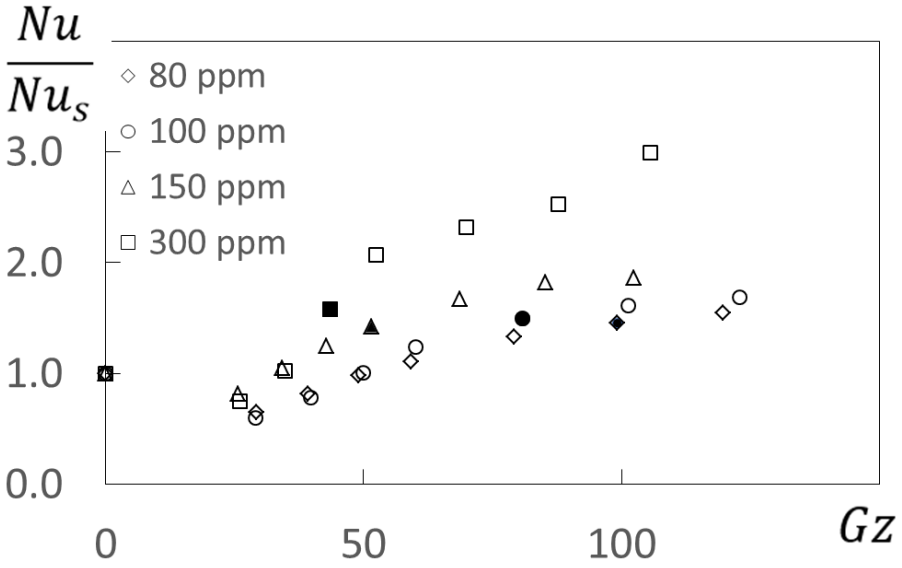

Figure 5.11. Nusselt number ratio variations with Graetz number for the $2/3R_1$ location, for different polymer concentrations. Closed symbols indicate transition experimental conditions for onset of elastic instabilities.

Nusselt number ratios for the $2/3R_1$ location and different polymer concentrations from Figures 5.10 and 5.11, are again presented in Figure 5.12, but as a function of Weissenberg number. From these data, it is evident that elastic instability transition onset is well represented by the Wi=30 experimental condition. Associated transition onset Nusselt number ratios equal 1.42 to 1.58. Variations of normalized and time-averaged magnitudes of the mean-square of flow static temperature fluctuations at the $2/3R_1$ location, within Figure 5.13, are then also consistent with this criterion, since those values also increase substantially as Weissenberg number becomes greater than 30.

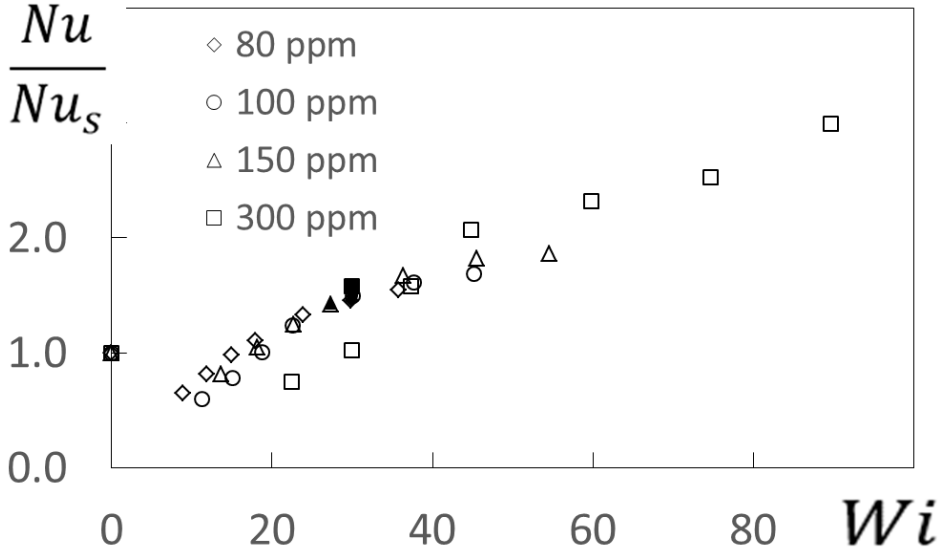

Figure 5.12 Nusselt number ratio variations with Weissenberg number for the $2/3R_1$ location, for different polymer concentrations. Closed symbols indicate transition experimental conditions for onset of elastic instabilities.

Figure 5.14 then shows that the present Nusselt number ratio data, as they vary with Weissenberg number, are also reasonably consistent with Nusselt number ratio results from Abed et al. (2016). Similar trends are evident for both collections of data, with substantial Nusselt number ratio increases as Weissenberg number varies from zero, to values as high as 70 to 90. Within Figure 5.15, Nusselt number ratio data for the $2/3R_1$ location from Figures 5.10, 5.11, 5.12, and 5.14, are again presented as they vary with the McKinley et al. elastic instability transition parameter (McKinley et al., 1996). From these results, the elastic instability onset, for different polymer concentrations, appears to occur over a significant range of McKinley et al. transition parameter values.

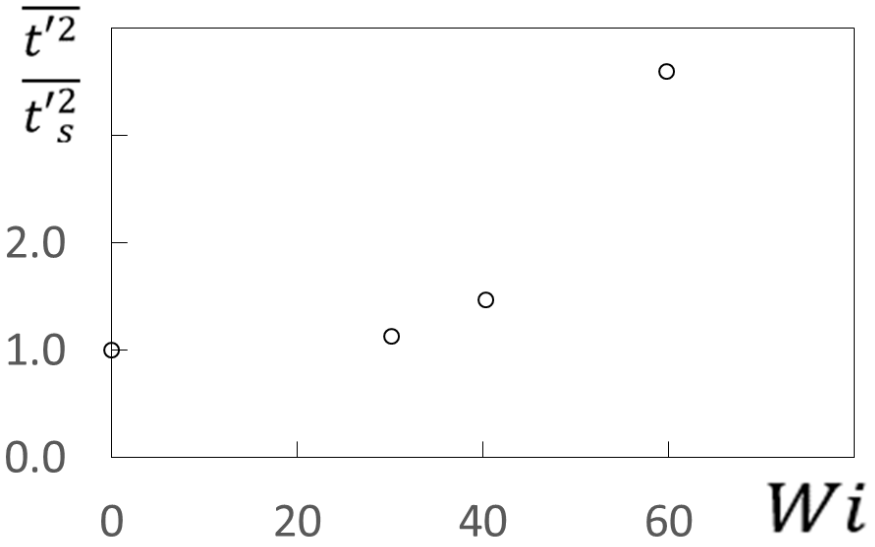

Figure 5.13 Normalized and time-averaged magnitudes of the mean-square of flow static temperature fluctuations with Weissenberg number for a 4.19 rad/s disk rotational speed and a shear rate of 21.28 1/s for the $2/3R_1$ location.

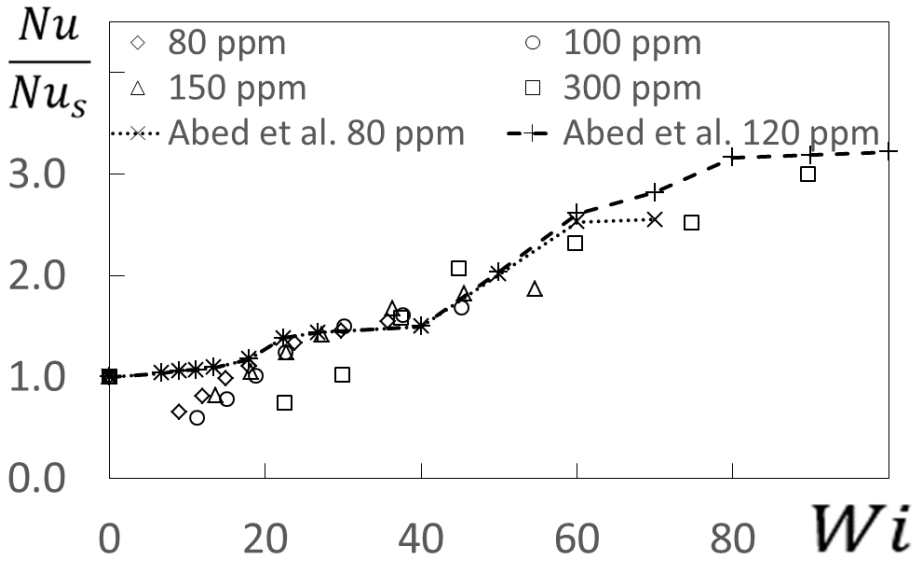

Figure 5.14 Nusselt number ratio variations with Weissenberg number for the $2/3R_1$ location, including comparisons with data from Abed et al. (2016).

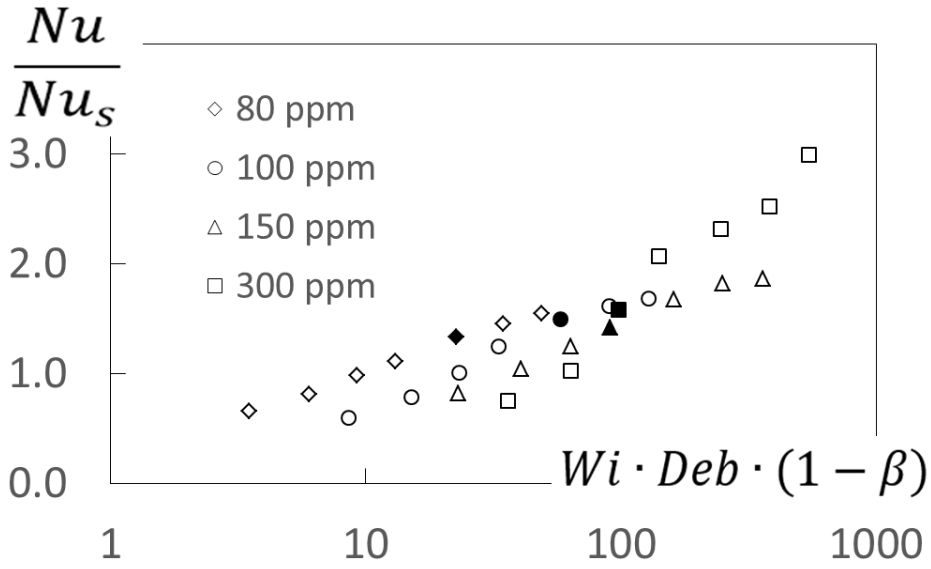

Figure 5.15. Nusselt number ratio variations for the $2/3R_1$ location as they vary with the McKinley et al. elastic instability transition parameter (McKinley et al., 1996). Closed symbols indicate transition experimental conditions for onset of elastic instabilites.

CHAPTER 6

EXPERIMENTAL RESULTS: ROTATIONAL COUETTE FLOW WITH DIFFERENT GAP HEIGHTS

The present chapter provides new data for a gap height of 7 mm, with comparisons between two different gap heights of 5mm and 7mm for a rotating Couette flow arrangement. A sucrose based Boger fluid with 3 different polymer concentrations, a pure sucrose solvent, and distilled water are used. To investigate thermal transport enhancement due to elastic turbulence, heat transfer coefficients, Nusselt numbers, fluctuating temperatures, temperature spectra, and flow visualizations are measured for different shear rates, two radius positions within the flow, and two gap heights. The flow visualizations are made for a gap height of 7 mm by tracking the flow with a fluorescein dye. By the variation of gap height, a wider range of shear rates is provided in which elastic instabilities and elastic turbulence are investigated.

6.1 Heat Transfer Results and Discussion

The present section gives experimental results, including Nusselt numbers, Nusselt number ratios, heat transfer coefficients, time-averaged magnitudes of static temperature fluctuations, and static temperature spectra. Associated experimental conditions are given in Tables 6.1 and 6.2. Measured results are obtained for polymer concentrations of 0 ppm,

100 ppm, 150 ppm, and 300 ppm. Investigated are gap heights of 5 mm and 7 mm at two radius positions of $1/3R_1$ and $2/3R_1$. Nusselt numbers are presented which are based upon different length scales. The fluid is subjected to various rotational speeds in the range of 0 RPM to 60 RPM, which correspond to shear rate magnitudes from 0 s^{-1} to 31.9 s^{-1}. Experimental results are presented as they vary with rotation speed and shear rate in order to show magnitudes of heat transfer enhancement with and without dependence on gap height.

Table 6.1 Test matrix for heat transfer measurements for gap heights of 5 mm and 7 mm.

Concentration [ppm]	Rotational speed [RPM]	Rotational speed ω [s^{-1}]	Shear rate $\dot{\gamma}$ [s^{-1}]			
			H=5 mm		H=7 mm	
			1/3 R	2/3 R	1/3 R	2/3 R
0	0	0.000	0.000	0.000	0.000	0.000
	15	1.571	3.990	7.980	2.850	5.700
	20	2.094	5.320	10.640	3.800	7.600
	25	2.618	6.650	13.299	4.750	9.500
	30	3.142	7.980	15.959	5.700	11.399
	40	4.189	10.640	21.279	7.600	15.199
	50	5.236	13.299	26.599	9.500	18.999
	60	6.283	15.959	31.919	11.399	22.799
100	0	0.000	0.000	0.000	0.000	0.000
	15	1.571	3.990	7.980	2.850	5.700
	20	2.094	5.320	10.640	3.800	7.600
	25	2.618	6.650	13.299	4.750	9.500
	30	3.142	7.980	15.959	5.700	11.399
	40	4.189	10.640	21.279	7.600	15.199
	50	5.236	13.299	26.599	9.500	18.999
	60	6.283	15.959	31.919	11.399	22.799
150	0	0.000	0.000	0.000	0.000	0.000
	15	1.571	3.990	7.980	2.850	5.700
	20	2.094	5.320	10.640	3.800	7.600
	25	2.618	6.650	13.299	4.750	9.500
	30	3.142	7.980	15.959	5.700	11.399
	40	4.189	10.640	21.279	7.600	15.199
	50	5.236	13.299	26.599	9.500	18.999
	60	6.283	15.959	31.919	11.399	22.799
300	0	0.000	0.000	0.000	0.000	0.000
	15	1.571	3.990	7.980	2.850	5.700
	20	2.094	5.320	10.640	3.800	7.600
	25	2.618	6.650	13.299	4.750	9.500
	30	3.142	7.980	15.959	5.700	11.399
	40	4.189	10.640	21.279	7.600	15.199
	50	5.236	13.299	26.599	9.500	18.999
	60	6.283	15.959	31.919	11.399	22.799

Table 6.2 Test matrix for flow visualizations for a gap height of 7 mm.

Concentration [ppm]	Rotational speed [RPM]	Rotational speed ω [s^{-1}]
0	0	0.000
	30	3.142
	60	6.283
150	0	0.000
	30	3.142
	60	6.283
300	0	0.000
	30	3.142
	60	6.283

Figure 6.1 shows Nusselt numbers based upon gap height as they vary with shear rate for two gap heights and different concentrations. Data are obtained at $2/3R_1$ radius position. For each shear rate value, the results indicate no clear trend with gap height because the Nusselt number is based upon gap height. For constant shear rate and gap height, Nusselt numbers generally increase with polymer concentration. For each gap height and each polymer concentration, Nusselt numbers generally become larger with shear rate. Figure 6.2 presents dimensional heat transfer coefficient variations with shear rate for the $2/3R_1$ radius position for gap heights of 5 mm and 7 mm and different concentrations. For each shear rate value and polymer concentration, heat transfer coefficients generally increase with smaller gap height. Heat transfer coefficients show an increasing trend with concentration for each gap height and each shear rate. Results exhibit a general heat transfer coefficient augmentation with shear rate when gap height and concentration are constant.

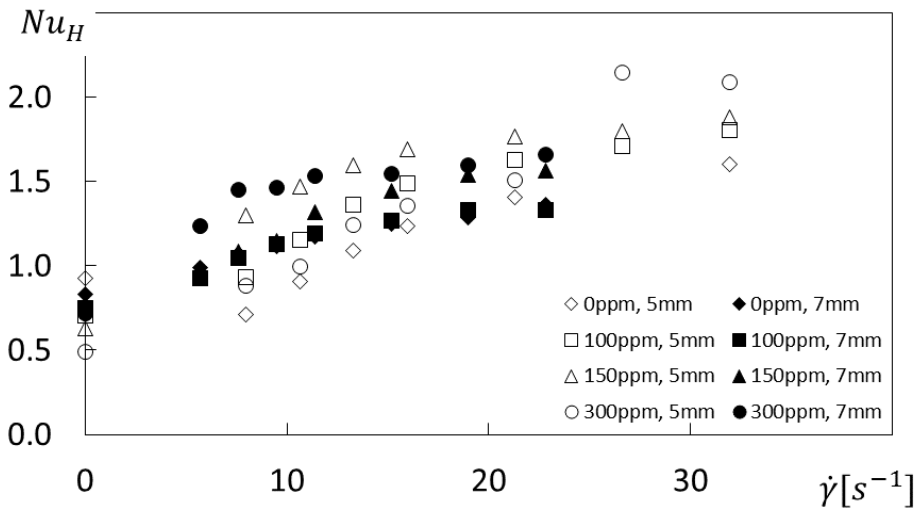

Figure 6.1 Nusselt number variations with shear rate, for gap heights of 5 mm and 7 mm at $2/3R_1$ radius position.

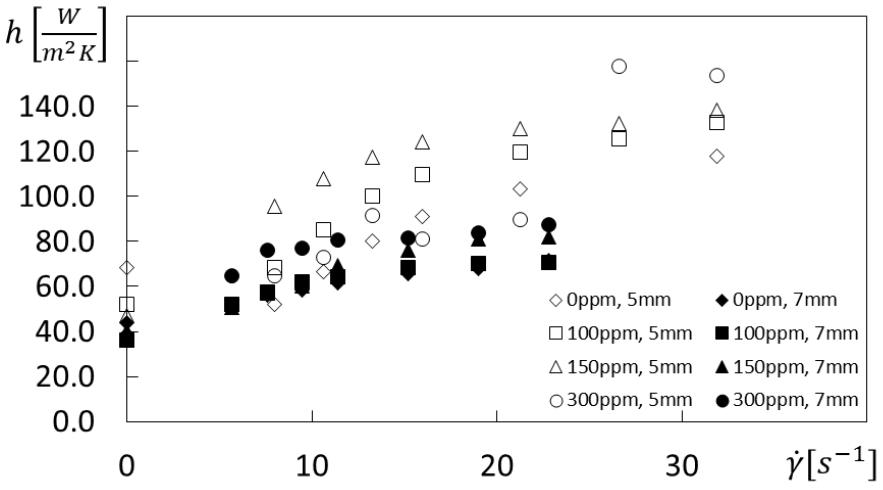

Figure 6.2 Heat transfer coefficient variations with shear rate, for gap heights of 5 mm and 7 mm at $2/3R_1$ radius position.

Figure 6.3 shows Nusselt number ratios based upon gap height as they vary with shear rate. These results are provided for two gap heights at the $2/3R_1$ radius location. Nusselt numbers are normalized by the Nusselt number at zero shear rate condition for each concentration. For each shear rate and each polymer concentration, Nusselt number ratios show no clear trend as gap height changes. For constant shear rate and gap height,

Nusselt number ratios generally increase with polymer concentration. Nusselt number ratios generally increase with shear rate for each concentration and each gap height.

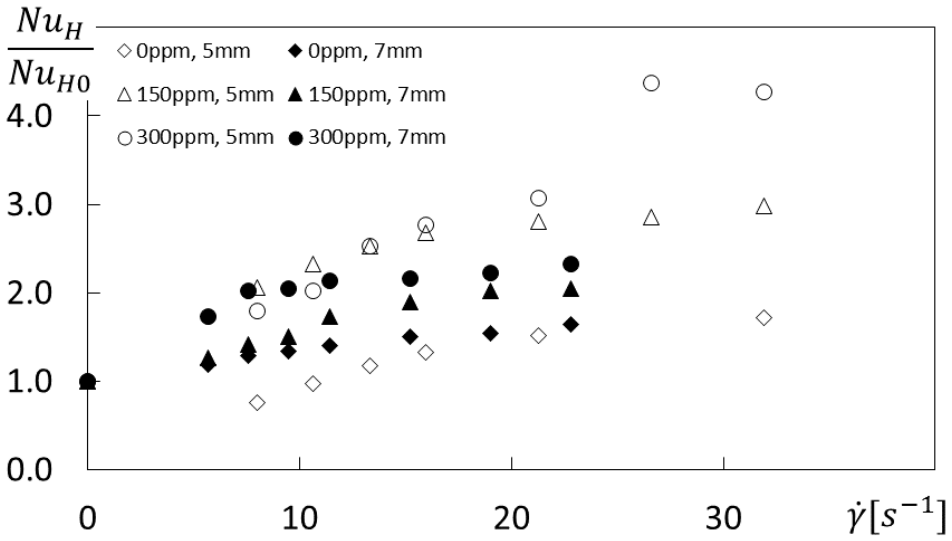

Figure 6.3 Nusselt number ratio variations with shear rate, for different polymer concentrations for gap heights of 5 mm and 7 mm at $2/3R_1$ radius position.

Figure 6.4 presents Nusselt number ratios based upon gap height as they vary with rotational speed. Nusselt number ratios are provided for two gap heights, two radius positions, and three polymer concentrations. In general, higher Nusselt number ratios are related to higher polymer concentrations for each rotational speed, radius position, and gap height. For a specific polymer concentration, rotational speed, and radius position, Nusselt number ratios generally increase with smaller gap height. For a specific concentration, radius position, and gap height, Nusselt number ratios increase with higher rotational speed. For a specific polymer concentration, rotational speed, and gap height, Nusselt number ratios increase with greater radius position. Increased Nusselt number ratios seem to result from shear rate augmentations which are associated with higher rotational speeds,

smaller gap heights, or greater radius positions. This is consistent with the assumption that shear rate is related to the onset and development of elastic instabilities.

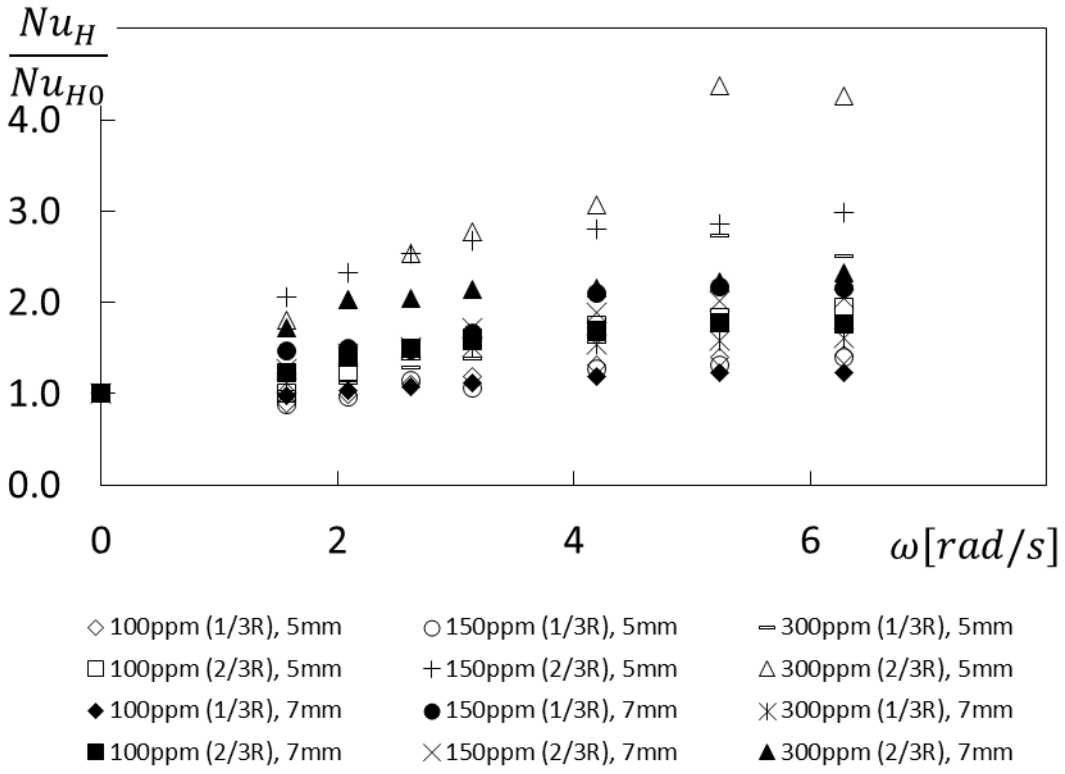

Figure 6.4 Nusselt number ratio variations with disc rotational speed for different polymer concentrations for $1/3R_1$ and $2/3R_1$ radius positions, and gap heights of 5 mm and 7 mm.

Figure 6.5(a) presents Nusselt number ratios as they vary with disc rotational speed for different polymer concentrations, gap height of 5 mm, and two radius positions of $1/3R_1$ and $2/3R_1$. Here, Nusselt numbers are based upon the rotation disk radius R as the characteristic length and are normalized by the Nusselt number value for each concentration and gap height for the zero shear rate condition. For each rotational speed and each polymer concentration, Nusselt number ratios generally show a significant augmentation with greater radius. Nusselt number ratios also show an increasing trend with concentration, when rotational speed and radius position remain the same. For each

concentration and each radius position, Nusselt number ratios generally become larger with rotational speed due to higher magnitudes of shear rate.

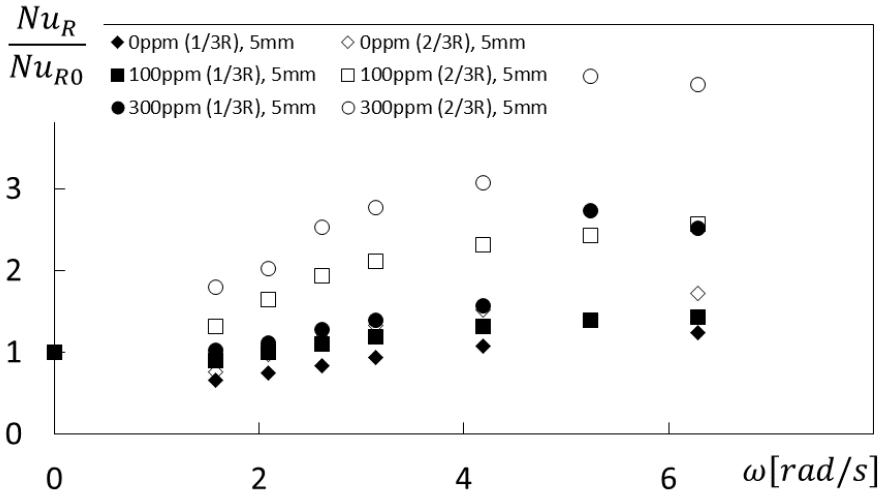

(a)

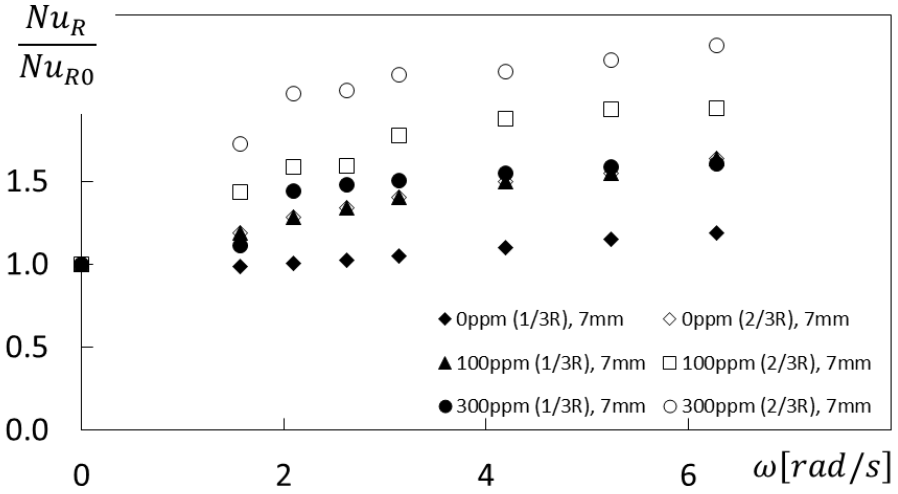

(b)

Figure 6.5 Nusselt number ratio variations with disc rotational speed for different polymer concentrations for $1/3R_1$ and $2/3R_1$ radius positions: (a) at a gap height of 5 mm; (b) at a gap height of 7 mm.

Figure 6.5(b) provides Nusselt numbers ratios as they vary with disc rotational speed for a gap height of 7 mm, different concentrations, and two radius positions. Here, the Nusselt number characteristic length is the rotational disk radius R_1. Nusselt number ratios show an overall augmentation with greater radius location for constant values of polymer concentration and rotational speed. Results indicate a general increase with rotational speed for each polymer concentration and each radius position. For each radius position and each rotational speed, Nusselt number ratios generally increase with polymer concentration. Both parts of Figure 6.5 show Nusselt number ratio augmentation increases with higher polymer concentrations (as radial location, disc rotational speed, and gap height are maintained constant), which are believed to be associated to the onset and development of elastic instabilities.

Figures 6.6(a) and 6.6(b) show Nusselt number ratios as they vary with disc rotational speed for two gap heights and three polymer concentrations. In general, for the $2/3R_1$ position (and with the exception of the 0 ppm polymer concentration), Nusselt number ratios in Figure 6.6(b) are generally higher as gap height changes from 7 mm to 5 mm, provided disc rotational speed, polymer concentration, and radial position are maintained constant. When the $1/3R_1$ position is examined, trends with changing gap height in Figure 6.6(a) are less consistent. This is believed to be due to overall lower shear rates, and less flow instability development, as radial position becomes smaller.

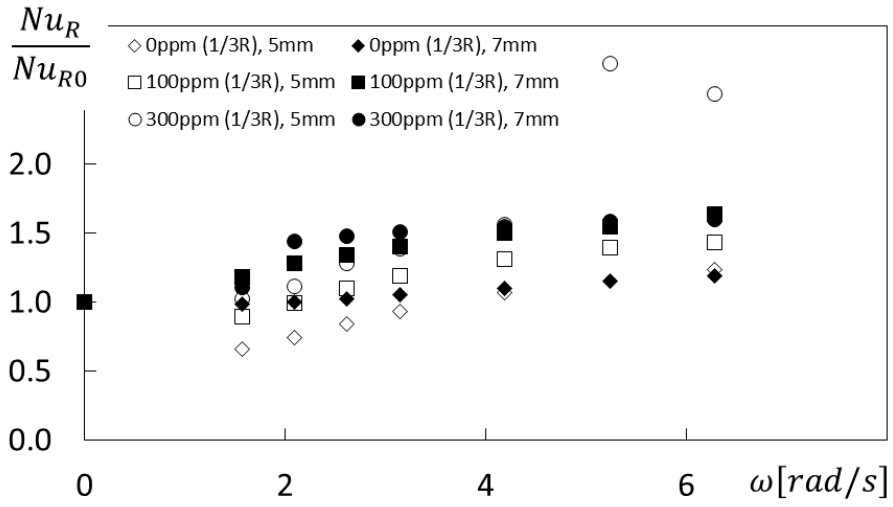

(a)

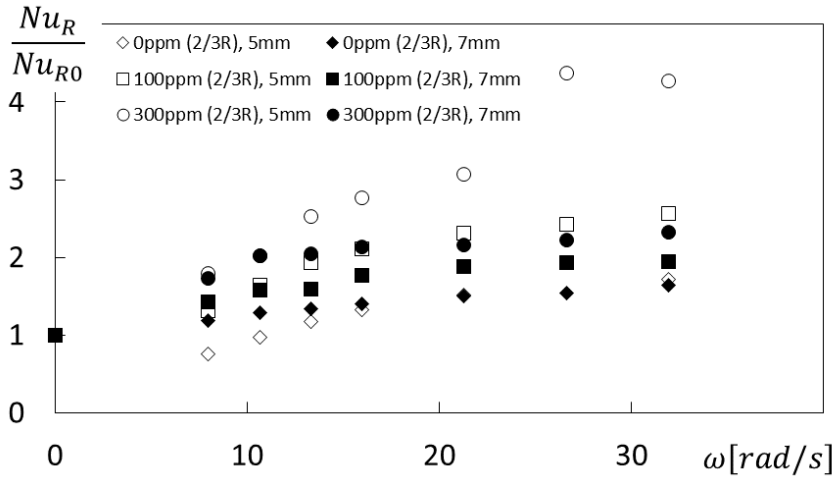

(b)

Figure 6.6 Nusselt number ratio variations with disc rotational speed for different polymer concentrations for gap heights of 5 mm and 7 mm: (a) at $1/3R_1$ radius position; (b) at $2/3R_1$ radius position.

Figure 6.7 gives the mean-square of static temperature fluctuations as they vary with shear rate for three different polymer concentrations, a gap height of 7 mm and the $2/3R_1$ radius position. For a particular polymer concentration, the mean-square of temperature fluctuations generally increase with shear rate. The results also show

significantly higher temperature fluctuation magnitudes as polymer concentration increases, compared to the 0 ppm sucrose solution. The two parts of Figure 6.8 show spectra of static temperature for different polymer concentrations, a gap height of 7mm, and the $2/3R_1$ radius position. Figure 6.8(a) gives the temperature spectra for a disc rotational speed of 40 RPM. Figure 6.8(b) shows the temperature spectra for a disc rotational speed of 60 RPM. Static temperature spectra show higher magnitudes of energy with increasing polymer concentration for each frequency. Such increases of spectral energy content at a particular frequency, as well as the increases of the mean-square of static temperature fluctuations, are believed to be due increase mixing and unsteady motions associated with the development and presence of elastic instabilities.

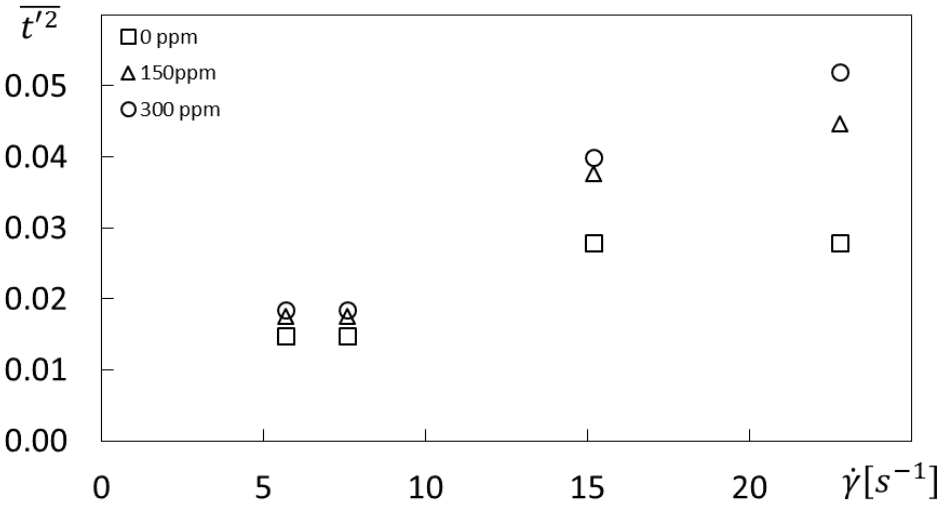

Figure 6.7 Mean square of static temperature fluctuation variation with local shear rate for different concentrations for a gap height of 7 mm and $2/3R_1$ radius position.

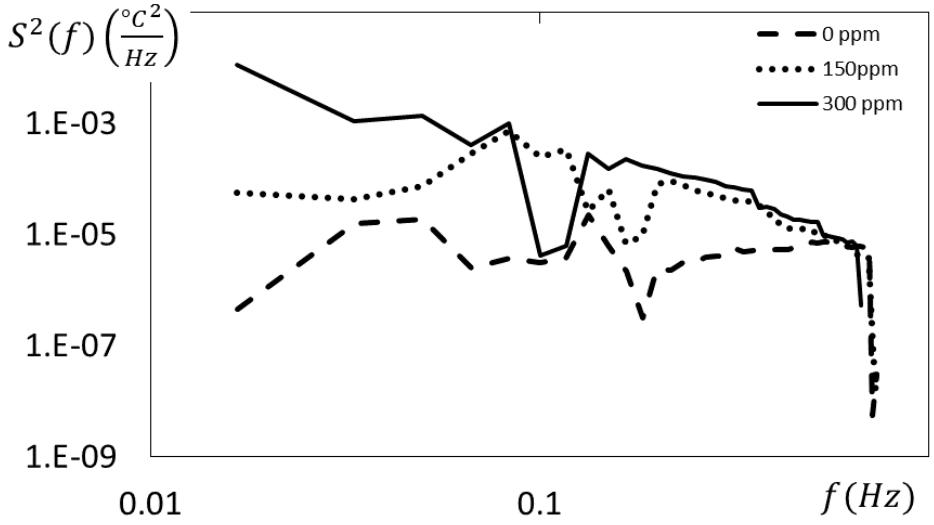

(a)

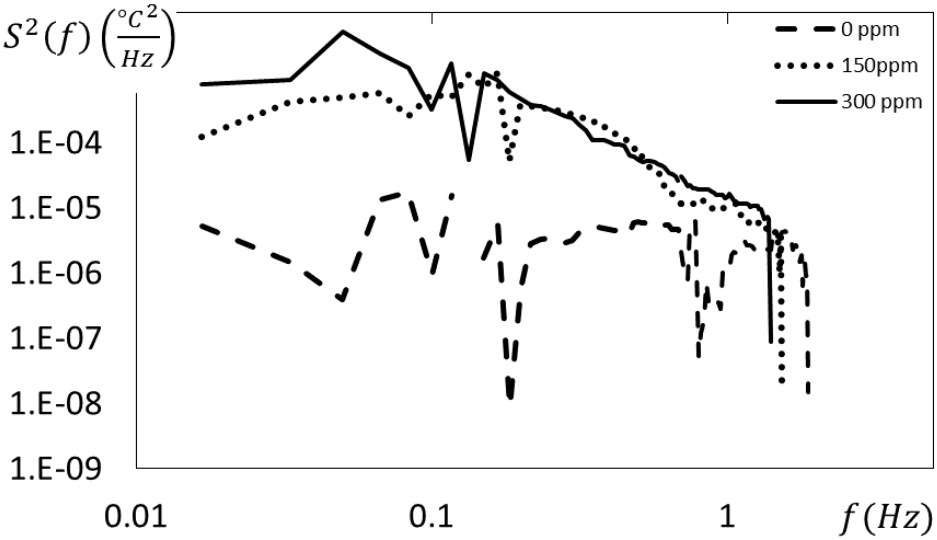

(b)

Figure 6.8 Static temperature spectra for different concentrations at gap height of 7 mm, and $2/3R_1$ radius location: (a) rotation speed of 40 RPM; (b) rotation speed of 60 RPM.

6.2 Flow Visualization Results and Discussion

The present section gives time sequences of flow visualization images, fluorescein dye front analysis results, and procedures for determination of effective diffusion coefficients, along with the effective diffusion coefficient values. As discussed in Chapter

4, flow variations are visualized using a fluorescein red tracer dye, which is injected into the flow. Experiments are conducted for the gap height of 7 mm, with no disk rotation, as well as with three different disk rotations speeds, and polymer concentrations of 0 ppm, 150 ppm, and 300 ppm. Associated experimental conditions are given in Table 6.2.

6.2.1 Experimental results without advection

This section presents flow visualization images and diffusion coefficients for 0 RPM rotational speed, with no rotation of the disk. Because no advection is present for this arrangement, results characterize molecular diffusion phenomena only. Figure 6.9 shows associated time sequences of flow visualization images, including a scale, which is used for the diffusion analysis. From these results, it is evident that the dye diffuses a little more rapidly for the 150 ppm polymer concentration, compared to the 0 ppm sucrose solvent.

Figure 6.10 gives the grey scale as it varies with normalized radius location for 150 ppm polymer concentration and different times. Figure 6.11 gives normalized dye concentration variations as they vary with normalized radius location for 150 ppm concentration and two times. Experimental data are presented as unfilled markers. The fitted concentration profile is shown as solid line and determined by the approach described by Lee et al. (2004). This method is denoted the PDE approach, and is based upon a solution to Fick's second law of diffusion using a cylindrical coordinate system with the diffusion coefficient as the variable. To obtain the theoretical results in Figure 6.11, the diffusion coefficient is varied until the normalized concentration profile is consistent with the associated experimental data. As such, the PDE approach is applied to determine diffusion coefficients for each concentration. Figure 6.12 presents resulting diffusion coefficients as they vary with polymer concentration determined using PDE approach (with no advection).

For the 0 RPM condition, diffusion coefficients remain approximately constant over the range of polymer concentrations considered.

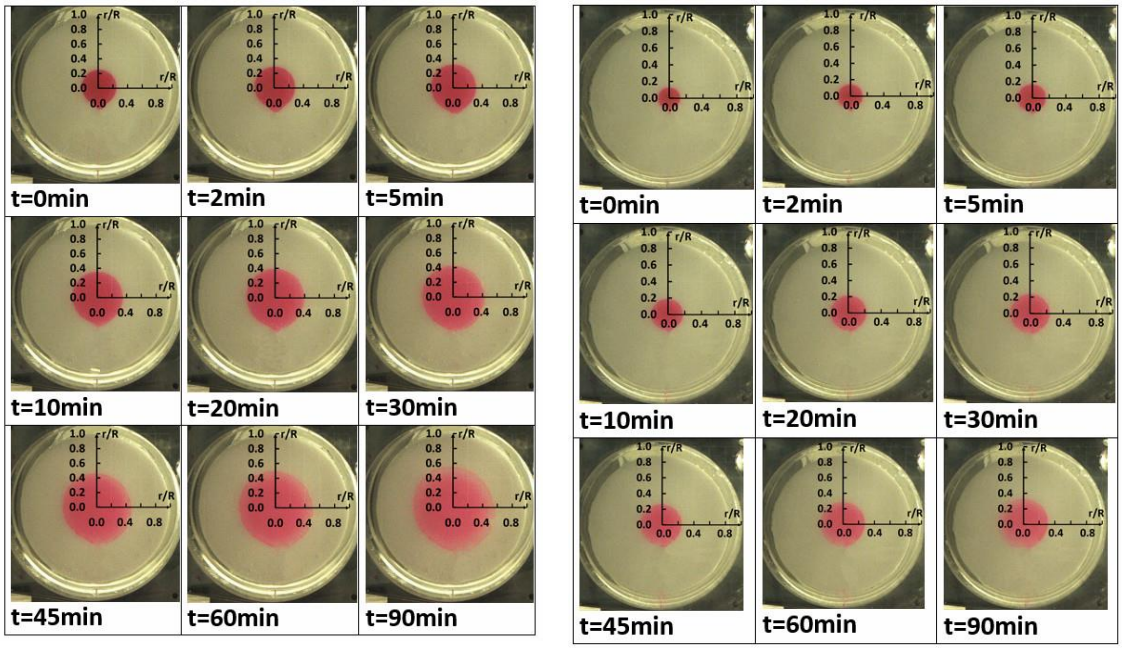

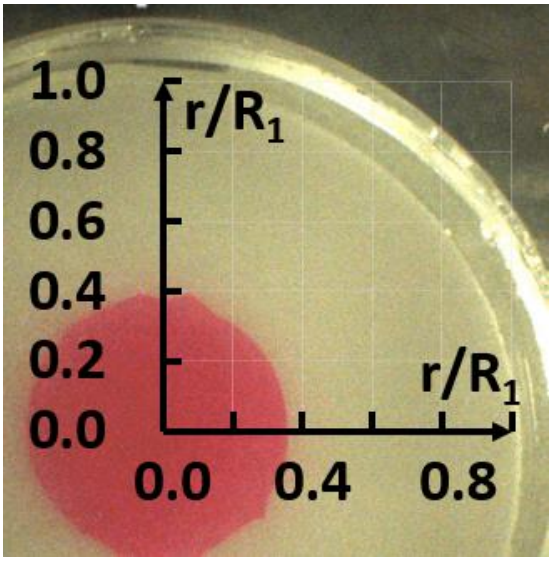

Figure 6.9 Time sequences of flow visualization images with no disk rotation, for polymer concentrations of 0 ppm and 150 ppm.

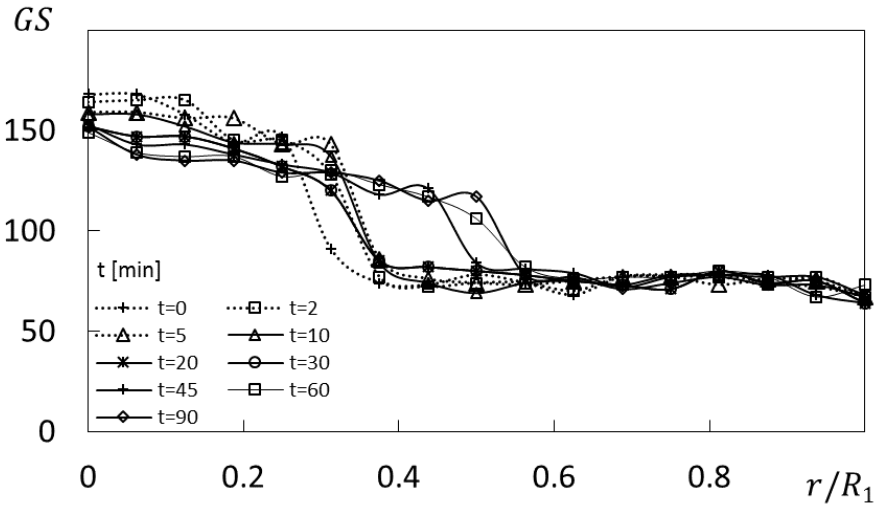

Figure 6.10 Gray scale variations with normalized radius location for 150 ppm polymer concentration, 0 RPM rotation speed, and no circumferential advection.

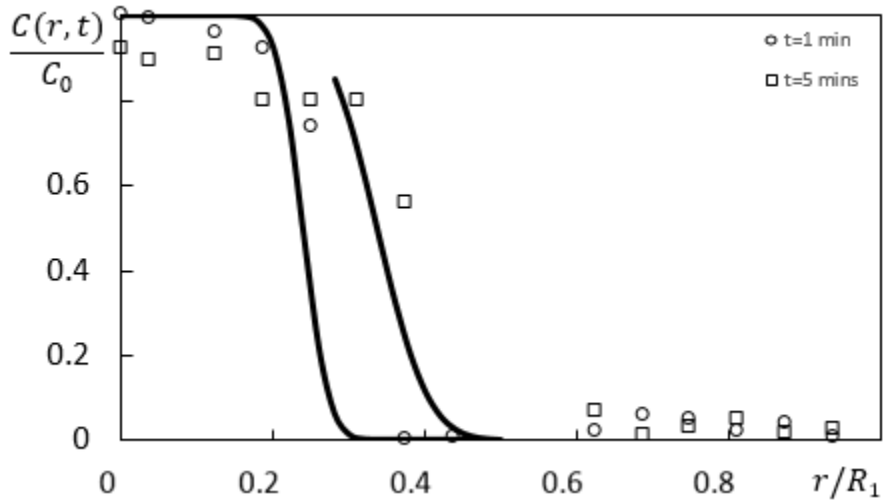

Figure 6.11 Comparison between experimental data and theoretical prediction from Lee et al. (2004) for 150 ppm polymer concentration, 0 RPM rotation speed, and no circumferential advection.

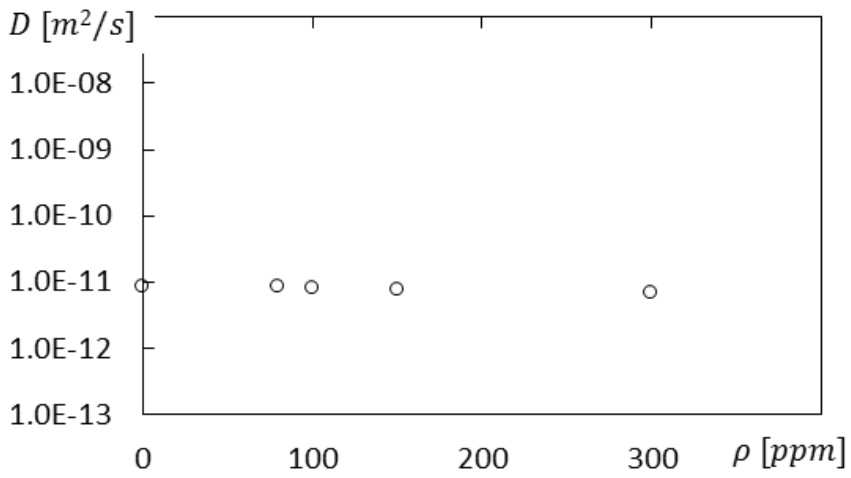

Figure 6.12 Diffusion coefficient variation with polymer concentration for 0 RPM rotation speed, and no circumferential advection.

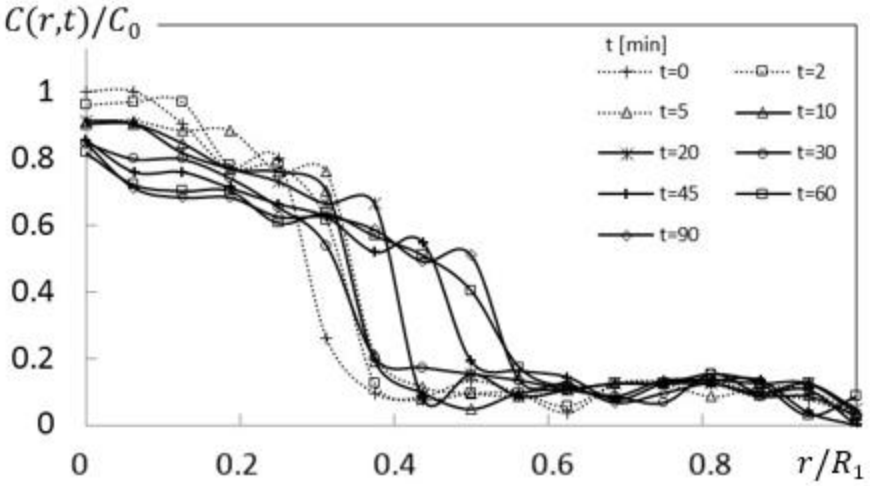

Figure 6.13 Normalized concentration profile variations with normalized radius location for 150 ppm polymer concentration, rotation speed of 0 RPM, and no circumferential advection.

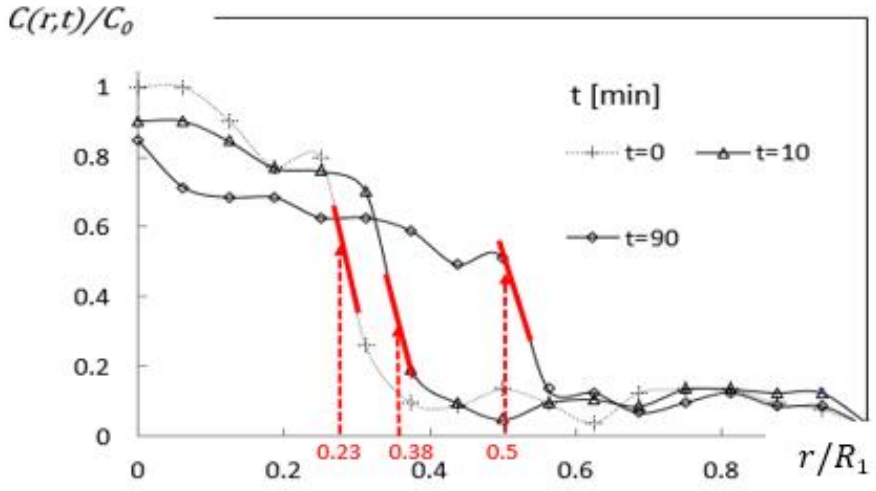

Figure 6.14 Normalized concentration profile variations with normalized radius location for 150 ppm polymer concentration, rotation speed of 0 RPM, and no circumferential advection.

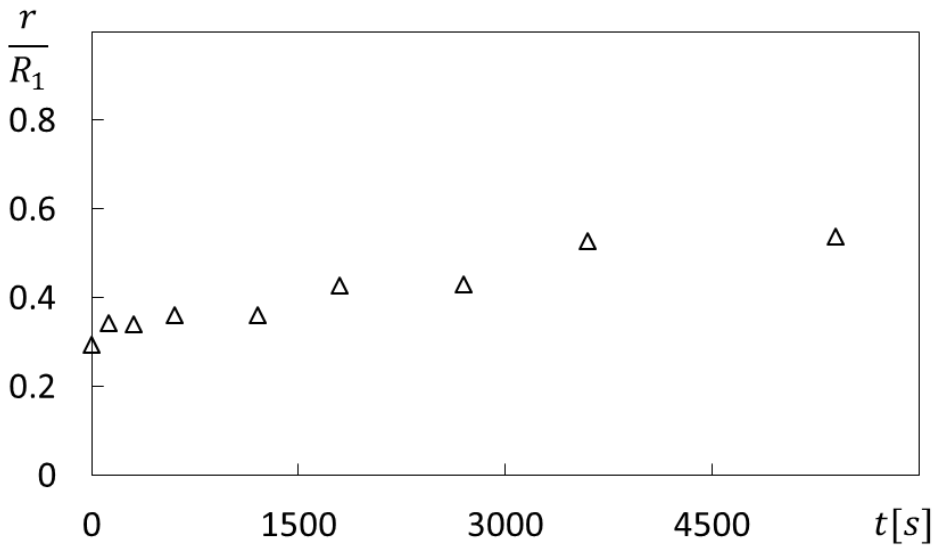

Figure 6.15 Dye front variation with time for 150 ppm polymer concentration, rotation speed of 0 RPM, and no circumferential advection.

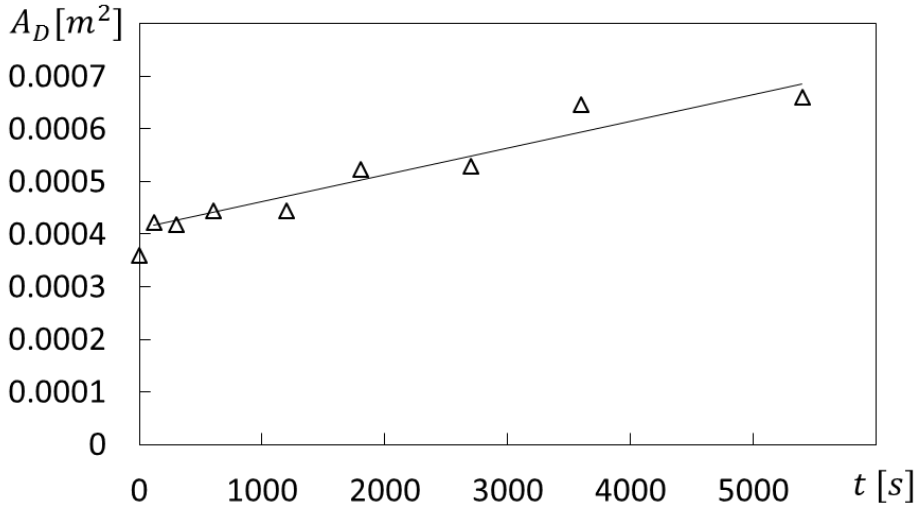

Figure 6.16 Dye front area variation with time for 150 ppm polymer concentration, rotation speed of 0 RPM, and no circumferential advection.

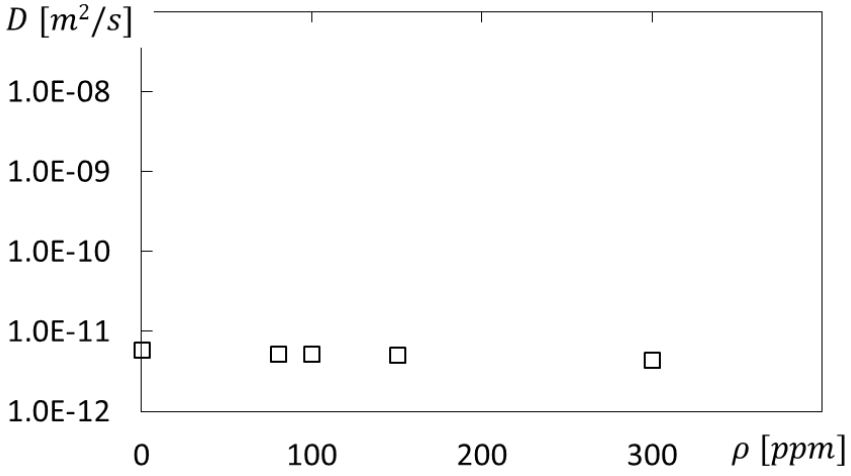

Figure 6.17 Diffusion coefficient variation with polymer concentration for rotation speed of 0 RPM, and no circumferential advection.

Figures 6.10 and 6.13 to 6.17 present steps for determination of diffusion coefficients using the time-derivative of the area of the fluorescein dye front, referred to as the area derivative approach. First, the normalized dye concentration is determined, as shown in Figure 6.13. Figure 6.14 then shows the normalized dye concentration as it varies with normalized radius location, including the maximum slope for three different times. The dye front is then considered to be located at the same radial position as the maximum

slope. This procedure is applied to normalized dye concentration data at each time. Figure 6.15 shows resulting dye front locations r/R as time proceeds. The dye front area A_D is determined using the equation given by

$$A_D = 2\pi rH \tag{6.1}$$

where H is the gap height and r the dye front radius. Figure 6.16 shows the dye front area A_D as it varies with time for 150 ppm and 0 RPM. A linear trend line is determined to fit the associated data points for the dye front area variation with time. The resulting diffusion coefficients are estimated from a linear fit to time-varying data, to provide representative values, and as such, are an approximate overall representation of each time-varying data set. The slope of the linear fit equals the diffusion coefficient multiplied by a constant, as given by

$$D = \beta \frac{dA_D}{dt} \tag{6.2}$$

where α is a dimensionless factor, $\beta = 0.001$ for $H = 5$ mm and $\beta = 0.0001$ for $H = 7$ mm. The factor β is determined to scale the diffusion coefficients obtained from the area derivative approach to diffusion coefficients as are calculated with the PDE approach. This factor is determined for the condition without advection, irrespective of polymer concentration. Figure 6.17 gives the resulting diffusion coefficients as they vary with polymer concentration. As such, the present approach is consistent with the comment by Einstein (1905) in relation to the diffusion coefficient D that "particles will pass across a unit area per unit time as the result of diffusion." According to Einstein (1905), using the microscopic theory, "the diffusion coefficient can be understood as parameterizing the area of a spherical surface, defined as the surface of root-mean-square displacement of material diffusing away from an infinitesimal point where a mass is initially concentrated. Since the

statistics of diffusion cause this area to grow linearly in time, the diffusion coefficient is a quantity described by area per time."

Figure 6.18 compares diffusion coefficients which are determined by four different methods, including Einstein (1905), Chenyakin et al. (2017), the PDE approach, and the area derivative approach. Chenyakin et al. (2017) investigates diffusion coefficients of three different dyes in sucrose solutions, including fluorescein dye. Diffusion coefficients for fluorescein dye as employed in the present study are determined from data provided by Chenyakin et al. (2017). The Einstein (1905) approach is given by

$$D = \frac{kT}{6\pi R_{HD}\eta} \tag{6.3}$$

where D is the diffusion coefficient, and k is the Boltzmann constant with value of 1.3807×10^{-23} J/K. The diffusing fluorescein dye is determined for temperature$T$, viscosity η, and with effective molecule hydrodynamic radius R_{HD} equal to $5.02\cdot\times10^{-10}$ m. Resulting diffusion coefficients are given in Table 6.3 and in Figure 6.18 (for each method) for different polymer concentrations. As shown in Figure 6.18, diffusion coefficients are approximately constant as polymer concentration varies. Note that the present analysis considers molecular diffusion of fluorescein only, with and without polymers present in the fluid.

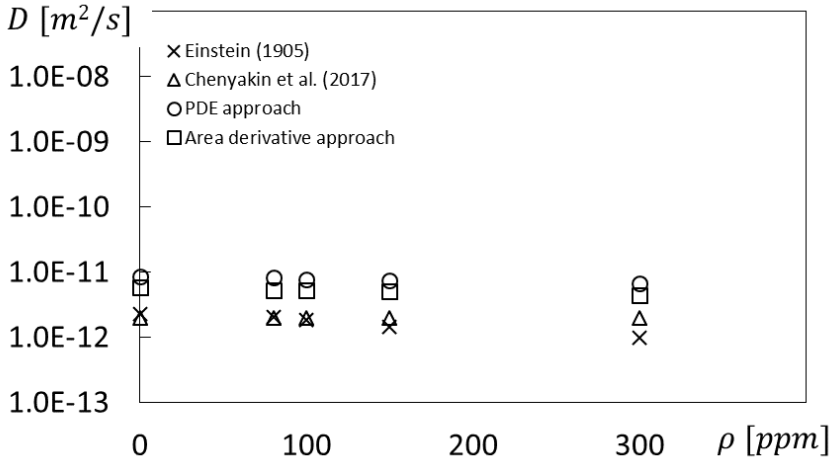

Figure 6.18 Diffusion coefficient variations with polymer concentration determined using different methods for rotation speed of 0 RPM, and no circumferential advection.

Table 6.3 Diffusion coefficients determined using different methods for rotation speed of 0 RPM, and no circumferential advection.

	D [10^{-12} m^2/s]			
ρ [ppm]	Einstein (1905)	Chenyakin et al. (2017)	PDE approach	Area derivative. approach
0	2.31	2.00	8.56	5.90
100	1.87	2.00	7.84	5.20
150	1.44	2.00	7.49	5.10
300	9.70	2.00	6.77	4.40

6.2.2 Experimental results with advection

In this subsection, results are given for testing conditions with *effective diffusion*, which accounts for circumferential advection, and in addition, in some cases, for the effects and presence of elastic instabilities and elastic turbulence. Investigated are rotation speeds of 15 RPM, 30 RPM, and 60 RPM using polymer concentrations of 0 ppm, 150 ppm and 300 ppm. Figures 6.19 to 6.21 show time sequences of flow visualization images for polymer concentrations of 0 ppm, 150 ppm, and 300 ppm, respectively. Each set of data is given for three different rotation speeds. For each rotation speed, dye generally diffuses (in an effective fashion) more rapidly as concentration increases. For each concentration, the

dye diffuses (in an effective fashion) more rapidly as rotation speed becomes higher, due to increased advection.

The same types of data and analysis approaches are employed in Figures 6.22 to 6.24 as for Figures 6.10 to 6.12, and in Figures 6.25 to 6.32 as for Figures 6.13 to 6.17. The difference is the effective diffusion data in Figures 6.22 to 6.24, and 6.25 to 6.32 are obtained with disk rotation and with circumferential advection.

Note that the effective diffusion coefficients D_{eff} with diffusion and advection are not true diffusion coefficients, but instead, are effective values that include effects and presence of elastic instabilities and elastic turbulence. Such an approach then allows a direct comparison to coefficients from diffusion alone. Effective diffusion coefficients D_{eff} are given in Figure 6.32 as they vary with rotation speed for three different polymer concentrations, as determined using area derivative approach. Results show effective diffusion coefficient augmentation as polymer concentration increases, for a particular value of rotation speed. Figure 6.33 then compares effective diffusion coefficients for the PDE approach and the area derivative approach. Effective diffusion coefficients are again shown as they vary with rotation speed for different polymer concentrations. For each polymer concentration and approach, effective diffusion coefficients increase with larger magnitudes of rotation speed. For each rotation speed, the effective diffusion coefficients generally increase with higher polymer concentration. For each rotation speed and polymer concentration, magnitudes of effective diffusion coefficients are generally higher for the area derivative approach, relative to the PDE approach.

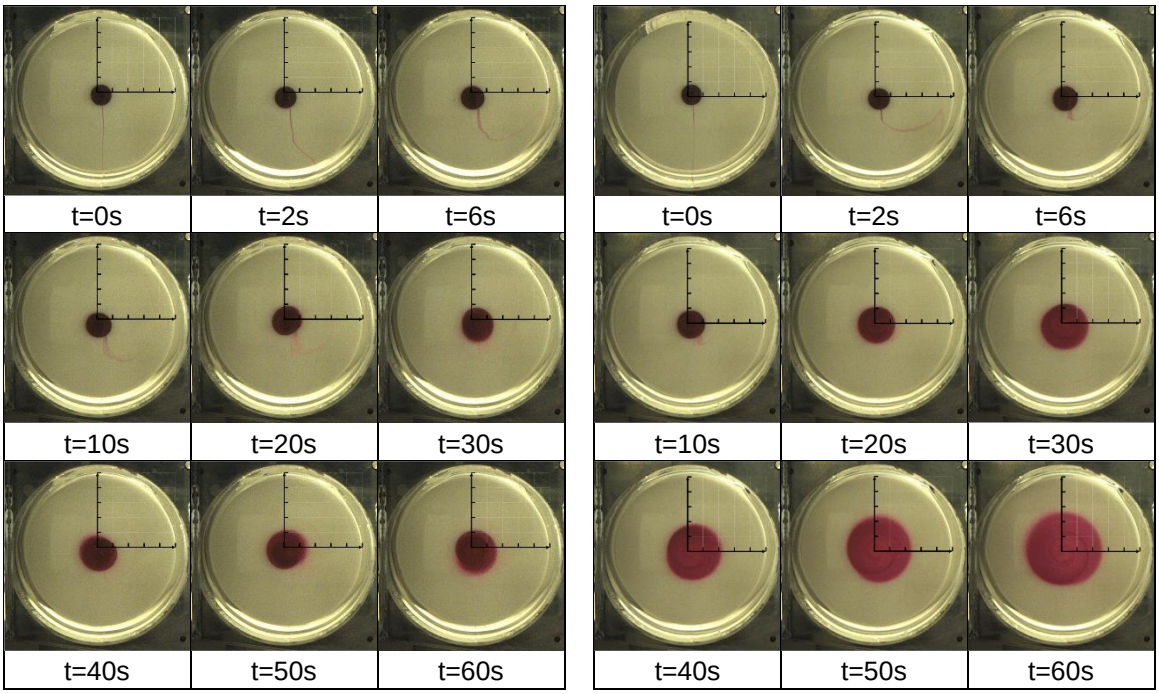

0 ppm, 15 RPM

0 ppm, 30 RPM

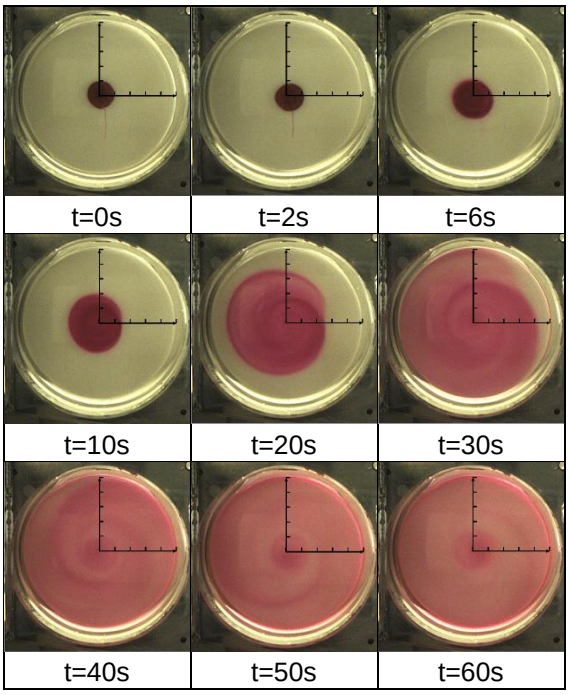

0 ppm, 60 RPM

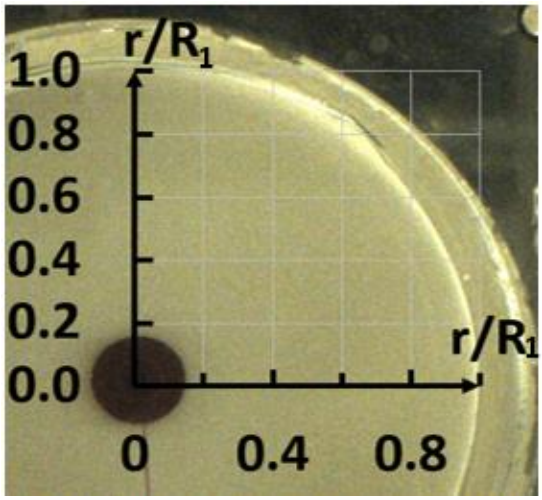

Figure 6.19 Time sequences of flow visualization images for 0 ppm polymer concentration for disk rotational speeds of 15 RPM, 30 RPM, and 60 RPM.

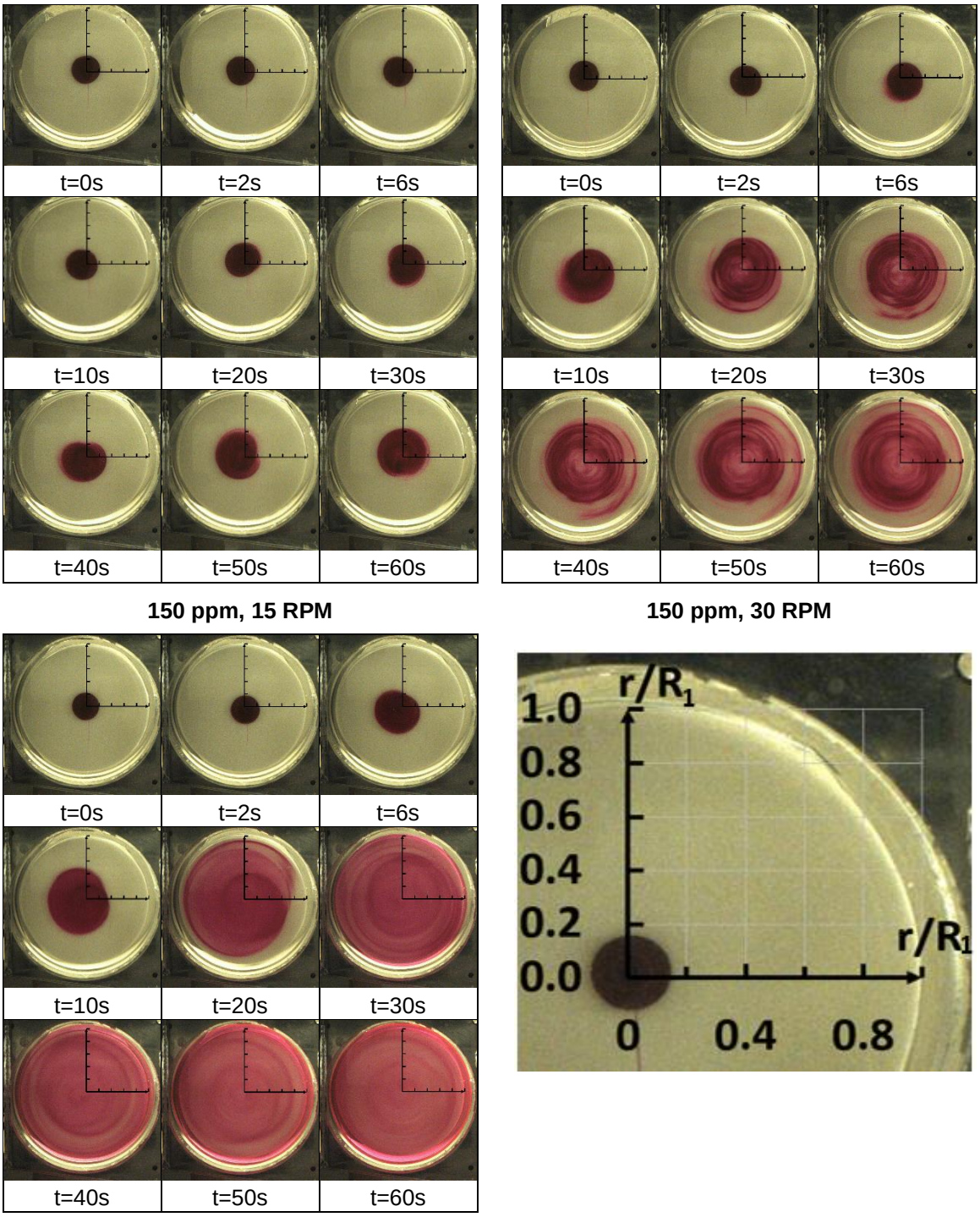

Figure 6.20 Time sequences of flow visualization images for 150 ppm polymer concentration for disk rotational speeds of 15 RPM, 30 RPM, and 60 RPM.

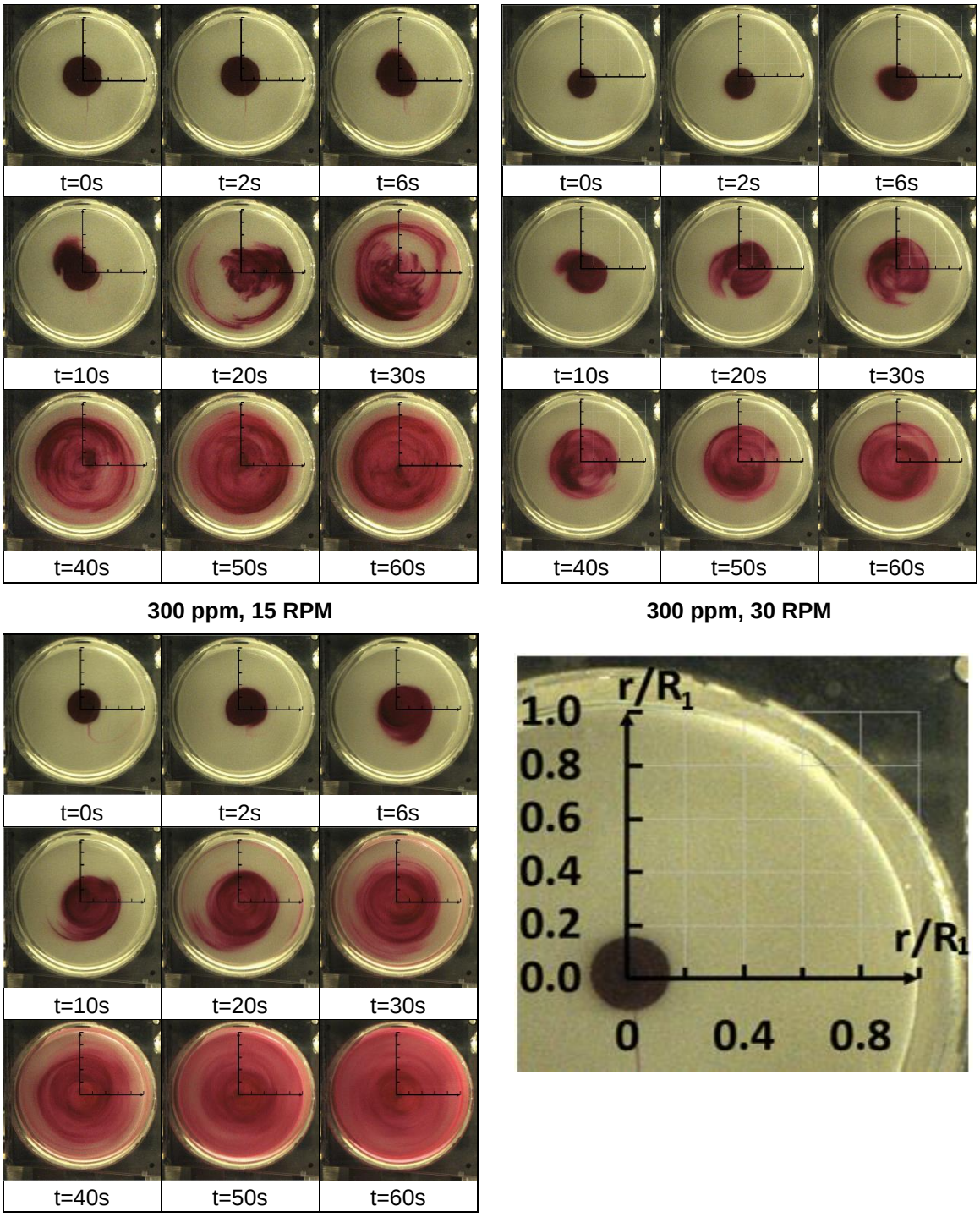

Figure 6.21 Time sequences of flow visualization images for 300 ppm polymer concentration for disk rotational speeds of 15 RPM, 30 RPM, and 60 RPM.

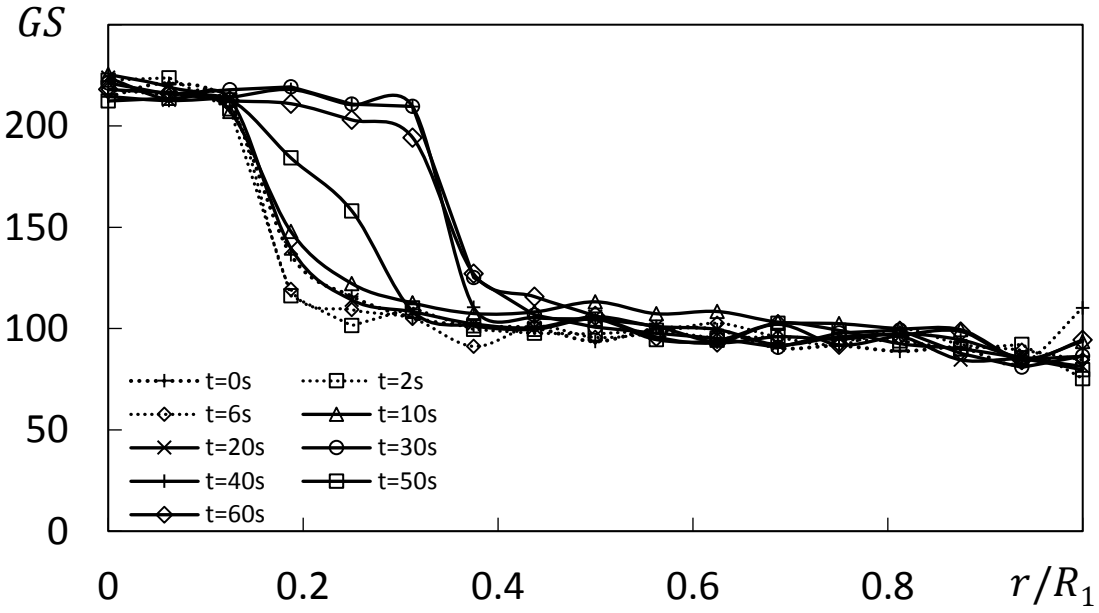

Figure 6.22 Gray scale variations with normalized radius location for 150 ppm polymer concentration for disk rotational speeds of 15 RPM.

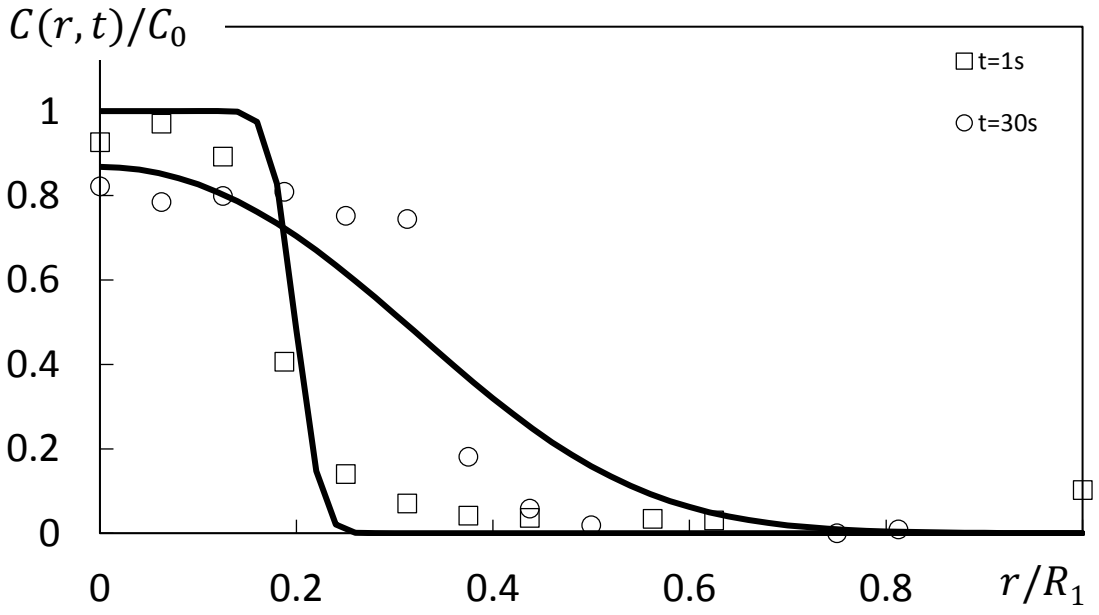

Figure 6.23 Comparison between experimental data and theoretical prediction from Lee et al. (2004) for 150 ppm polymer concentration and disk rotation speed of 15 RPM.

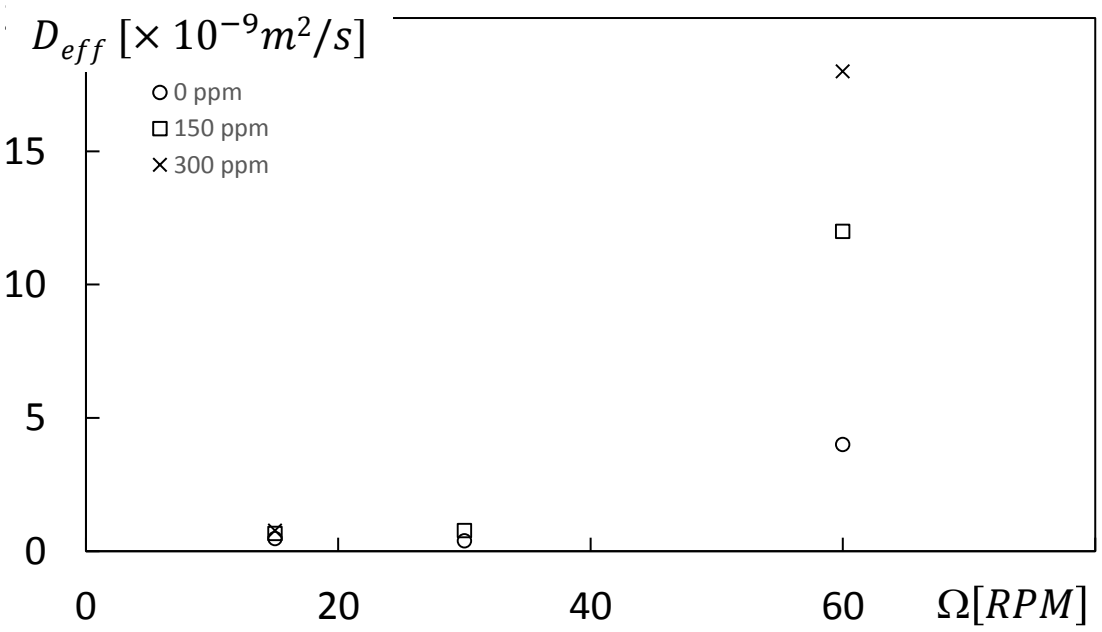

Figure 6.24 Effective diffusion coefficient variations with rotation speed for different polymer concentrations.

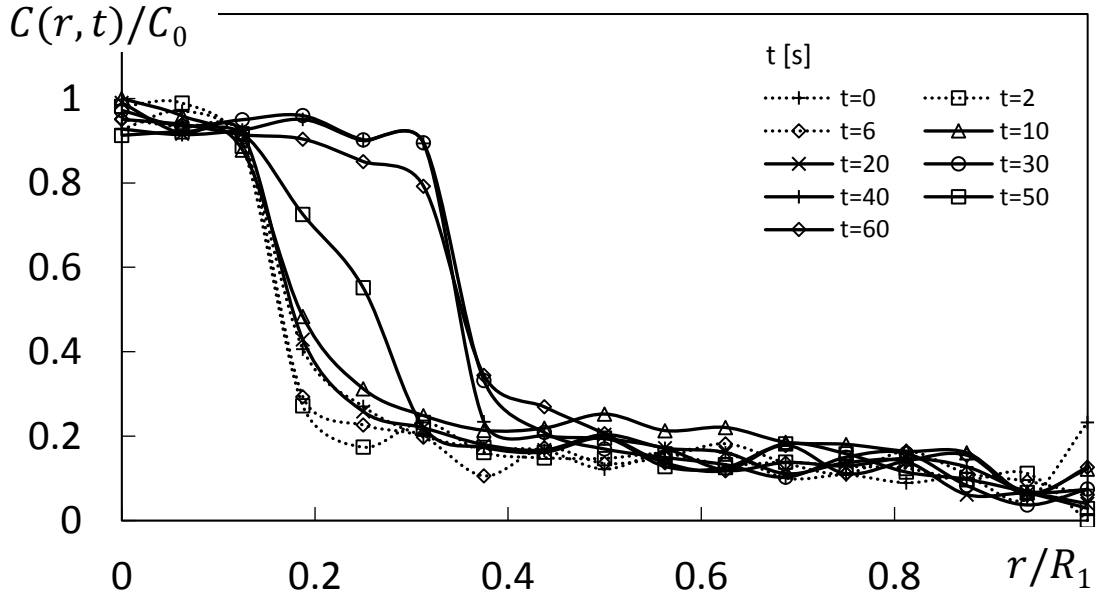

Figure 6.25 Normalized concentration profile variations with normalized radius location for 150 ppm polymer concentration and rotation speed of 15 RPM.

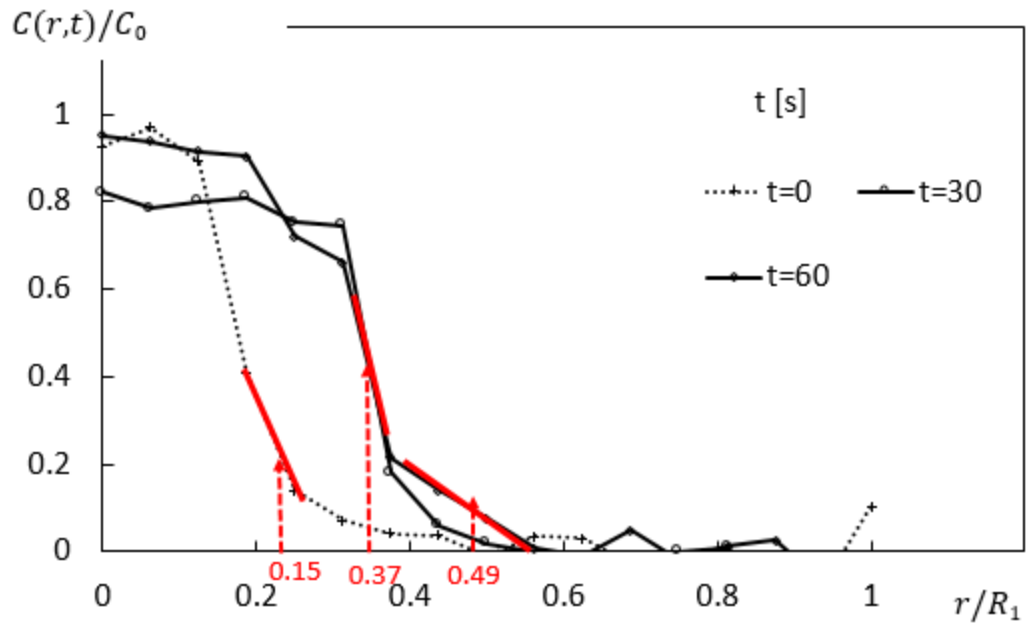

Figure 6.26 Normalized concentration profile variations, illustrating dye front determination for 150 ppm polymer concentration and rotation speed of 15 RPM.

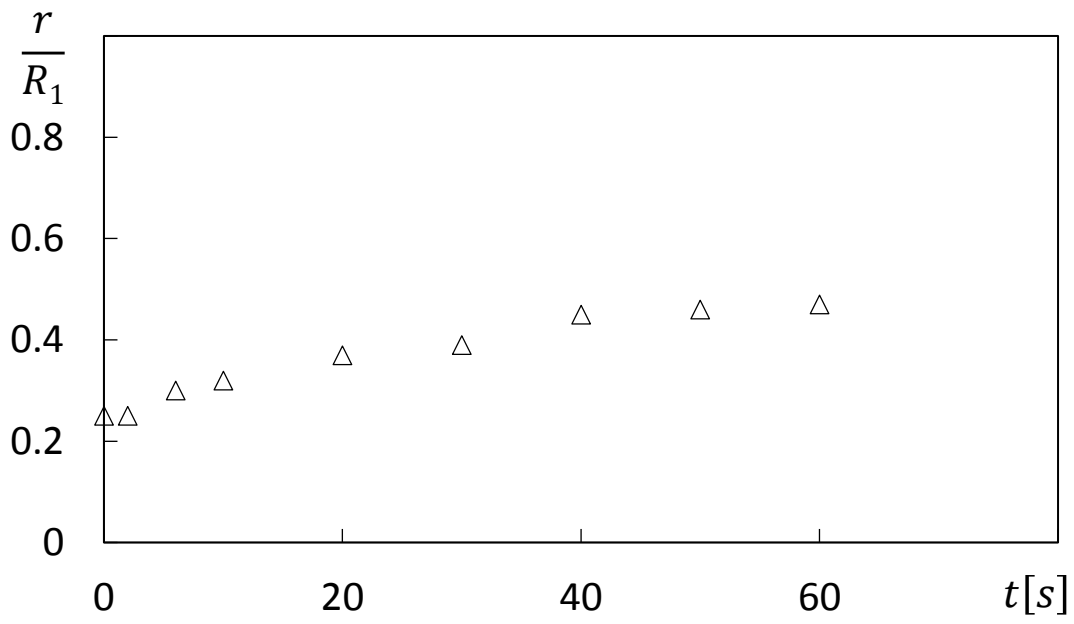

Figure 6.27 Dye front variation with time for 150 ppm polymer concentration and rotation speed of 15 RPM.

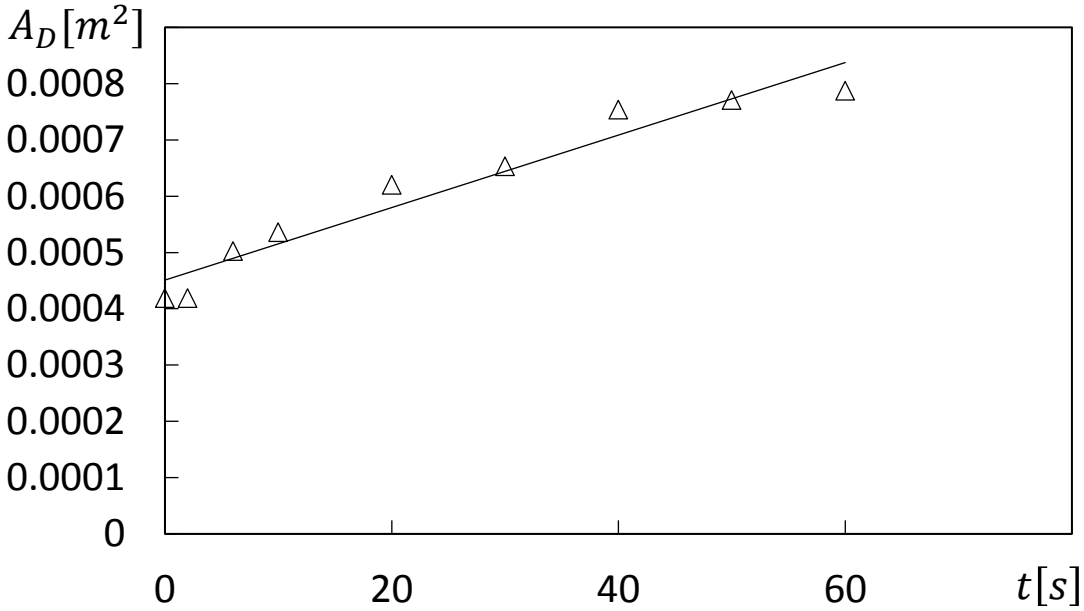

Figure 6.28 Diffusion area variation with time for 150 ppm polymer concentration and rotation speed of 15 RPM.

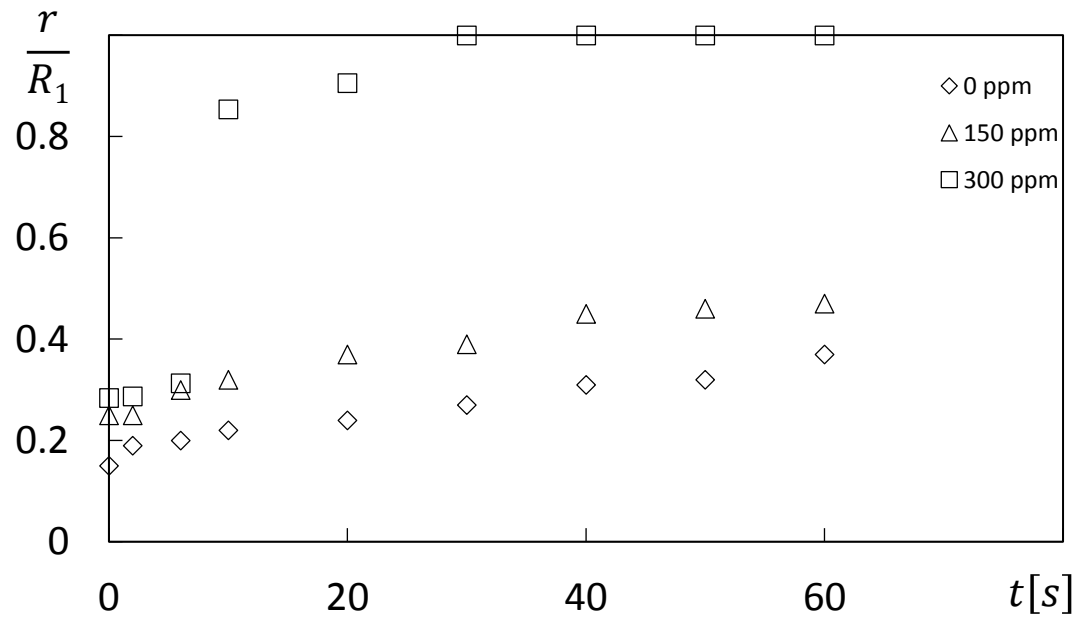

Figure 6.29 Dye front variations with time for different polymer concentrations and rotation speed of 15 RPM.

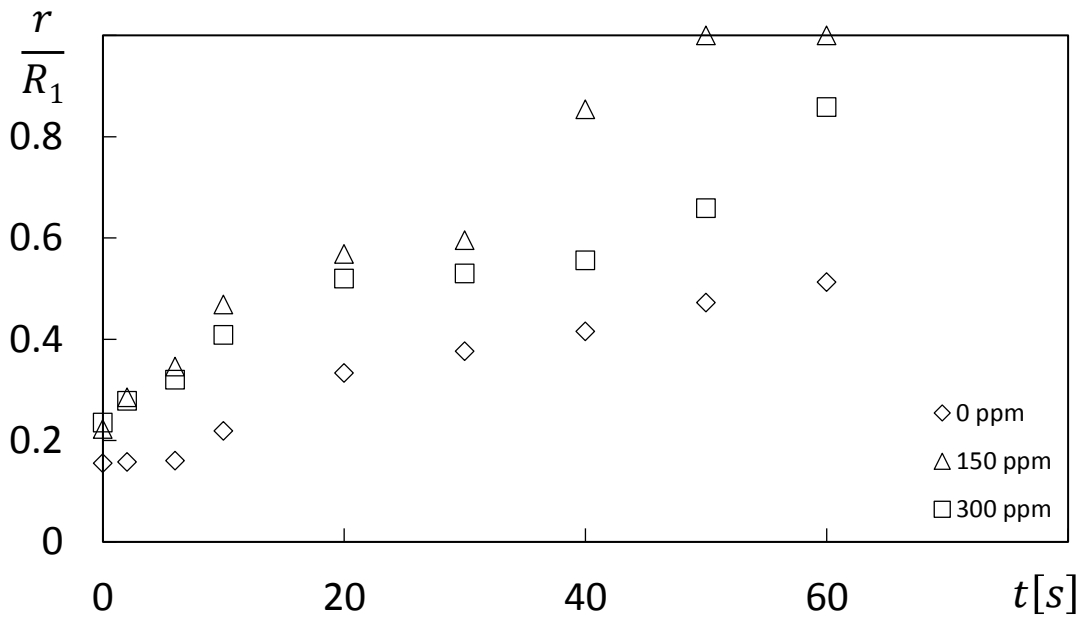

Figure 6.30 Dye front variations with time for different polymer concentrations and rotation speed of 30 RPM.

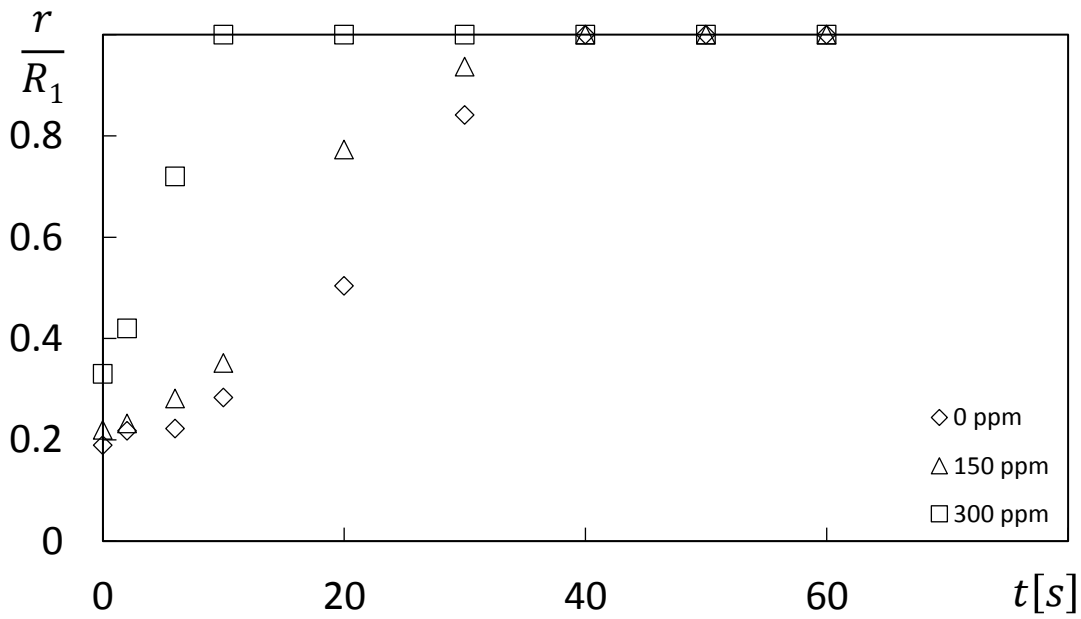

Figure 6.31 Dye front variations with time for different polymer concentrations and rotation speed of 60 RPM.

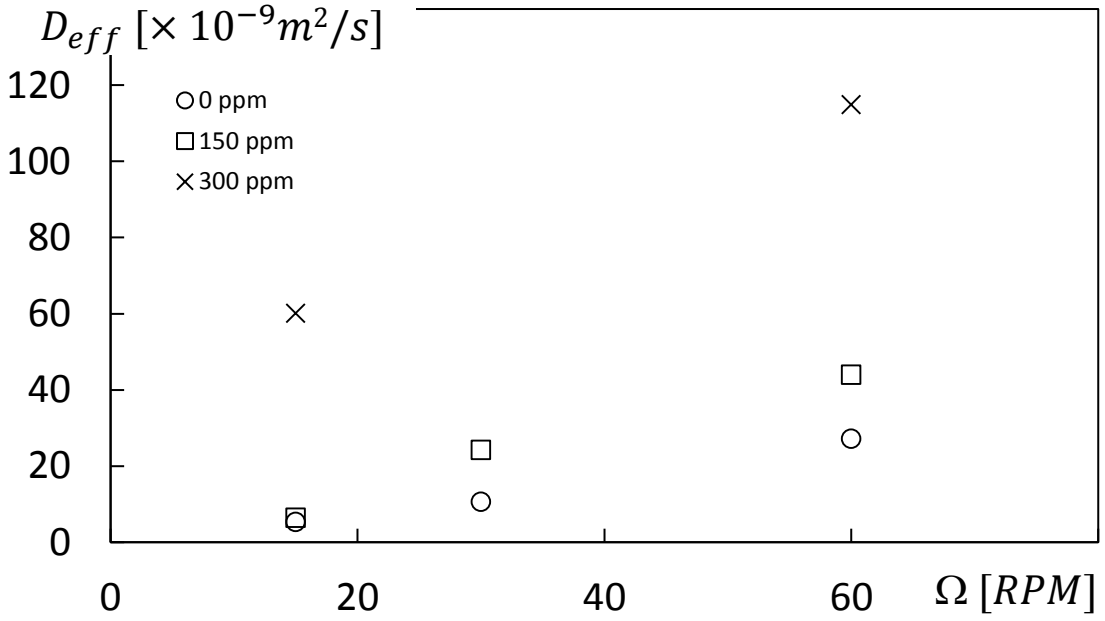

Figure 6.32 Effective diffusion coefficient variations with rotation speed for different polymer concentrations.

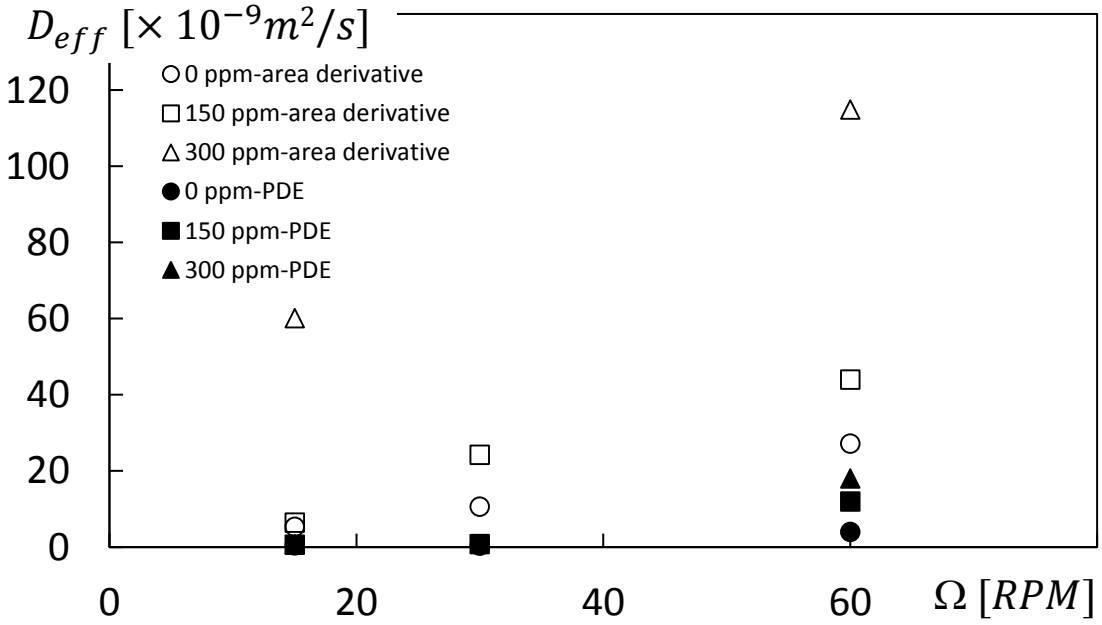

Figure 6.33 Effective diffusion coefficient variations with rotation speed for different polymer concentrations. Comparison between PDE approach and area derivative approach.

CHAPTER 7

EXPERIMENTAL RESULTS: DIFFUSION RATE IN ROTATIONAL COUETTE FLOW

The present chapter gives flow visualization images, obtained using fluorescein dye, and procedures for determination of the dye front, including related statistical properties, along with effective diffusion coefficient values. Experiments are conducted for a gap height of 5 mm at four different disk rotations speeds, and polymer concentrations of 0 ppm, 80 ppm, 100 ppm, 150 ppm, and 300 ppm. Associated shear rates range from 0 1/s to 31.92 1/s.

This chapter consists of four parts: (1) analysis of flow visualization time sequence images; (2) effective diffusion coefficient analysis; (3) elastic instability onset based upon effective diffusion coefficient data; (4) missing/diffusion rate parameter g determination and associated data trends.

7.1 Analysis of Flow Visualization Time Sequence Images

Figure 7.1 compares time sequences of flow visualization images for a time period of 60 seconds for 0 ppm, 100 ppm, and 300 ppm polymer solutions. Rotation speeds is 40 RPM (4.19 rad/s) and gap height is H of 5 mm. As shown in Fig. 7.1a, pure sucrose solution for 0 ppm shows that the dye follows the trajectory of a laminar flow.

The associated dye paths are well defined, and smooth, with very little distortion for different times up to a total time period of 60s. When polymers are present with ρ=100 ppm and ρ=300 ppm, Figs. 7.1b and 7.1c show that the dye distribution exhibits turbulent behavior, with larger effective diffusion rates compared to the 0 ppm solution. Thus, as polymer concentration increases, the diffusion speed and flow behavior are dramatically different as polymer concentration increases, as rotational speed is constant. With ρ=100 ppm and ρ=300 ppm, the dye spreads over the entire radial extent of the flow, throughout the entire flow passage, within 30s to 40s. Effective diffusion is significantly enhanced, compared to flows without polymers present. Overall, the present flow is visualization results, show that contributions from polymer addition on effective diffusion are dramatic.

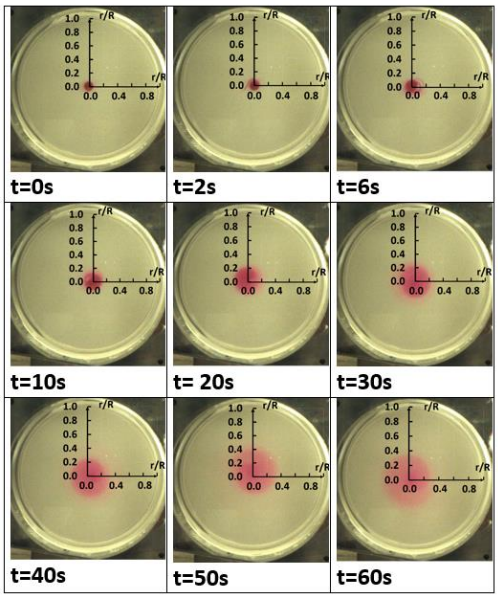
t=0s
t=2s
t=6s
t=10s
t= 20s
t=30s
t=40s
t=50s
t=60s

(a)

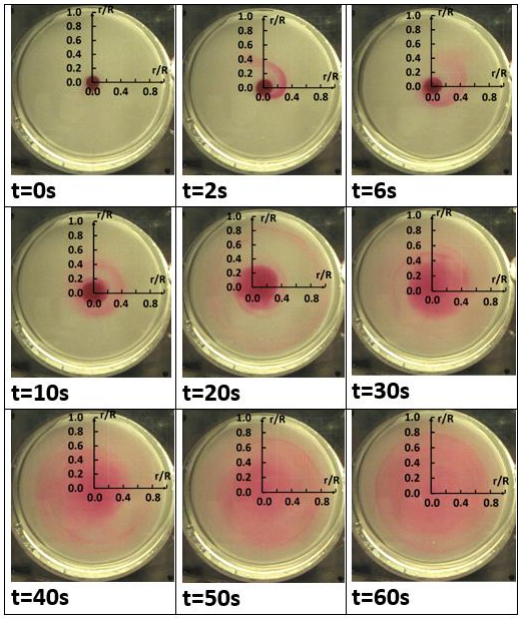
t=0s
t=2s
t=6s
t=10s
t=20s
t=30s
t=40s
t=50s
t=60s

(b)

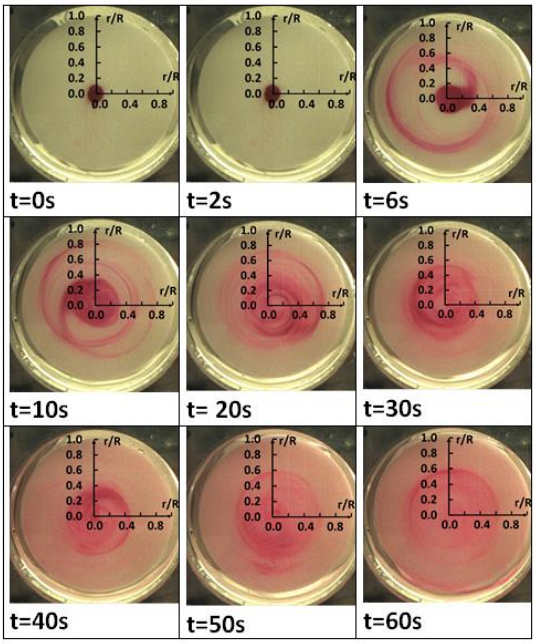

(c)

Figure 7.1 Time sequences of flow visualization images at a rotation speed of 40 RPM (4.19 rad/s) with a gap height H of 5 mm: (a) 0 ppm; (b) 100 ppm; (c) 300 ppm.

The results given in Figs. 7.2, 7.3, and 7.4, are determined from the data presented in Fig. 7.1. Figs. 7.2 and 7.3 present gray scale data, and normalized dye concentration variations, as they vary with normalized radius location at different times. The corresponding dye front determination is illustrated by results given in Fig. 7.4.

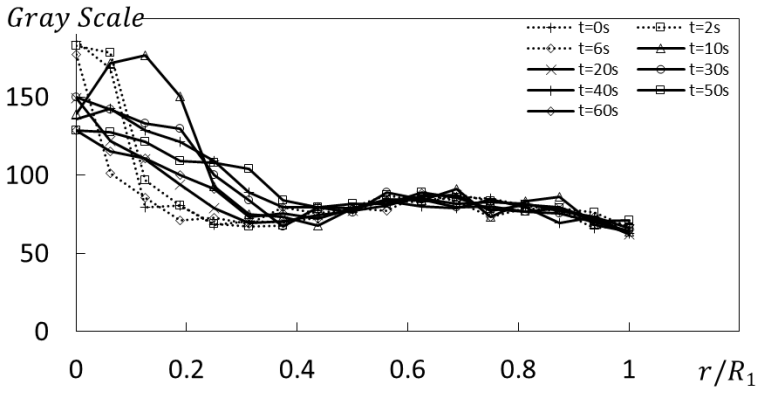

(a)

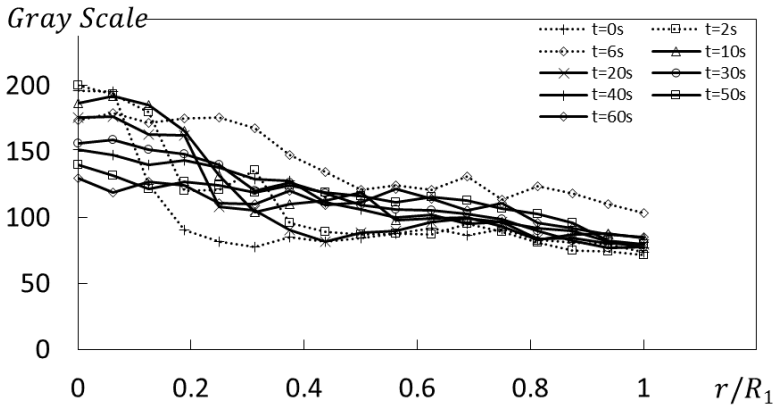

(b)

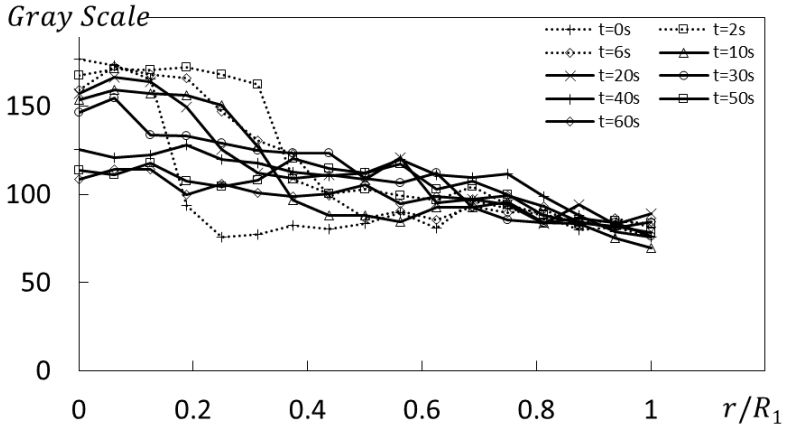

(c)

Figure 7.2 Gray scale variations with normalized radius location at different times for a rotation speed of 40 RPM (4.19 rad/s) with a gap height H of 5 mm: (a) 0 ppm; (b) 100 ppm; (c) 300 ppm.

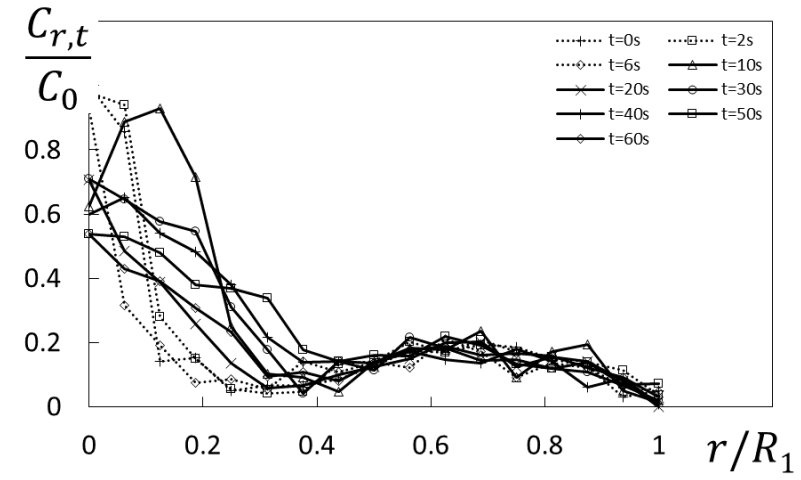

(a)

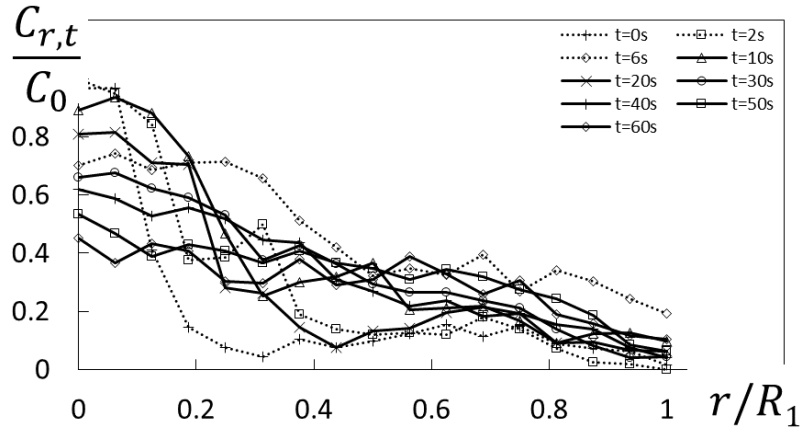

(b)

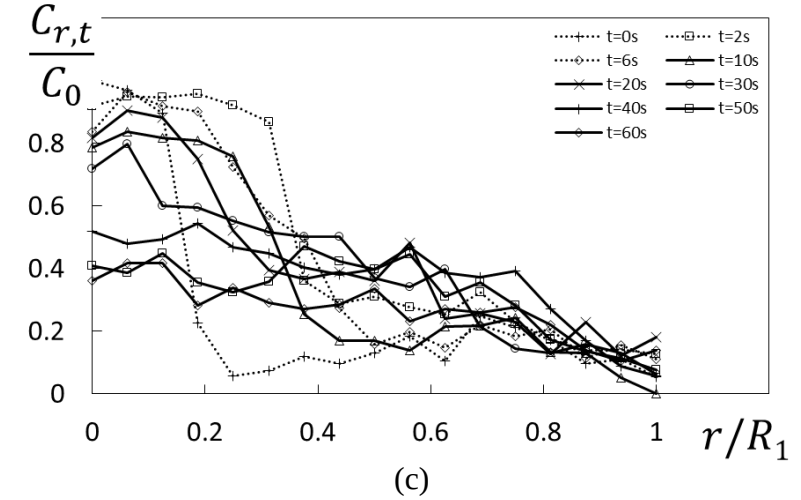

(c)

Figure 7.3 Normalized dye concentration variations with normalized radius location at different times for a rotation speed of 40 RPM (4.19 rad/s) with a gap height H of 5 mm: (a) 0 ppm; (b) 100 ppm; (c) 300 ppm.

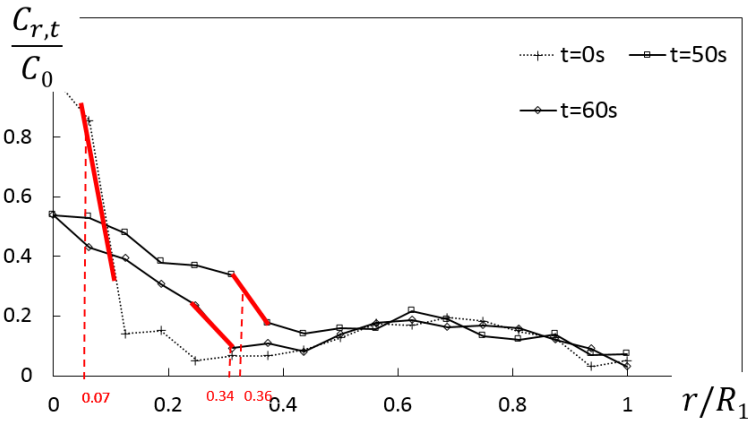

(a)

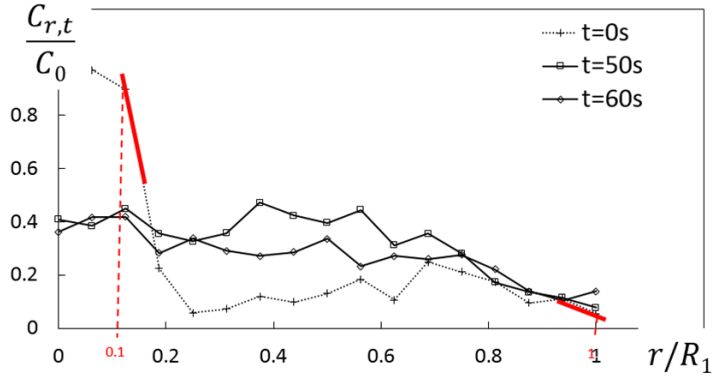

(b)

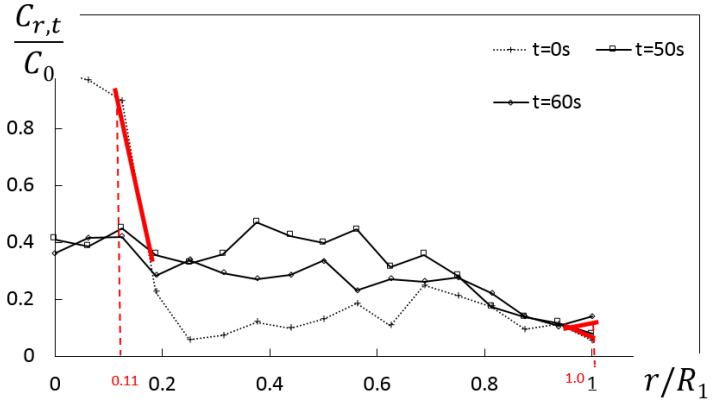

(c)

Figure 7.4 Identification of maximum slope of normalized concentration variations with normalized radius location at different times for a rotation speed of 40 RPM (4.19 rad/s) with a gap height H of 5 mm: (a) 0 ppm; (b) 100 ppm; (c) 300 ppm.

Figure 7.5 shows dye front variations with time for different polymer concentrations. Here, dye fronts associated with higher polymer concentrations exhibit higher r/R_1 values as time increases. Fig. 7.6 shows dye front area variations with time, also for different polymer concentrations.

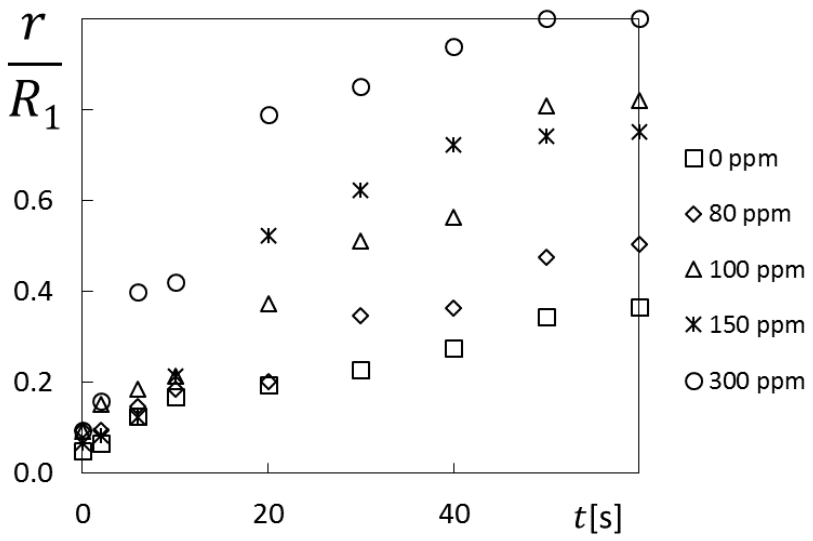

Figure 7.5 Dye front radical location variations with time for different polymer concentrations at a rotation speed of 40 RPM (4.19 rad/s) with a gap height H of 5 mm.

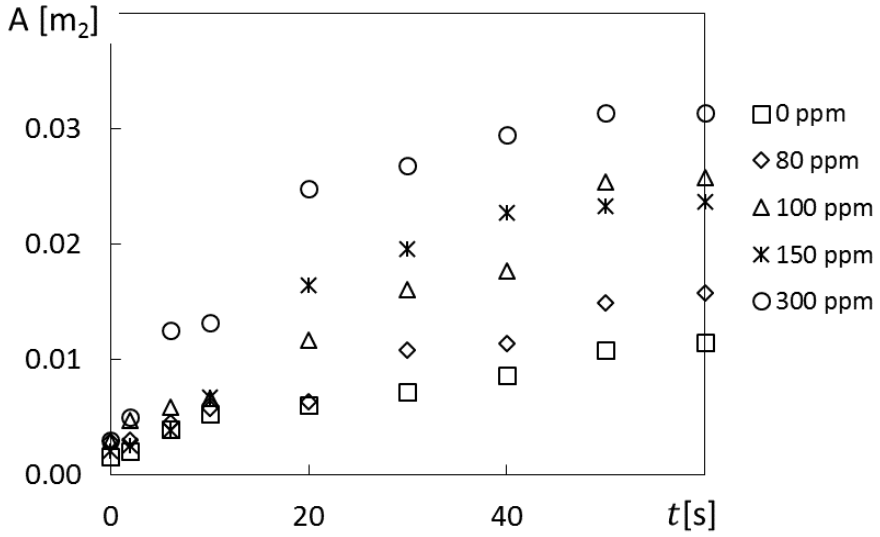

Figure 7.6 Dye front area variations with time for different polymer concentrations at a rotation speed of 40 RPM (4.19 rad/s) with a gap height H of 5 mm.

Overall, values for derivative of dye front area in Fig. 7.7 show increasing magnitudes with increasing polymer concentrations, as rotation speed and shear rate are held constant. For a constant polymer concentration, higher derivative values are associated with higher rotation speeds, which evidence stronger non-Newtonian flow influences from elastic instabilities, and thus, greater deviations from Newtonian fluid behavior. Within the present RCF, effective diffusion increases are associated with larger local mixing and more pronounced instabilities within the flows.

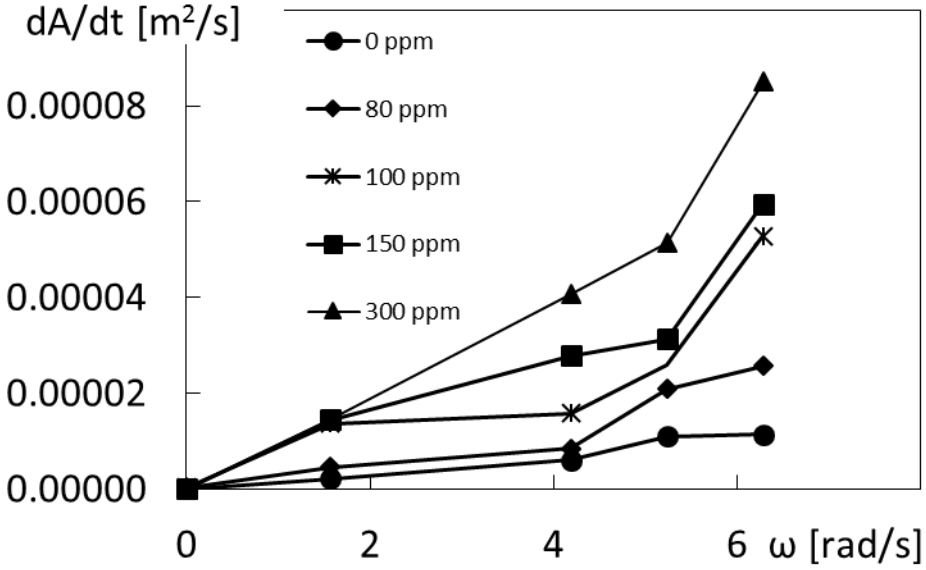

Figure 7.7 Derivative of dye front area variation with rotation speed for different polymer concentrations with a gap height H of 5 mm.

7.2 Effective Diffusion Coefficient Analysis

Figure 7.8 shows predicted normalized fluorescein concentration variations as they vary with normalized radius location for a rotational speed of 40 RPM (4.19 rad/s) and gap height H of 5mm, for 0 ppm, 100 ppm, and 300 ppm polymer solutions. Fig. 7.9 shows effective diffusion coefficient variations with rotation speed, also for different

polymer concentrations. Higher concentration solutions generally give larger effective diffusion coefficient values, when compared at a particular rotation speed. Fig. 7.10 shows β value variations with rotation speed for different polymer concentrations. Fig. 7.11 then compares effective diffusion coefficients determined using the PDE approach and area derivative approach.

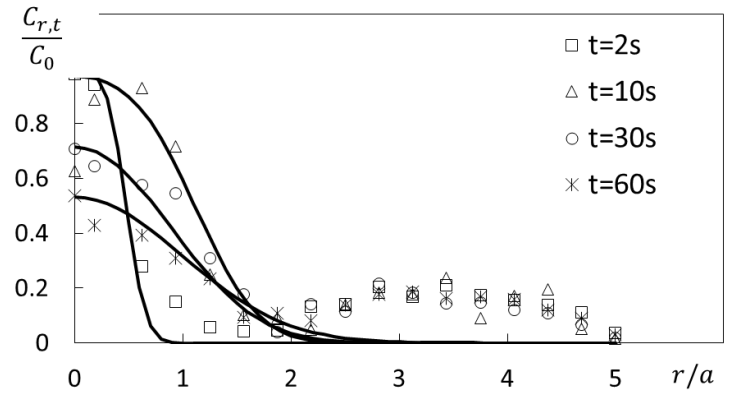

(a)

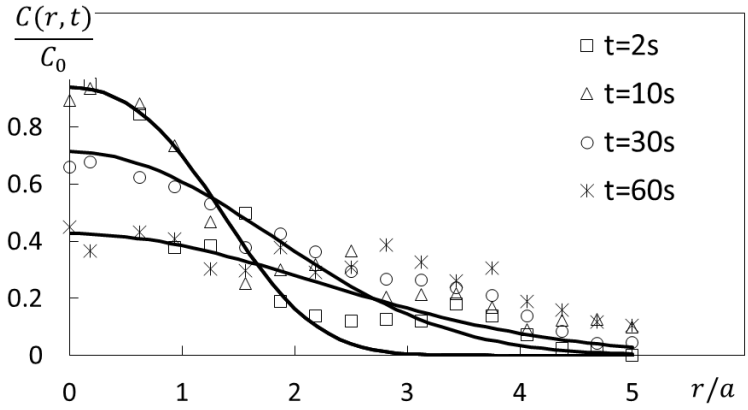

(b)

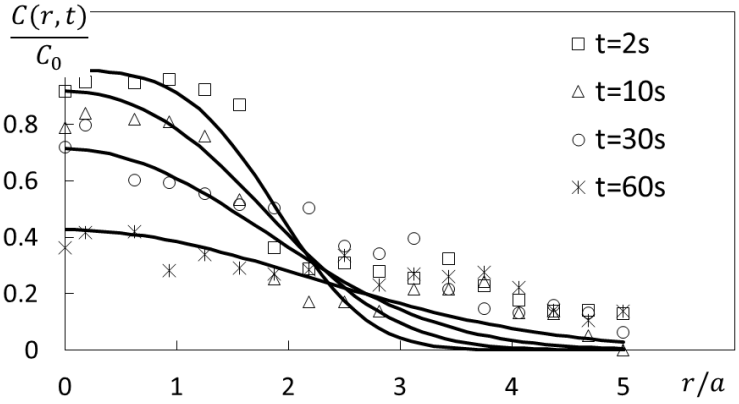

(c)

Figure 7.8 Comparisons between experimental and theoretical predictions using Lee et al. (2004) approach for normalized concentration profiles for a rotation speed of 40 RPM (4.19 rad/s) and gap height H of 5 mm: (a) 0 ppm; (b) 100 ppm; (c) 300 ppm.

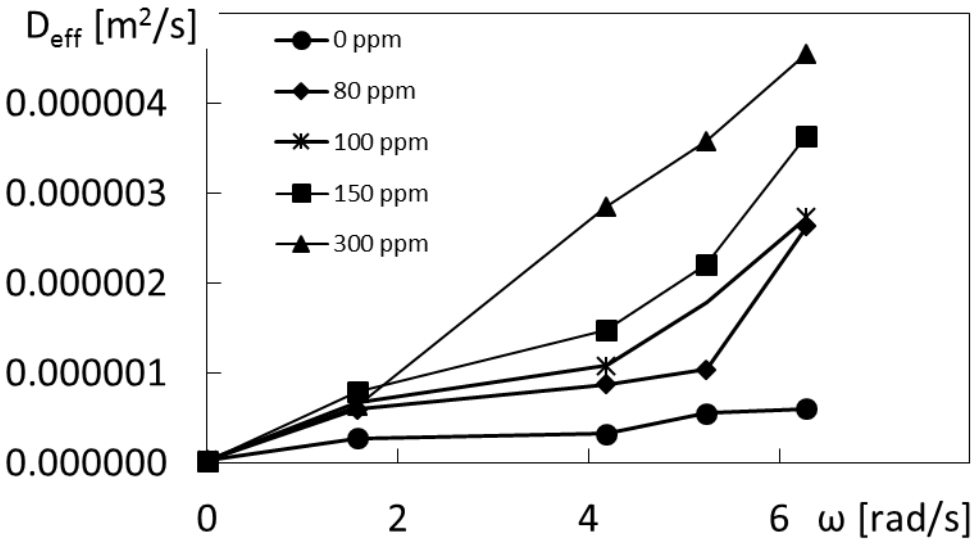

Figure 7.9 Effective diffusion coefficient D_{eff} variations with rotation speed, determined using the PDE approach, for different polymer concentrations with a gap height H of 5 mm.

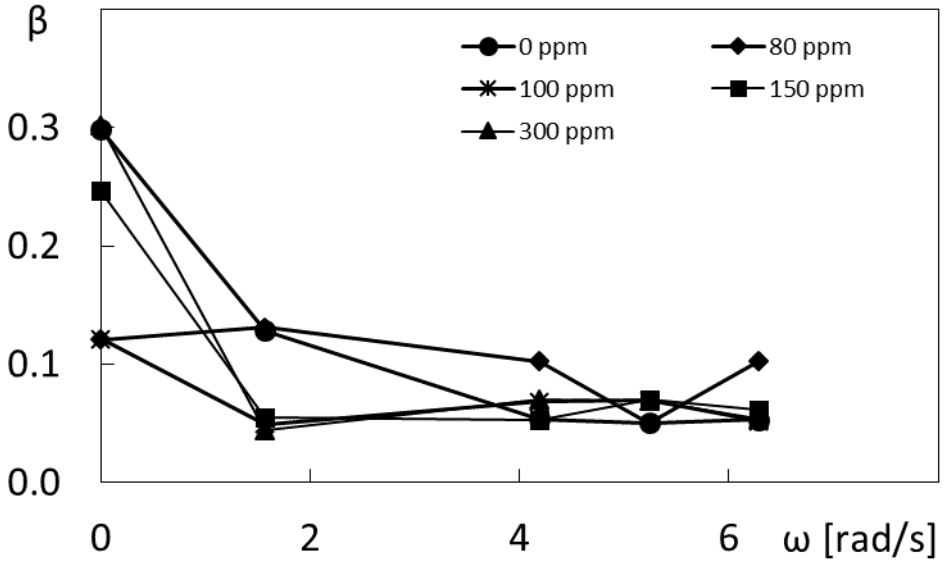

Figure 7.10 $\beta=(dA/dt)/D_{eff}$ parameter variations with rotation speed for different polymer concentrations for gap height H of 5 mm.

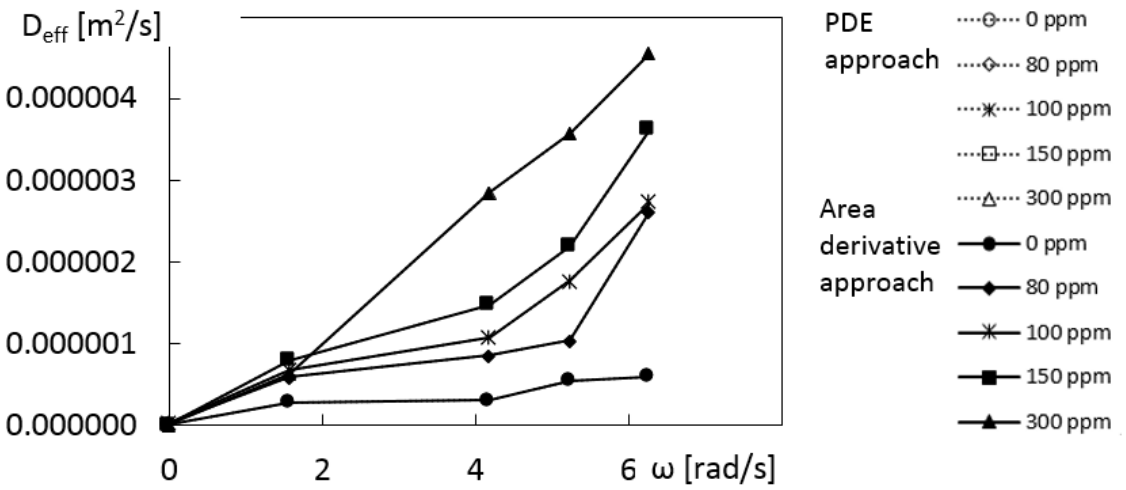

Figure 7.11 Comparisons of effective diffusion coefficients D_{eff} variations, for the PDE approach and the area derivative approach, for different rotation speeds for a gap height H of 5 mm.

7.3 Elastic Instability Onset Based Upon Effective Diffusion Coefficient Data

Figure 7.12 shows laminar, transition, and elastic instability onset flow conditions at different shear rates and different polymer concentrations within the Rotating Couette Flow device for different diffusion analysis approaches. Associated elastic instability onset values are D_{eff}=0.000001 m^2/s, and $d(r/R_1)/dt$=0.011 1/s. According to the results in Fig. 7.12, the onset of elastic instabilities occurs at lower shear rate as polymer concentration increases. The PDE approach and area derivative approach are related to each other using

$$D_{eff} = \beta\left(\frac{dA}{dt}\right) \tag{7.1}$$

where data, such as are presented in Fig. 7.9, are used for determination of D_{eff}, and data, such as are presented in Fig. 7.7 are used for determination of (dA/dt).

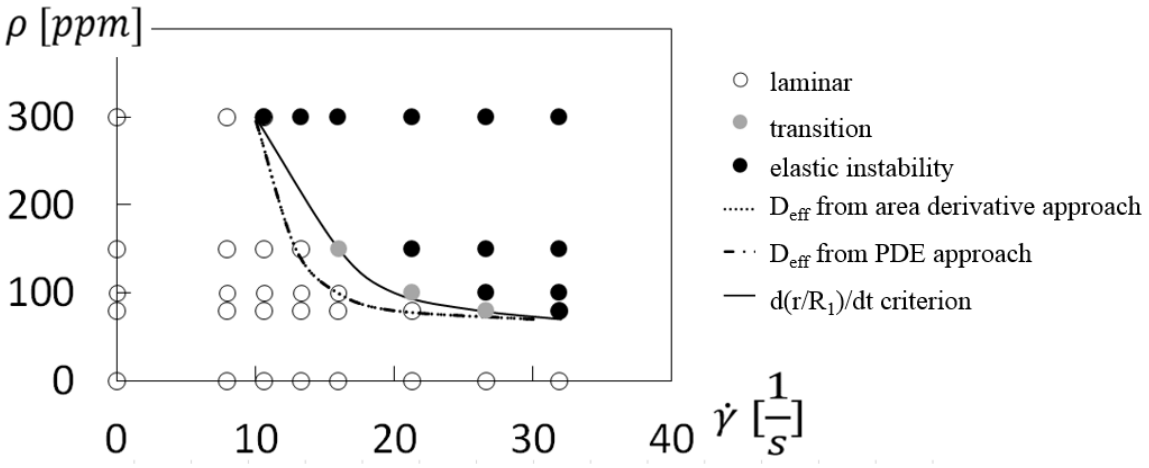

Figure 7.12 Laminar, transition, and elastic instability onset flow conditions at different shear rates and different polymer concentrations within the Rotating Couette Flow device for different diffusion analysis approaches.

7.4 Mixing/Diffusion Rate Parameter g Determination and Associated Data Trends

To characterize the mixing/diffusion rate of fluorescein dye within the solutions, parameter g is employed, as given by

$$A = A_0[1 - \exp(-gt)] \tag{7.2}$$

where $A = \frac{r}{R_1}$, A_0 is equal to 1.0, t is time, and g is the mixing/diffusion rate (Ottino, 1987).

Figure 7.13 shows a comparison of Eqn. (7.2) with normalized dye front variations with time and polymer concentrations for a gap height H of 5mm. Predicted data are generally in agreement with experimental results. Magnitudes of $A = \frac{r}{R_1}$ increase with polymer concentration at a specific shear rate. Fig. 7.14 then shows mixing/diffusion rate g parameter variations with rotation speed for different polymer concentrations, also for a gap height H of 5mm. Magnitudes of effective diffusion rate generally increase, as

fluid rotation speed increases. Mixing/diffusion rate value increases are associated with larger polymer concentrations, for each rotational speed considered. Finally, Fig. 7.15 presents laminar, transition, and elastic instability onset flow conditions at different shear rates and different polymer concentrations within the Rotating Couette Flow device based on the g mixing/diffusion rate parameter. Note that the onset of elastic instability determined from flow visualization data is in approximate agreement with the onset shown in Fig. 7.15.

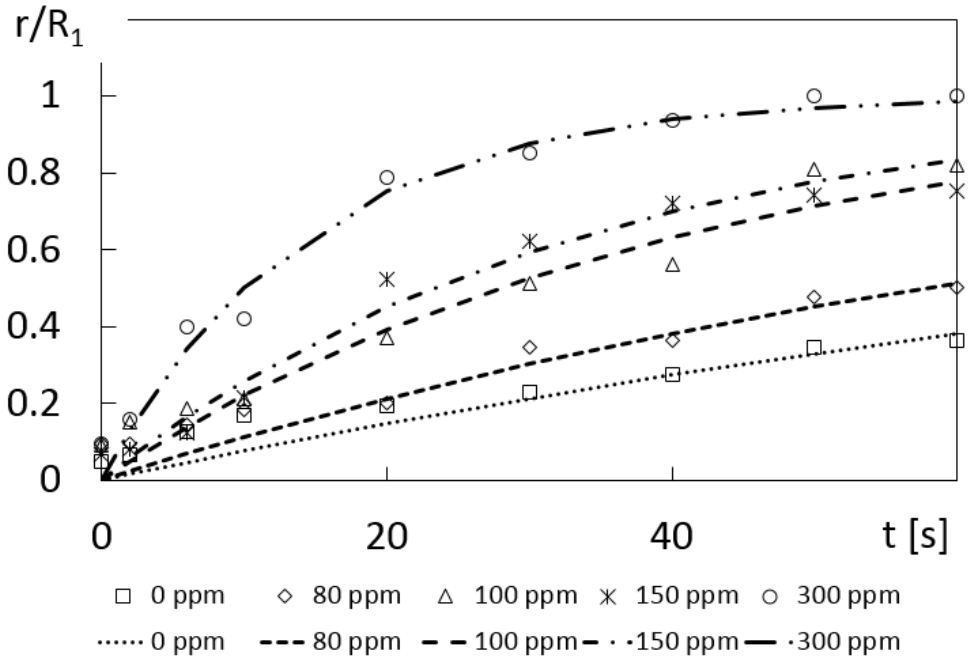

Figure 7.13 Comparison of Eqn. (7.2) with normalized dye front variations with time and polymer concentration for a gap height H of 5mm.

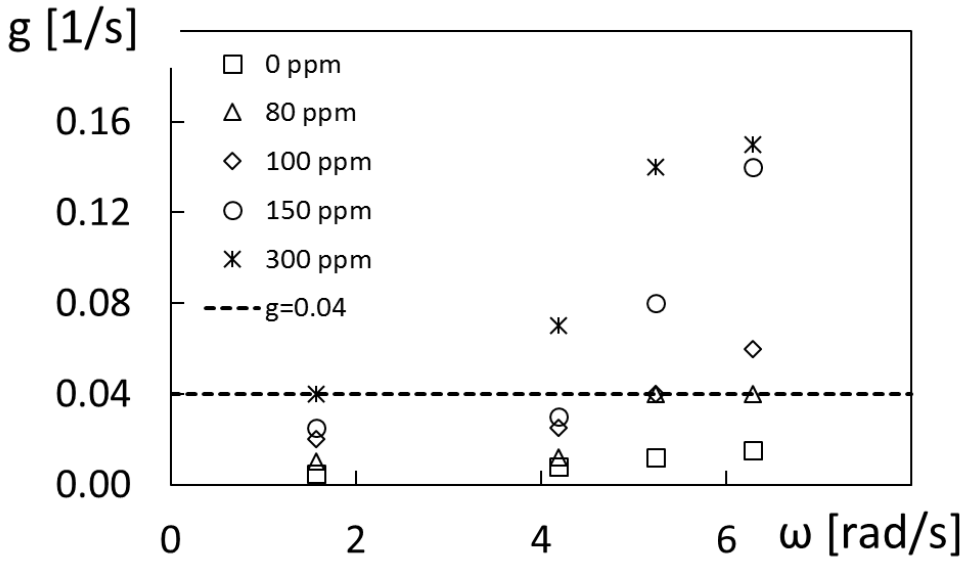

Figure 7.14 Mixing/diffusion rate g parameter variations with rotation speed for different polymer concentrations for a gap height H of 5mm.

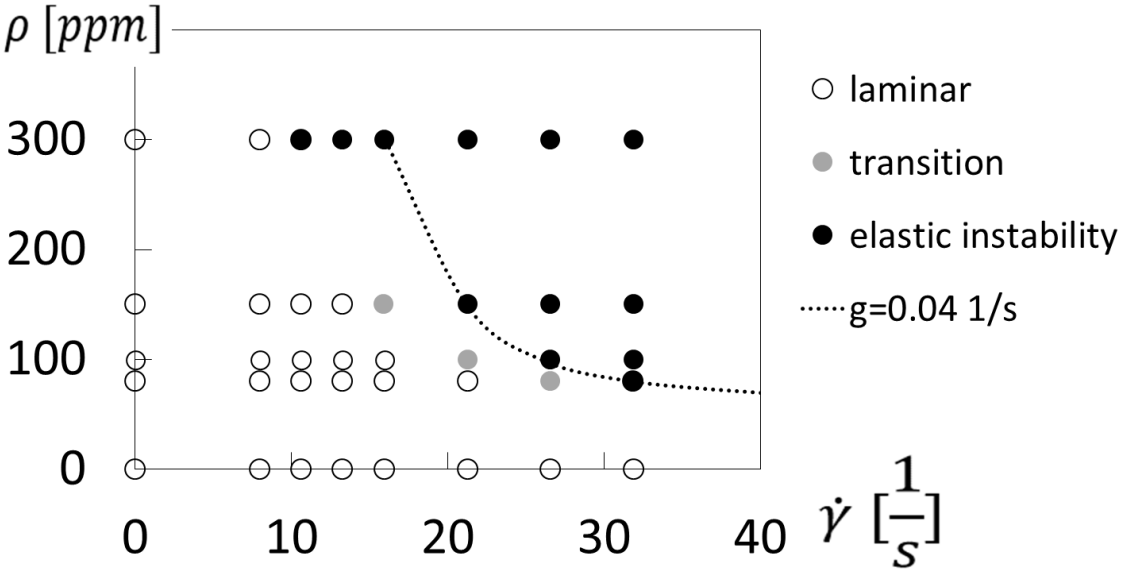

Figure 7.15 Laminar, transition, and elastic instability onset flow conditions at different shear rates and different polymer concentrations within the Rotating Couette Flow device based on the g mixing/diffusion rate parameter.

CHAPTER 8

POLYMER SOLUTIONS RHEOLOGICAL PROPERTIES

Within this chapter, the rheological properties, including overall viscosity, and elastic and viscous modulus values, are determined experimentally and theoretically. Five different concentrations of sucrose-based polymer solution samples, including 0 ppm, 80 ppm, 100 ppm, 150 ppm and 300 ppm, are considered. Besides the sucrose solution, distilled water is also tested. A state-of-the-art commercial rheometer, Anton-Paar 92002 MCR 302 Modular Compact Rheometer, with a sample-adaptive motor controller and normal force sensor, is used to determine the rheological properties. The Carreau-Yasuda model (Yasuda et al., 1981) is applied to predict the overall viscosity and the Zimm equation (Zimm, 1956; Del Guidice, 2017) is used to calculate the relaxation time. The theoretical results are generally in good agreement with the experimental data.

Present chapter consists of four sections: testing facility, overall viscosity measurement and determination, relaxation time determination, and procedures for separation of elastic and viscous modulus values.

8.1. Testing Facility

8.1.1 Testing facility geometry and initialization

Measurement of rheological properties are determined for sucrose-based, viscoelastic solutions with polyacrylamide using a state-of-the-art commercial Anton-Paar 92002 MCR 302 Modular Compact Rheometer, with a sample-adaptive motor controller and normal force sensor, which is shown in Figures 8.1 and 8.2. The corresponding series number of the rheometer is 52131. Polymer mixture rheological data are employed to provide information regarding absolute viscosity properties of the different fluids which are used for testing at different magnitudes of shear rate. The rheometer is connected to a DELL Latitude 3450 personal computer using the USB cable. RheoCompass ™ software is installed within the computer provided by Anton Parr, which is used for the control of the Anton-Paar MCR rheometer. The measurement parameters, test definition, results as well as all settings, are set in the software. The RheoCompass™ software also contains various templates suited to different applications and methods. The templates are selected from the application program shown at the first start of the software, as shown in Figure 8.3. This figure as well as the contents of Figures 8.4, 8.5, 8.6, 8.7, 8.8, 8.11 and 8.12 are taken from the rheometer operation manual (Anton-Paar rheometer manual).

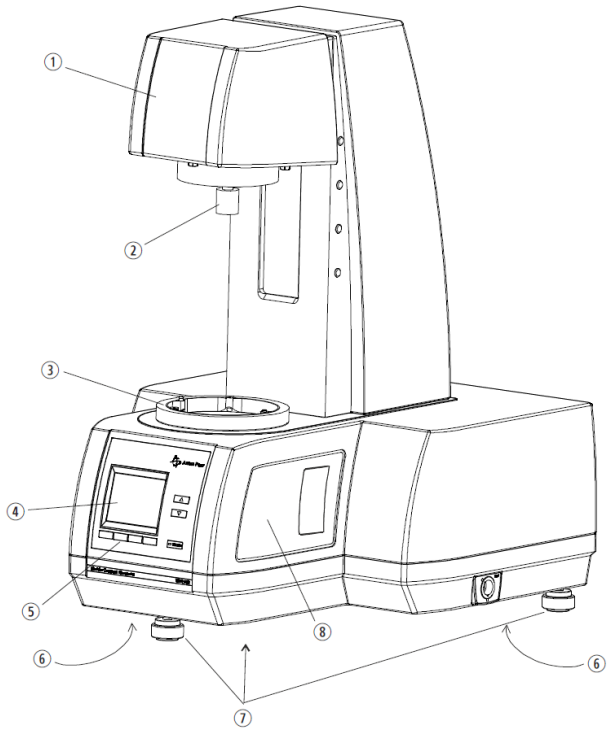

1	MCR measuring head
2	MCR coupling for measuring system
3	Flange ring (Temperature device holder): Mechanical self-alignment of all accessories
4	Color display
5	Soft keys
6	Recessed grip
7	Three adjustable feet
8	Right side cover

Figure 8.1 Configuration of Anton-Paar 92002 MCR 302 Modular Compact Rheometer.

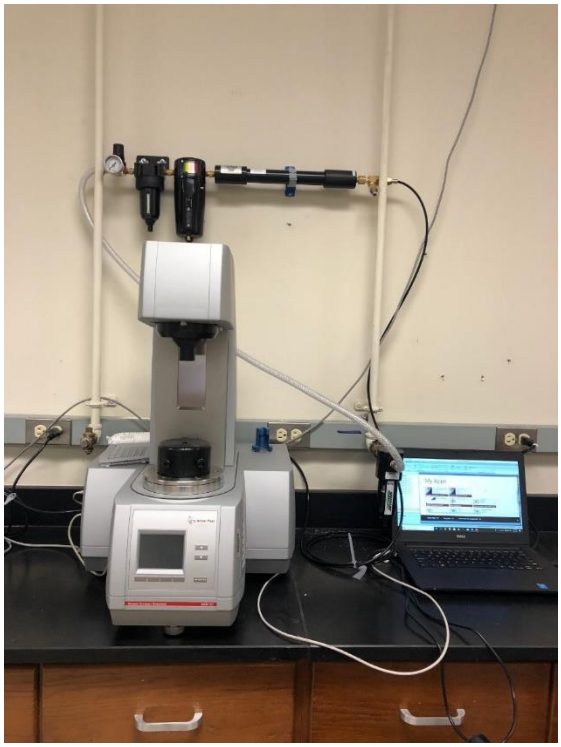

Figure 8.2 Photograph of Anton-Paar 92002 MCR 302 Modular Compact Rheometer.

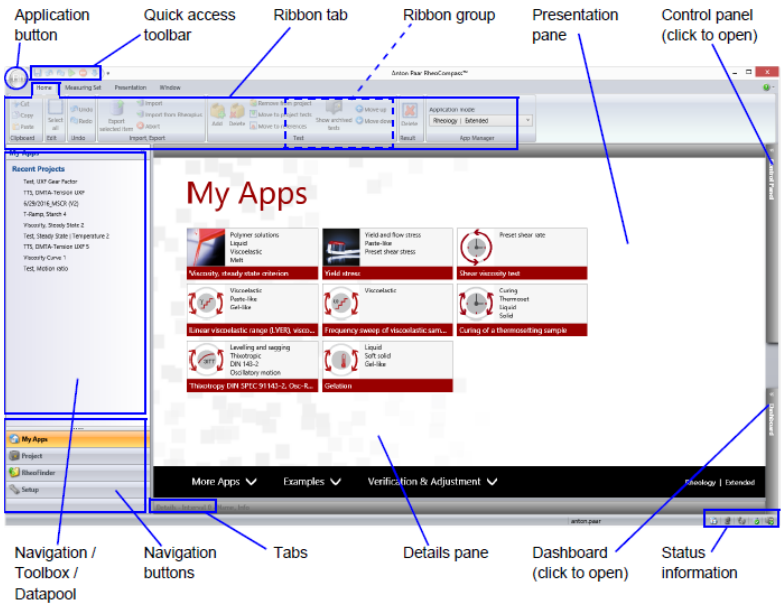

Figure 8.3 Anton-Paar 92002 MCR 302 Modular Compact Rheometer control panel for the main elements of RheoCompass™ at start.

The concentric cylinder systems are used to determine the rheology properties of the samples. Figures 8.4 and 8.5 show the geometry and dimensions of the system, CC27 measuring system testing chamber. Before the testing, make sure that the air supply and filter system are connected. The air supply switch should be in vertical position to the wall. The air pressure is read using the gas-pressure gauge, whose value should be around 500 kPa. Switch the instrument on and wait for the instrument to boot. After the MCR has finished the boot procedure and is ready, the screen in Figure 8.6 is displayed. Physical properties such as current temperature and positions are displayed on the screen. A volume amount consisting of 19.28 ml sample solutions are then loaded in the chamber. A mark inside the cup indicates when this volume for the sample is fulfilled. The information on the cup configuration is provided for the rheometer under the measuring system CC27 in Figure 8.5.

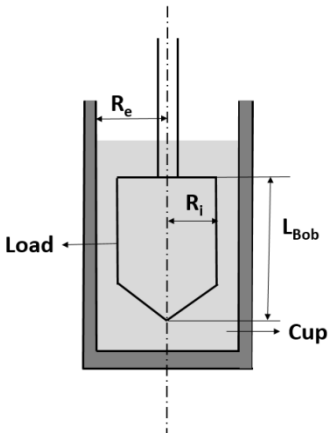

R_i (mm)	R_e (mm)	L_{Bob} (mm)
26.664	28.898	39.994

Figure 8.4 Geometry and dimensions of the rheometer testing chamber

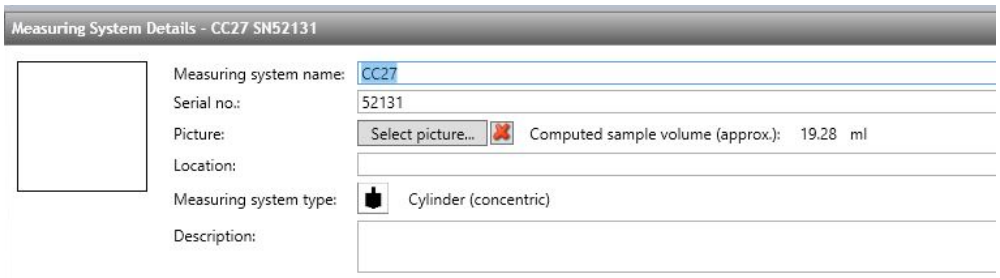

Figure 8.5 Anton-Paar 92002 MCR 302 Modular Compact Rheometer control panel for detail description of measuring system CC27.

Each sample is inserted into the measuring system slowly and carefully to prevent the formation of vapor bubbles. The measuring bob, whose vertical position is adjustable, is then lowered to the measuring position, which is 1 mm from the bottom of the cup. When in place, the bob is in complete contact with the sample being tested, as shown in Figure 8.5. The measuring position of the bob is controlled using RheoCompass™ Software. The original position is set to 60 mm for all testing. The control panel is also used to set the testing temperature. For the current investigation, the temperature is set to 20 ºC for all the testing. The current temperature and position of the bob are shown on the panel of the rheometer as shown in Figure 8.6. The setting of the measurement position is shown in Figure 8.7, which shows the original position is 60 mm from the bottom of the cup. 5 mm represents that the bob is lowered to a position of 5 mm first and then goes down to 1 mm with a much slower speed to avoid the formation of vapor bubbles.

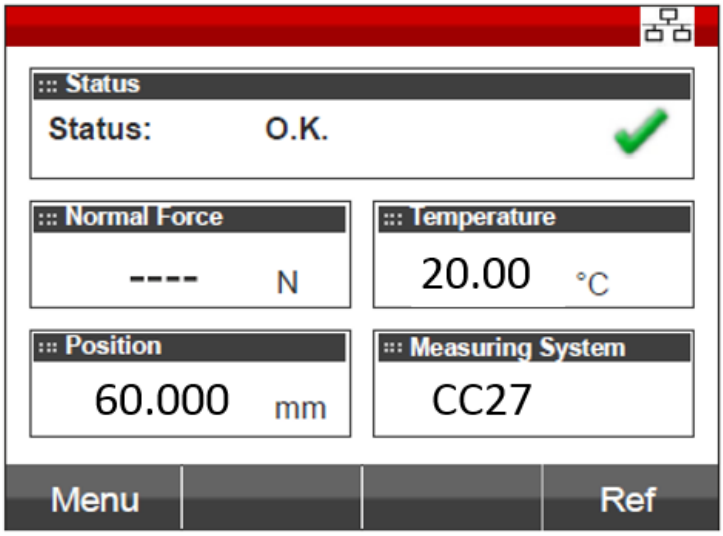

Figure 8.6 Anton-Paar 92002 MCR 302 Modular Compact Rheometer controlpanel for MCR display when the Rheometer is ready.

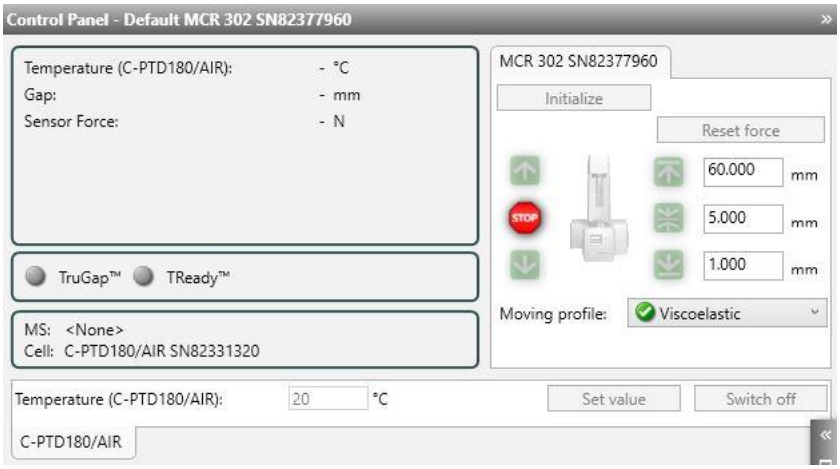

Figure 8.7 Anton-Paar 92002 MCR 302 Modular Compact Rheometer control panel interface.

8.1.2 Sample preparation

For the preparation of samples used for the rheological properties testing, smaller amount of polymer solutions are prepared to provide uniform distributions of the polymer chains within each solution. Solutions are utilized with five different polymer concentrations: 0 ppm, 80 ppm, 100 ppm, 150 ppm and 300 ppm, where ppm refers to

parts per million. The viscoelastic solutions are prepared by adding polyacrylamide powder into the sucrose solution, which is 65% sucrose and 1% NaCl, in 204g distilled water. The procedure for mixing the stock solution is adopted from Abed et al. (2016). For example, to mix a 100 ppm solution, 0.030 g of PAAm (Polyacrylamide, MW = 18,000,000 Dalton, Polysciences Inc.) powder, 3 g of NaCl, and 195 g sucrose are dissolved in 102 g DI water, as the solution is gently combined for approximately 4 hours within a commercial mixer, JJ-1 Accurate Electronic Overhead 100 W Stirrer Mixer, with a propeller operating at very low rotational speed. The amounts of polymer powders are weighed using an electronical balance METTLER AJ100 by Mettler-Toledo Inc., and the amounts of distilled water and NaCl are weighed using an Adam PGL 2002 Precise Balance.

8.2. Overall Viscosity Measurement and Determination

8.2.1 Theoretical background

Viscosity of a fluid is the ratio of shear stress to shear rate, as given by

$$\eta = \frac{\sigma}{\dot{\gamma}} \tag{8.1}$$

where η is the overall viscosity, σ is the shear stress, and $\dot{\gamma}$ is the shear rate. Depending on the viscosity behavior as a function of shear rate and stress, fluids are characterized as Newtonian or non-Newtonian. For Newtonian fluid, viscosity is independent of shear rate and is a function of temperature only. In contrast to Newtonian fluid, a non-Newtonian fluid has a viscosity that depends on time or deformation history, which display a non-linear behavior between shear rate and shear stress. Viscoelastic fluids exhibits both liquid and solid like behavior which distinguishes them from other fluids (Sunthar, 2010). The deformation response of most polymers is viscoelastic, displaying characteristics of

both an elastic solid (reversible mechanical response) and a viscous liquid (irreversible mechanical response). However, dilute polymeric solutions are Boger fluids, which are viscoelastic fluids with approximately constant viscosity.

Polymer solutions generally have shear-thinning properties. Different from concentrated polymer solutions, the variation of viscosity with shear rate for Boger fluids, or dilute polymer solutions, is very small or negligible. According to James (2009), another important characteristic of Boger fluids that elastic effects can be separated from viscous effects.

Different models are proposed to predict the viscosity of dilute polymer solutions. For example, the Carreau-Yasuda viscosity model (Yasuda et al., 1981) is given by

$$\eta = \eta_\infty + \frac{\eta_o - \eta_\infty}{[1 + \lambda_{CY}\dot{\gamma}^a]^{n/a}} \tag{8.2}$$

where a is a fitting parameter introduced by Yasuda et al. (1981), n is a power law index, and λ_{CY} is a parameter representing the inverse shear rate at the onset of shear-thinning behavior. η_o and η_∞ are the viscosity at zero shear rate and infinite shear rate. Corresponding values are presented in Table 8.1 and these parameters are generally determined empirically from experimental data from testing using present A.P. rheometer. Also include are ρ_d, k_f and c_p, which are the density, conductivity and specific heat of the liquids.

8.2.2 Testing procedures

Viscosity values for shear rates from 0.1 1/s to 100 1/s are determined using the setting interface shown in Figure 8.8 and RheoCompass Software to remotely control the MCR. The software program, Flow Curve Steady State 1, is applied to determine the overall viscosity. The number of data points and shear rate are set under the Measurement

tab. All setting information is shown in Figure 8.8. With the setting shown, 25 data points are tested over a shear rate range of 0.1 1/s to 100 1/s. The duration time for one data point is adjusted by the device automatically. The results are displayed using a logarithmic profile.

The step-by-step procedure is as follows.

Test preparation steps follow.

a. Turn on Rheometer and turn the air supply switch to the vertical direction. After the Rheometer is fully operational, open control panel from RheoCompass™ software by double left-clicking the icon on the desktop and initialize the rheometer by clicking the initialize button. Note that the measurement bob is unattached here.

b. Attach the measurement bob to the top part of rheometer. The bob should be cleaned and dried each time before the attachment.

c. Set the testing parameters using RheoCompass™ control panel by left-clicking the MCR 302 SN83277960 tab, so the temperature is 20 ºC, measurement distance is 1 mm, and the original distance is 60 mm.

d. Fill the testing cup with sample solution to the marker inside the cup and insert the testing cup into the chamber. Make certain that there no vapor bubbles are present during the insertion.

e. Lower measurement bob to 1 mm using the control panel and wait until the temperature, is equilibrium at 20 ºC.

Test procedure steps follow.

f. Open software program, Flow Curve, Steady State 1, from the application tab and click on the Measurement viscosity curve tab, which measures the viscosity in

variation with shear rate. Under the shear rheological measurement tab, change the point number, which is the number of data points obtained, from 18 to 25. Change the shear rate range from 0.1 1/s to 100 1/s and the profile is Ramp logarithmic.

g. Click on the Start tab, name test using the date and testing properly and start the testing by click on the Start. The output data is in the form of an EXCEL file, as shown in Figure 8.9.

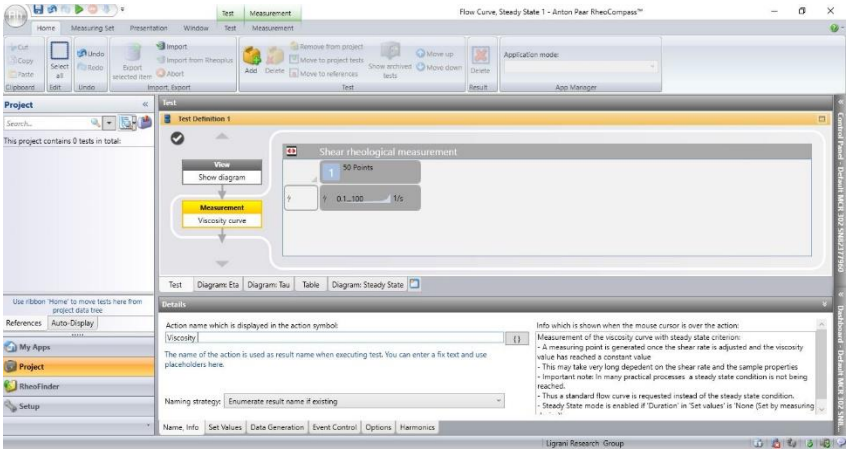

(a)

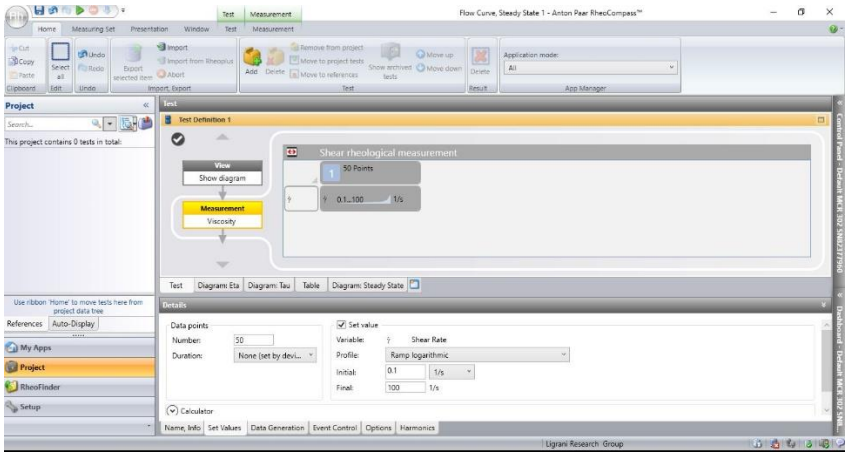

(b)

Figure 8.8 Anton-Paar 92002 MCR 302 Modular Compact Rheometer controlpanel for setting interface for overall viscosity testing.

test date	4/27/2018					
Point No.	Measuring Point Duration	Shear Rate	Shear Stress	Viscosity	Torque	Status
	Constant component	Constant component				
	[s]	[1/s]	[Pa]	[mPa·s]	[mN·m]	
1	120	0.00999	0.003914	391.59	0.00020774	Dy_auto
2	144	0.0147	0.0059325	404.25	0.00031488	Dy_auto
3	72	0.0216	0.0093121	431.95	0.00049425	Dy_auto
4	224	0.0316	0.010282	325.1	0.00054573	Dy_auto
5	32	0.0464	0.01374	296.06	0.00072929	Dy_auto
6	24	0.0681	0.01961	287.9	0.0010408	Dy_auto
7	24	0.1	0.02872	287.17	0.0015244	Dy_auto
8	48	0.147	0.037118	252.87	0.0019701	Dy_auto
9	32	0.215	0.054962	255.09	0.0029172	Dy_auto
10	16	0.316	0.078196	247.24	0.0041504	Dy_auto
11	32	0.464	0.11109	239.32	0.0058963	Dy_auto
12	16	0.681	0.16023	235.15	0.0085047	Dy_auto
13	40	1	0.22818	228.17	0.012111	Dy_auto
14	40	1.47	0.39862	271.56	0.021157	Dy_auto
15	88	2.15	0.48846	226.72	0.025926	Dy_auto
16	16	3.16	0.72924	230.58	0.038705	Dy_auto
17	128	4.64	1.0412	224.31	0.055262	Dy_auto
18	144	6.81	1.5069	221.18	0.079983	Dy_auto
19	24	10	2.1547	215.45	0.11436	Dy_auto
20	120	14.7	3.136	213.65	0.16645	Dy_auto
21	16	21.5	4.5574	211.51	0.24189	Dy_auto
22	24	31.6	6.6015	208.74	0.35038	Dy_auto
23	32	46.4	9.6747	208.42	0.5135	Dy_auto
24	16	68.1	14.223	208.75	0.75493	Dy_auto
25	40	100	20.624	206.23	1.0946	Dy_auto

Figure 8.9 Data file listing of output data for overall viscosity.

8.2.3 Results and discussion

Magnitudes of overall viscosity η from Anton-Parr rheometer analysis are presented in Figure 8.10 for different polymer concentrations. Viscosity values are presented for shear rates from 8 1/s to about 55.0 1/s. Here, magnitudes of overall viscosity increase with polymer concentration at each value of shear rate. In addition, values are approximately constant as shear rate varies, which is consistent with viscoelastic, Boger fluid behavior (James, 2009) for ρ values of 80, 100, 150, and 300 ppm. A similar trend is evidenced by the sucrose solvent solution, with a ρ value of 0 ppm, which is consistent with Newtonian fluid behavior. Experimental rheometer data for all magnitudes of polymer concentration and shear rate is also in agreement with values

determined using the Carreau-Yasuda viscosity model (Yasuda et al., 1981), given by equation (8.2), where associated parameter values are given in Table 8.1.

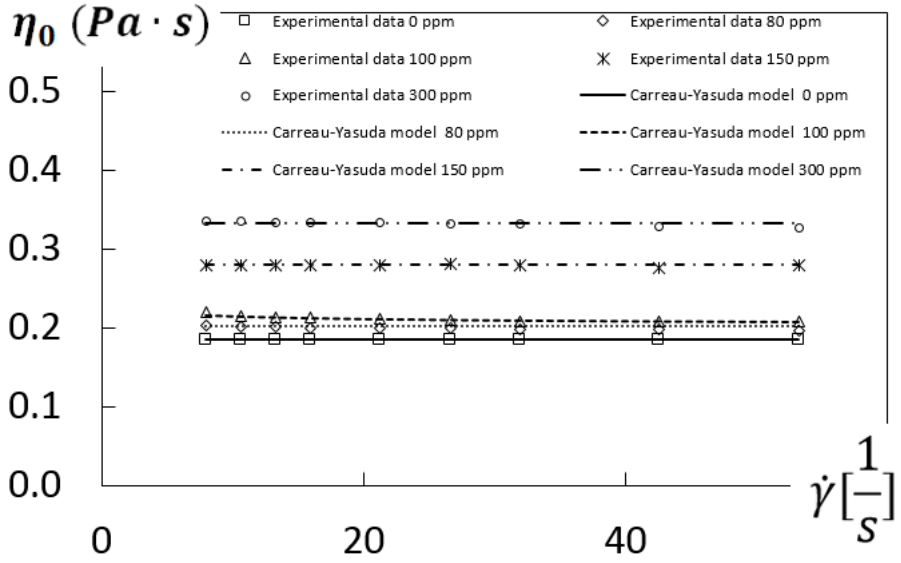

Figure 8.10 Overall viscosity variation with shear rate from experimental rheometer testing, compared to values determined using the Carreau-Yasuda analytic model (Yasuda et al., 1981).

Table 8.1 Rheological properties of the polymer solutions.

ρ (ppm)	0	80	100	150	300
ρ_d (kg/m^3)	1311	1315	1315	1315	1316
k_f (W/m·K)	0.368	0.368	0.368	0.368	0.368
c_p (J/kg·K)	2600	2600	2600	2600	2600
η_0 (Pa·s)	0.187	0.209	0.228	0.297	0.439
η_∞ (Pa·s)	-	0.200	0.210	0.270	0.260
a	-	0.150	0.300	0.460	0.500
n	-	0.421	0.564	0.305	0.310
λ_{CY}	-	0.546	0.490	0.655	0.230

8.3. Relaxation Time Determination

8.3.1 Theoretical background

Relaxation time, λ, is an observable time scale, which is an important characteristic of polymer solutions. Relaxation time is related to the elastic energy

absorbed by the polymer solution, depending on the relaxation process within and outside the polymer chain (Del Giudice et al., 2017). Relaxation time is associated with large scale microscopic motions, which are generally associated with the elastic character of the polymer solutions (Sunthar, 2009). Relaxation time depends on the relaxation process within and outside the polymer chain. The relaxation process occurs from multiple processes related to the entire polymer chain, including the polymer subchains (Del Giudice et al., 2017). When the equilibrium state of a polymer microstructure is deformed, the chain tends to back to the equilibrium state through the elastic energy stored during the deformation process. As polymer solutions are not ideal elastic material, dissipative processes also occur at the same time. For the small deformations, system response are often considered linear. Linear viscoelastic behavior allows determination of the relaxation time using the frequency sweep method, however, the determination of the relaxation time is generally challenging for dilute polymer solutions.

The characteristic relaxation time, or maximum relaxation is determined by testing the cross-over points of angular frequency of the storage modulus and the loss modules (Bohme, 1987). G' is the storage component and represents the elastic modulus. G'' is the loss component, and represents the viscous modulus. The characteristic relaxation time is the inverse of the angular frequency at the point where G' and G' are equal, as given by

$$\lambda = \frac{G'}{G''\omega} \tag{8.3}$$

where ω is cross-over the angular frequency (Sunthar, 2009).

The Zimm theoretical model describes the relaxation time analytically for lower polymer concentrations below the concentration that polymer coils start to interact with

each other (Del Giudice, 2017). The Zimm model relaxation time (Zimm, 1956) is given by

$$\lambda = \frac{F \times [\eta] \times M_w \times \eta_s}{RT} \tag{8.4}$$

where F is a parameter which depends on the quality of the solvent, [η] is intrinsic viscosity, M_w is molecular weight, R is universal gas constant, T is absolute temperature, and η_s is the solvent viscosity, which is a constant independent of shear rate. With the present solutions, the value of F is approximately 0.5313. In Table 8.2 and Table 8.3, η_0 is viscosity at zero shear rate, and η_r equals η_0/η_s.

The intrinsic viscosity [η] is determined based on a theoretical models from Del Giudice et al. (2017). Note that viscosity varies with polymer concentration. With dilute polymers, Del Giudice et al. (2017) indicates that the specific viscosity at zero shear rate η_{sp0} is given by

$$\eta_{sp0} = \rho \times [\eta] \tag{8.5}$$

This quantity is also expressed using:

$$\eta_{sp0} = \frac{\eta_0 - \eta_s}{\eta_s} \tag{8.6}$$

Within these equations, ρ is the concentration of the polymer solution, $[\eta]$ is the intrinsic viscosity, and η_0 and η_s are the zero-shear rate viscosity and solvent viscosity, respectively. Solvent viscosity for 65 percent of sucrose solution within the present study is 0.185 Pa·s. The zero shear rate viscosity is determined based on Carreau-Yasuda viscosity model (Yasuda et al., 1981). Associated parameters are given in Table 2. The Soloman-Ciuta equation (Pamies et al., 2008) is also used to predict the intrinsic viscosity, and the relaxation time. Associated parameters are given in Table 8.3. Note that

the relaxation times given in Table 8.2 and Table 8.3 are in approximate agreement with each other, especially for lower concentrations.

Table 8.2 Rheological properties of polymer solutions for different concentrations from Del Giudice, et al. (2017).

ρ	η_o	η_{sp0}	$[\eta]$	λ
ppm	Pa·s	Pa·s	Pa·s	s
80	0.209	0.130	1.622	1.177
100	0.228	0.232	2.324	1.687
150	0.297	0.605	4.036	2.930
300	0.439	1.373	4.577	3.322

Table 8.3 Rheological properties of polymer solutions for different concentrations from Solomon-Ciuta equation (Pamies, et al., 2008).

ρ	η_o	η_r	$[\eta]$	λ
ppm	Pa·s	Pa·s	Pa·s	s
80	0.209	1.130	1.556	1.130
100	0.228	1.232	2.165	1.572
150	0.297	1.568	3.239	2.351
300	0.439	2.373	3.363	2.441

8.3.2 Testing procedures

Testing preparation steps are similar to the ones used for viscosity determination. The program, Frequency Sweep with auto LVER, is applied using 25 data points and 10% final strain setting. The rheometer interface is shown in Figure 8.11. Output data includes the storage modulus and loss modulus as they vary with angular frequency. The cross-over value is associated with the cross-over frequency where the storage and loss modules are the same.

The step-by-step procedure as follows.

Test preparation steps follow.

a. Turn on Rheometer and turn the air supply switch to the vertical direction. After the Rheometer is fully operational, open control panel from RheoCompass™ software by double left-clicking the icon on the desktop and initialize the rheometer by clicking the initialize button. Note that the measurement bob is unattached here.

b. Attach the measurement bob to the top part of rheometer. The bob should be cleaned and dried each time before the attachment.

c. Set the testing parameters using RheoCompass™ control panel by left-clicking the MCR 302 SN83277960 tab, so the temperature is 20 ºC, measurement distance is 1 mm, and the original distance is 60 mm.

d. Fill the testing cup with sample solution to the marker inside the cup and insert the testing cup into the chamber. Make certain that there no vapor bubbles are present during the insertion.

e. Lower measurement bob to 1 mm using the control panel and wait until the temperature, is equilibrium at 20 ºC.

Test procedure steps follow.

f. Open software program, Frequency Sweep with auto LVER, from the application tab and open the Amplitude Sweep section. This section is to set the amplitude of the frequency sweep. Under the shear rheological measurement tab, change the first value, the point number, from 13 to 25, the final strain from 1 to 10% and angular frequency from 10 to 1 rad/s.

g. Open Frequency Sweep section. During the frequency sweep the frequency is varied while the amplitude of the deformation is kept constant. For the analysis the storage and loss modulus are plotted against the frequency. The data at low

frequencies describe the behavior of the samples at slow changes of stress. Change number of points, which is the data points you want to record from 16 to 25 and initial angular frequency from 100 to 10 rad/s.

h. Click on the Start tab, name test using the date and testing properly, start the testing, the output is the storage and loss module values.

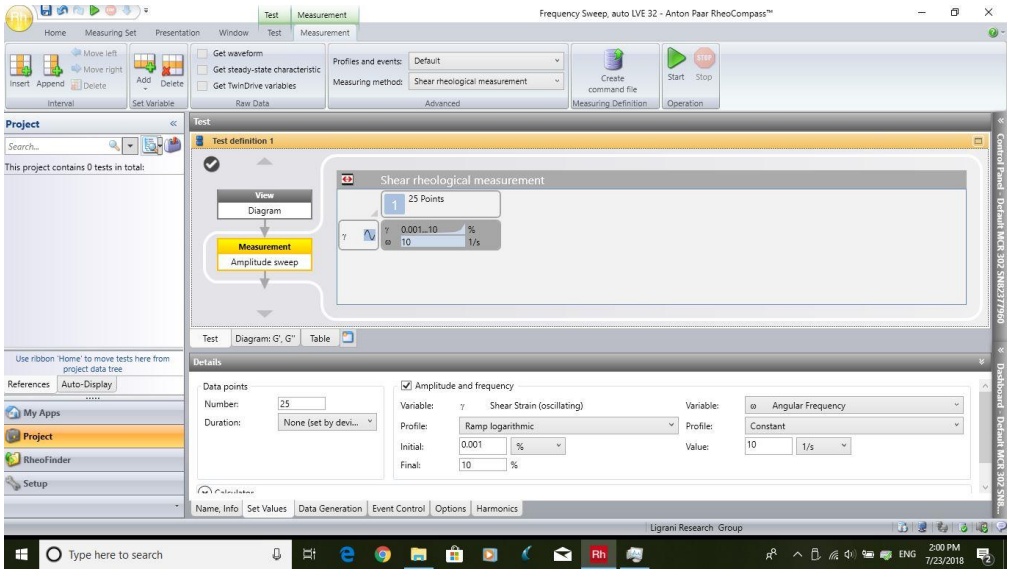

Figure 8.11 Anton-Paar 92002 MCR 302 Modular Compact Rheometer control panel for relaxation time setting.

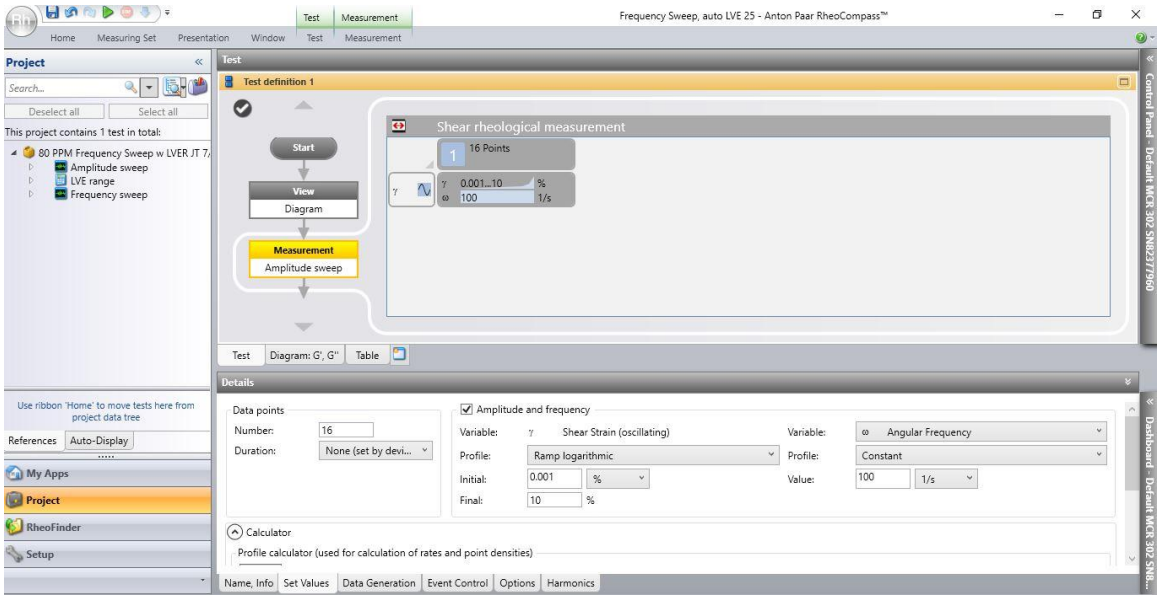

Figure 8.12 Anton-Paar 92002 MCR 302 Modular Compact Rheometer control panel for separation of elastic and viscous modulus setting.

8.3.3 Results and discussion

The relaxation time is determined theoretically using Zimm equation (Zimm, 1956; De Gennes, 2017). For dilute polymers used in current investigation, the magnitude of G' is substantially lower than the magnitude of G'' as frequency varies. Therefore, no cross-over point is achieved experimentally due to the low concentration of polymers.

8.4. Procedures for Separation of Elastic and Viscous Modulus Values

8.4.1 Theoretical background

In the dilute polymer solution, the polymer coils are believed to have sufficient space without contacting and interacting with each other. Therefore, the viscoelasticity depends on the behavior of individual polymer coils. In dilute polymer solutions, the magnitude of G'' is always larger than the magnitude of G' as frequency varies. This is believed to be because the polymer chains are able to slip past one another due to the sufficient space and time. This means that there is no tension caused between chain

segments due to the coupling and interaction of different species, which enhances the elastic modulus. With no sufficient interactions between polymer chains, the viscosity is approximately constant for dilute polymer solutions, even when the chains attain maximum length (Rao, M.A.,1999; Sunthar,2009; James, 2009).

The elastic or storage modulus and the viscous or loss modulus are expressed using

$$G' = \frac{\tau_0'}{\gamma_0} \tag{8.7}$$

and

$$G'' = \frac{\tau_0''}{\gamma_0} \tag{8.8}$$

respectively. Within theses equations, γ_0 is the preset strain, which is 5% for the current investigation, and τ_0' and τ_0'' are stress values related to the respective moduli. Complex viscosity is then composed of a viscous portion and an elastic portion, as given by

$$\eta'' = \frac{\tau_0''}{\gamma_0} = \frac{G''}{\omega} \tag{8.9}$$

and

$$\eta' = \frac{\tau_0'}{\gamma_0} = \frac{G'}{\omega} \tag{8.10}$$

respectively. The overall magnitude of the absolute value of the complex viscosity, η^* is then determined using

$$|\eta^*| = (\eta'^2 + \eta''^2)^{1/2} \tag{8.11}$$

8.4.2 Testing procedures

The software program, Frequency Sweep with auto LVER, is again used to separate the viscous and elastic modulus values. 16 data points and frequency range from

0.1 to 100 1/s are set. A larger frequency range is chosen compared to the frequency range in the relaxation time testing. An example of output data in the form of an EXCEL FILE is shown in Figure 8.12.

The step-by-step procedure is as follows.

Test preparation steps follows.

a. Turn on Rheometer and turn the air supply switch to the vertical direction. After the Rheometer is fully operational, open control panel from RheoCompass™ software by double left-clicking the icon on the desktop and initialize the rheometer by clicking the initialize button. Note that the measurement bob is unattached here.

b. Attach the measurement bob to the top part of rheometer. The bob should be cleaned and dried each time before the attachment.

c. Set the testing parameters using RheoCompass™ control panel by left-clicking the MCR 302 SN83277960 tab, so the temperature is 20 ºC, measurement distance is 1 mm, and the original distance is 60 mm.

d. Fill the testing cup with sample solution to the marker inside the cup and insert the testing cup into the chamber. Make certain that there no vapor bubbles are present during the insertion.

e. Lower measurement bob to 1 mm using the control panel and wait until the temperature, is equilibrium at 20 ºC.

Test procedure steps follow.

f. Open software program, Frequency Sweep with auto LVER, from the application tab and open the Amplitude Sweep section. This section is to set the amplitude of the frequency sweep. Under the shear rheological measurement tab, change the first

value, the point number, from 13 to 16, the final strain from 1 to 10% and angular frequency from 10 to 100 rad/s.

g. Open Frequency Sweep section. During the frequency sweep the frequency is varied while the amplitude of the deformation is kept constant. For the analysis the storage and loss modulus are plotted against the frequency. The data at low frequencies describe the behavior of the samples at slow changes of stress. Change number of points, which is the data points you want to record to 16 and initial angular frequency from 100 rad/s.

h. Click on the Start tab, name test using the date and testing time, start the testing, the output is the storage and loss module values, as shown in Figure 8.13.

Point No.	Angular Frequency	Storage Modulus	Loss Modulus	Loss Factor	Shear Strain	Shear Stress	Torque	Status
		G'	G"					
	[rad/s]	[Pa]	[Pa]	[1]	[%]	[Pa]	[mN·m]	
1	100	0.0011188	22.375	20000	0.1	0.022383	0.001188	ME-,taD,TruStrain™
2	63.1	0.00063267	12.653	20000	0.159	0.02006	0.0010647	ME-,taD,TruStrain™
3	39.8	0.00034649	6.9298	20000	0.252	0.017435	0.0009254	ME-,taD,TruStrain™
4	25.1	0.00020394	4.0787	20000	0.399	0.016275	0.00086381	ME-,taD,TruStrain™
5	15.8	0.00012533	2.5066	20000	0.63	0.015796	0.00083838	ME-,taD,TruStrain™
6	10	7.88E-05	1.5756	20000	1	0.015764	0.00083672	ME-,taD,TruStrain™
7	6.31	4.96E-05	0.99241	20000	1.58	0.015688	0.00083265	ME-,taD,TruStrain™
8	3.98	0.00049149	0.62808	1277.911	2.52	0.015811	0.00083919	TruStrain™
9	2.51	0.00611	0.40247	65.871	3.98	0.016029	0.00085075	WMa,TruStrain™
10	1.58	0.0052481	0.25524	48.635	6.29	0.016048	0.00085176	WMa,TruStrain™
11	1	0.0037081	0.16272	43.883	10.1	0.016431	0.0008721	WMa,TruStrain™
12	0.631	0.0027372	0.10396	37.981	15.7	0.016365	0.00086861	WMa,TruStrain™
13	0.398	0.0013597	0.065873	48.445	25.1	0.016538	0.0008778	WMa,TruStrain™
14	0.251	0.00068121	0.041745	61.281	39.8	0.016633	0.00088284	WMa,TruStrain™
15	0.158	0.000311	0.026436	85.002	63.3	0.016734	0.00088819	WMa,TruStrain™
16	0.1	0.00012195	0.016713	137.043	101	0.016813	0.00089239	WMa,TruStrain™

Figure 8.13 Data file listing of storage modulus and loss modulus variation with angular frequency; angular frequency refers to the oscillating frequency for the amplitude frequency test.

8.4.3 Results and discussion

Values of elastic modulus and viscous modulus both vary with frequency for different polymer concentrations. Associated data are shown in Figures 8.14 (a)-(e). The frequency range for these data is from 0.1 to 100 rad/s for a temperature of 20°C. Figures

8.14 (a)-(e) show that the loss or viscous modulus values cover approximately the same range of values for all polymer concentrations. The elastic or storage modulus show a much smaller magnitude of value for each frequency, because the amount of polymer mass is only 0.008 percent (or $\frac{8}{1000}$ of one present) to 0.03 percent (or $\frac{3}{100}$ of one present) of the total mass. The elastic or storage modulus generally increases with increasing frequency, with a sharp decrease as frequency increases above 1 to 8 radians per second.

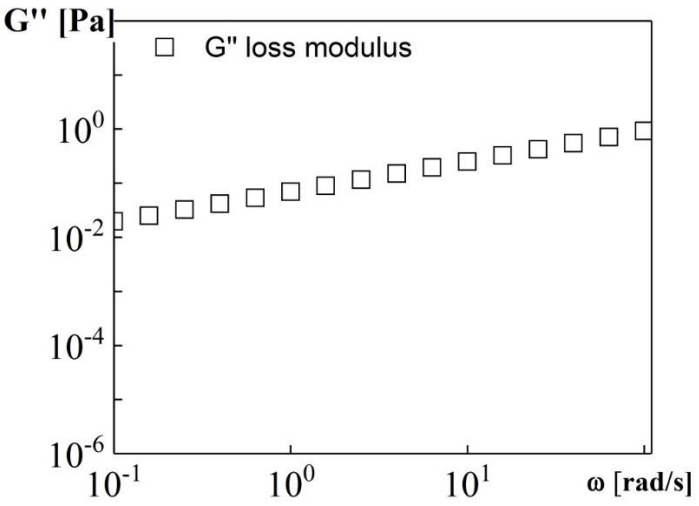
G'' [Pa]
G'' loss modulus
10^0
10^-2
10^-4
10^-6
10^-1
10^0
10^1
ω [rad/s]

(a)

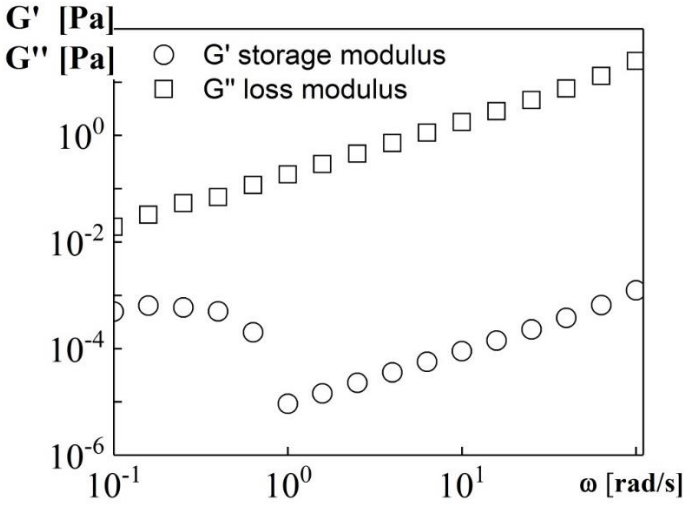
G' [Pa]
G'' [Pa]
G' storage modulus
G'' loss modulus
10^0
10^-2
10^-4
10^-6
10^-1
10^0
10^1
ω [rad/s]

(b)

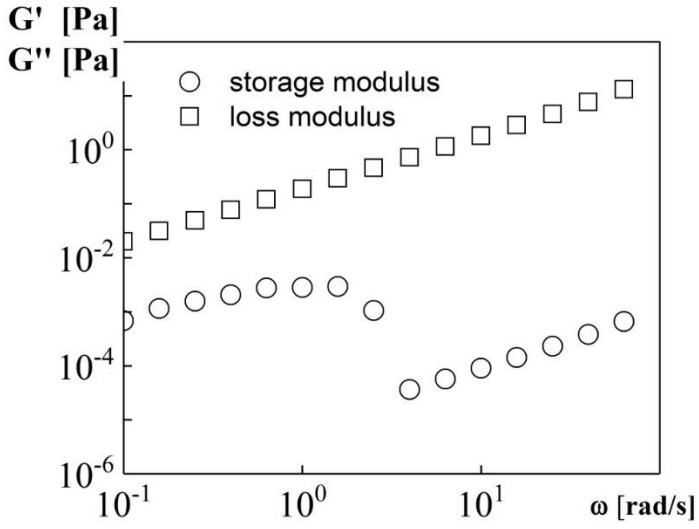
G' [Pa]
G'' [Pa]
storage modulus
loss modulus
10^0
10^-2
10^-4
10^-6
10^-1
10^0
10^1
ω [rad/s]

(c)

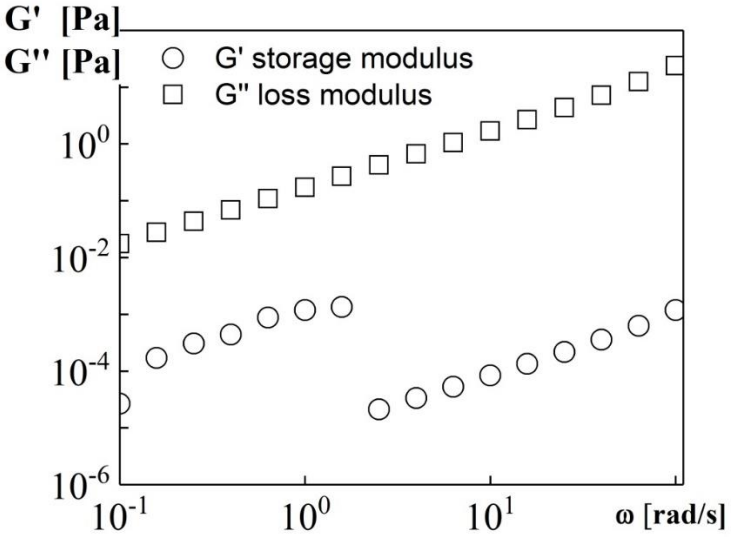
G' [Pa]
G'' [Pa]
G' storage modulus
G'' loss modulus
10^0
10^-2
10^-4
10^-6
10^-1
10^0
10^1
ω [rad/s]

(d)

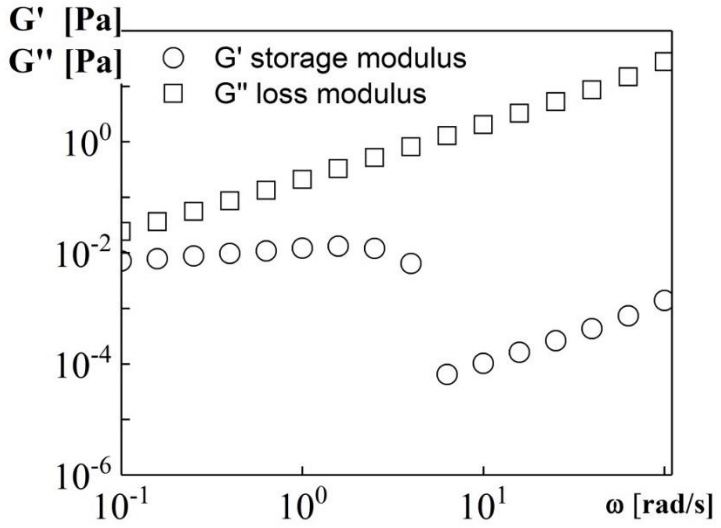

\

(e)

Figure 8.14 Loss modulus values and storage modulus values as they vary with angular frequency for: (a) 0 ppm (b) 80 ppm (c) 100 ppm (d) 150 ppm (e) 300 ppm.

CHAPTER 9

SUMMARY AND CONCLUSIONS

The present investigation considers thermal transport variations from the presence of elastic instabilities within internal flows. A miniature Viscous Disk Pump (VDP) and a Couette Rotating Flow (RCF) environment are utilized to investigate flow and heat transfer characteristics for very low Reynolds numbers.

The viscous disk pump heat transfer results are based upon energy balance measurements which utilize the mixed-mean temperature at the inlet and outlet of the VDP flow passage. The overall heat transfer rate is determined based upon a constant surface temperature thermal boundary condition, and upon a log-mean-temperature difference approach. The VDP operates at rotation speeds of 500 RPM, 1000 RPM, 1500 RPM, 1800 RPM, and 2000 RPM (or 52.36 radians/s, 104.7 radians/s, 157.1 radians/s, 188.5 radians/s, and 209.4 radians/s, respectively), which produce overall shear rates across the flow cross section of 146.05 1/s, 292.1 1/s, 438.1 1/s, 525.8 1/s, and 584.2 1/s. A channel depth of 640 μm is employed. Elastic turbulence is induced by adding polyacrylamide to water solutions with 65 % sucrose by mass.

Significant enhancements of mixing and transport are observed, which are associated with the onset and development of elastic instabilities. Such behavior is

verified, relative to Newtonian Boger fluid solvents, using flow visualization results, pressure rise data, overall shear stress variations, increases of overall magnitudes of convective Nusselt numbers, increases of time-averaged magnitudes of mean-square temperature fluctuations, and increases of spectral energy content of unsteady temperature fluctuations. Note that the enhancements observed are not due to increased viscosity values alone, because the natural tendency of increased viscosity (with or without polymers present) is suppression of flow fluctuations and local chaotic fluid motions. Increases of viscosity values associated with the polymer solutions, relative to Boger fluids, are not sufficient to induce the observed Nusselt number augmentations (even though such increases result in enhanced molecular transport). In addition, centrifugal instabilities associated with streamline curvature are not responsible for the observed variations, because associated Dean numbers are not large enough, or the streamwise extent of streamline curvature is not extensive enough, to allow development of the associated centrifugal-instability induced secondary flows. In addition, the experimental conditions associated with elastic instability transition cannot be characterized by one Dean number, and associated centrifugal instabilities (and associated Dean numbers) do not vary with polymer concentration.

Results associated with RCF are presented which demonstrate the remarkable ability of viscoelastic fluids to augment surface heat transfer characteristics. With this flow arrangement, the overall heat transfer rate is determined based upon a constant surface heat flux thermal boundary condition. Associated magnitudes of surface Nusselt number enhancement are determined for sucrose-based, viscoelastic solutions with polyacrylamide, relative to: (a) sucrose solvent flows, and (b) viscoelastic, Boger solution

flows. Included are Nusselt number variations, flow visualization results, spectral analysis of flow static temperature fluctuations, and consideration of the onset and development of elastic instabilities.

Flow visualization results and Nusselt number data show that the onset of what is believed to be elastic instabilities is well represented using a constant Weissenberg number criterion, given by

$$Wi=30$$

Variations of normalized and time-averaged magnitudes of the mean-square of flow static temperature fluctuations are also consistent with this criterion, since those values also increase substantially as Weissenberg number becomes greater than 30. Power spectral distributions of static temperature fluctuations, for the highest polymer concentrations and highest disk rotation speeds and the same experimental conditions, show broad-band characteristics, with continuous power content present at frequencies from just greater than 0.01 Hz to values of approximately 1 Hz. These spectral distributions are as much as three orders of magnitude higher than distributions which are associated either with the sucrose solvent flow, where $\rho=0$ ppm, or when no rotation is present and $\omega=0$ rad/s.

Associated elastic instability onset Nusselt number ratios (determined as the ratio of Nusselt number for sucrose-based, viscoelastic solutions with polyacrylamide, relative to Nusselt numbers for sucrose solvent flows) are equal to 1.42 to 1.58. The criterion for the onset of elastic instabilities, given by Wi=30, also provides a more physically realistic model for the present flow configuration, compared to criteria based upon either constant Reynolds number, constant Graetz number, or constant McKinley et al. transition parameter (McKinley et al., 1996). Magnitudes of Nusselt number enhancement,

associated with increased polymer concentration and increased shear rate, are as high as 3.0, compared to zero shear rate values (obtained with zero rotation), which are in the vicinity of 1.0. Note that enhancement ratios are even higher, relative to conditions associated with viscoelastic, Boger solution flows (or stable viscoelastic flows), when compared at the same polymer concentration.

APPENDIX A

Thermocouple Response Time

Temperature measurements uses Omega 5TC-TT-T-40-72 fine-wire copper-constantan (Type T) thermocouples. Thermocouple response time and response frequency are 0.0022 sec and 455 Hz, respectively, which are determined using the lumped heat capacitance method as given by Eqn. (a1).

$$\frac{T-T_\infty}{T_i-T_\infty} = exp\left[-\left(\frac{hA}{\rho Vc}\right)t\right] = exp\left[-\left(\frac{6h}{\rho Dc}\right)t\right] \quad \text{(a1)}$$

Here, t is response time, T_∞ is fluid temperature, T_i is initial temperature, D is thermocouple conjunction diameter, c is specific heat of solid, ρ is density of solid, V is volume, A is surface area, and h is heat transfer coefficient. To reach 63% of an instantaneous temperature change, response time data from the lumped heat capacitance method and from the thermocouple manufacturer are given in Table A1.

Table A1. Thermocouple response time and frequency

	Lumped heat capacitance method	Omega Corp.
Response time [s]	0.0038	0.003
Response frequency [Hz]	263	334

APPENDIX B

Relaxation Times for High Polymer Concentrations

Fluid relaxation time for high polymer concentrations, with viscosity values larger than 1000 mPa·s, can be obtained by fitting the stress relaxation data using the viscoelastic model expressed using

$$G(t) = G_0 e^{-\frac{t}{\lambda}} \tag{B1}$$

Here, t is time, G(t) is fluid shear modulus, G_0 is fluid shear modulus at t=0, and λ is longest fluid relaxation time (Pan et al., 2013).

To obtain the appropriate data, the software program of Anton-Paar 92002 MCR 302 Modular Compact Rheometer, Shear Strain, is used to measure fluid shear modulus as it varies with time. The longest relaxation time λ is then determined from output data provided by Eqn. B1, where

$$\lambda = -\frac{1}{n}$$

and n is the power law index.

Example data for carboxy-methyl-cellulose fluids are given in Table B1 and Figure B1 from Pan et al. (2013).

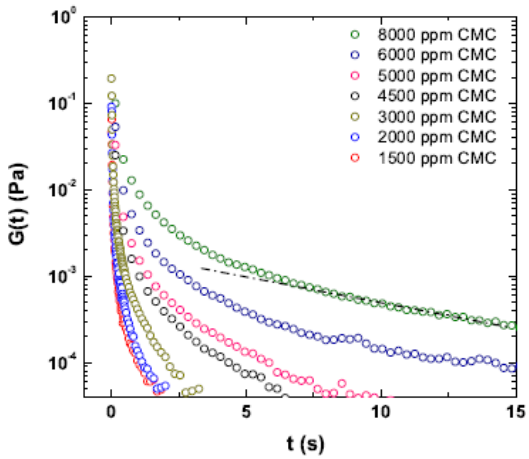

Figure B1: Stress relaxation data for carboxy-methyl-cellulose fluids (Pan et al., 2013).

Table B1: Relaxation time data for carboxy-methyl-cellulose fluids (Pan et al., 2013).

c (ppm)	n
1500	0.83
2000	0.81
3000	0.80
4500	0.76
5000	0.74
6000	0.70
8000	0.65

APPENDIX C

Software Directory

A listing of software by filename, with a brief description for each of the different software used in this dissertation.

Software Directory-Viscous Disk Pump

Software	Folder Name	File Name	Description
Lab View	Lab View Programs /Pressure Transducer	Motor Control.vi	Used to control the motor rotation
		Pressure measurement.vi	Used to collect and store pressure data from pressure transducers for Viscous Disk Pump
		Pressure_Transducer_Calibration.vi	Used to calibrate pressure transducer
	Lab View Programs /Thermocouple	Temperature Fluctuations VDP.vi	Used to collect and store temperature fluctuations data from thermocouples for Viscous Disk Pump
		Thermocouple Calibration.vi	Used to calibrate thermocouples
Lab View		._FloatingAvg.vi*	Used to control the motor rotation
		._Motor Control (1).vi*	
		._Pressure_Transducer_Calibration (1).vi*	Used to calibrate pressure transducer
		._Thermocouple_Calibration (1).vi*	Used to calibrate thermocouples
		._VDP_Data_Acq (1).vi*	Used to collect and store pressure data from pressure transducers for Viscous Disk Pump Used to calibrate pressure transducer
		._VDP_Data_Acq_Avg.vi*	
		._VDP_Data_Acq_Export.vi*	

*Old Version

Software Directory-Rotating Couette Flow

Software	Folder Name	File Name	Description
Lab View	Lab View	Temperature Fluctuations Measurement.vi	Used to collect and store temperature fluctuations data from thermocouples for Rotating Couette Flow
		Thermocouple_Calibration.vi	Used to calibrate thermocouples
Excel	Lab View	TC calibrations 1-11-2017.xlsx	Thermocouple calibration result
Matlab	Matlab	Concentration_profile_PDF.m	Used to plot concertation profiles for Rotating Couette Flow based on Partial Differential Equation approach
		grayscale_read.m	Used to determine gray scale at different points for Rotating Couette Flow
		Heat_Transfer_Calculation.m	Used to calculate the heat transfer coefficients, Nu values as well as mean temperature fluctuations
		RCFD_Temperature_Spectra.m	Used to plot power spectra using thermocouple data from LabView output for Rotating Couette Flow
OriginLab	OriginLab	0 ppm.opj	Origin Lab program to generate plots
		40 RPM.opj	
		300 ppm.opj	
Solid Edge	Thermocouple Location	Assembly1 Side View.dft	Rotating Couette Flow configuration
		Assembly1.asm	
		Assembly1.cfg	
		thermocouple location.dft	Thermocouple location

APPENDIX D

Data File Directory

A listing of data files by filenames, these data files include data for the results presented in this dissertation.

Folder Name	Configuration	Data File Name	Description
Chapter2 and Chapter 3	Viscous Disk Pump	VDP figure 2.1-2.5.pptx	Configurations of VDP
		figure 2.6.pptx	Thermocouple location figures
		shear stress Fig. 3.6.xlsx	Process data for shear rate and shear stress
		pressure rise Figure 3.4 3.5.xlsx	Process data for pressure rise
		diffusion speed Figure 3.2.xlsx	Process data for diffusion rate with flow rate
		transition plot Figure 3.3.xlsx	Process data associated with elastic instability onset
		VDP Time Sequence 100ppm figure 3.1b.docx	Record data for flow images
		VDP Time Sequence sucrose figure 3.1a. docx	
		Power_spectra 3.11.m	Process data for power spectra
		fft for VDP figure 3.11.jpj	Power spectra of temperature fluctuations
		VDP Heat Transfer 500RPM.xlsx	Temperature recorded at the outlet

		VDP Heat Transfer 1000RPM.xlsx	
		VDP Heat Transfer 1500RPM.xlsx	
		VDP Heat Transfer 2000RPM.xlsx	
Chapter 4	Rotating Couette Flow	Configuration 4.3-4.7.pptx	Configurations of Rotating Couette Flow
		Photograph 4,1 4.2 4.5.docx	Photographs of Rotating Couette Flow
		Fluid properties Table 4.1 4.2.xlsx	Solution physical and rheological properties
Chapter 5	Rotating Couette Flow	visualization Fig 5.1a.docx visualization Fig. 5.1b.docx	Data associated with flow visualization images.
		40 RPM spectra Fig 5.9a.jpg 300 ppm spectra Fig. 5.9b.jpg	Temperature fluctuations power spectra results
		viscosity Fig 5.5.xlsx	Process data associated with rheological properties
		dimensionless Nu_Fig 5.7,10,11,12,14.xlsx	Process data associated with thermal transport.
		Nusselt number Fig. 5.6 5.15.xlsx	Process data associated with thermal transport.
		temperature fluctuations Fig. 5.8 5.13.xlsx	Process data associated with temperature fluctuations
		Fig. 5.2.pptx Fig. 5.4.pptx	Modified data plot for Figures 5.2 and 5.4
		g values Fig. 5.3.xlsx	Processed data associated with diffusion rate
		transition plot diffusion approach.xlsx	Process data associated with elastic instability onset using diffusion approach

		transition plot McKinley approach.xlsx	Process data associated with elastic instability onset using McKinley approach
		RCF_Temperature_Spectra.m	Process data associated with thermal transport
Chapter 7		area derivative approach Fig 7.5 7.6.xlsx	Process data to determine effective diffusion coefficient using area derivative approach.
		0 ppm -5 mm analysis data Fig 7.8.xlsx	Process data to determine effective diffusion coefficient using PDE approach.
		100 ppm -5 mm analysis data Fig 7.8.xlsx	
		300 ppm -5 mm analysis data Fig 7.8.xlsx	
		transition plot Fig 7.12 7.15.xlsx	Process data associated with elastic instability
		diffusion coefficient Fig 7.7-7.11.xlsx	Process data associated with diffusion rate
		g values Fig. 7.13-14.xlsx	Transition based on g
		0 ppm 40 RPM.docx	Visualization images recorded at different conditions
		100 ppm 40 RPM.docx	
		300 ppm 40 RPM.docx	
Chapter 8		test name set.jpg	Start-up setting of MCR rheometer
		rheometer picture fig. 8.2.jpg	Photograph of MCR rheometer
		Relaxation time table 8.3.xlsx	Relaxation time determination
		rheometer testing chamber fig. 8.4.pptx	Testing chamber dimensions of MCR rheometer
		Measurement system fig. 8.5.jpg	Measurement system of MCR rheometer
		control panel fig. 8.7.jpg	Control panel of MCR rheometer
		viscosity setting fig8.8.jpg	Viscosity test setting using MCR rheometer
		Viscosity fig. 8.10.xlsx	Processed data

			associated with viscosity
		frequency sweep fig 8.11.jpg	Frequency sweep setting using MCR rheometer
		figure 8.12.jpg	
		MCR-manual book.pdf	MCR rheometer manual book
		80 PPM 0-100 Steady State JT 26 O.xlsx	Viscosity data obtained from MCR rheometer
		100 PPM 0-10 Steady State JT 59 O.xlsx	
		100 PPM 0-100 Steady State JT 57 O.xlsx	
		150 PPM 0-100 Average Steady State JT.xlsx	
		300 PPM Average.xlsx	
		Sucrose 0-100 Steady State JT.xlsx	

REFERENCES

Abed, W.M., Whalley, R.D., Dennis, D.J.C. and Poole, R.J., 2015, "Numerical and Experimental Investigation of Heat Transfer and Fluid Flow Characteristics in a Microscale Serpentine Channel," International Journal of Heat and Mass Transfer, Vol. 88, pp.790-802.

Abed, W.M., Whalley, R.D., Dennis, D.J.C. and Poole, R.J., 2016, "Experimental Investigation of the Impact of Elastic Turbulence on Heat Transfer in a Serpentine Channel," Journal of Non-Newtonian Fluid Mechanics, Vol. 231, pp.68-78.

Anton-Paar GmbH, 2016, "Instruction Manual MCR Series," Graz, Austria.

Arratia, P.E., Thomas, C.C., Diorio, J. and Gollub, J.P., 2006, "Elastic Instabilities of Polymer Solutions in Cross-Channel Flow," Physical Review Letters, Vol. 96(14), p.144502.

Balkovsky, E., Fouxon, A. and Lebedev, V., 2001, "Turbulence of Polymer Solutions," Physical Review E, Vol. 64(5), p.056301.

Berti, S. and Boffetta, G., 2010, "Elastic Waves and Transition to Elastic Turbulence in a Two-Dimensional Viscoelastic Kolmogorov Flow," Physical Review E, Vol. 82(3), p.036314.

Berti, S., Bistagnino, A., Boffetta, G., Celani, A. and Musacchio, S., 2008, "Two-Dimensional Elastic Turbulence," Physical Review E, Vol. 7(5), p.055306.

Bertola, V., Meulenbroek, B., Wagner, C., Storm, C., Morozov, A., van Saarloos, W. and Bonn, D., 2003, "Experimental Evidence for an Intrinsic Route to Polymer Melt Fracture Phenomena: A Nonlinear Instability of Viscoelastic Poiseuille Flow," Physical Review Letters, Vol. 90(11), p.114502.

Bonn, D., Ingremeau, F., Amarouchene, Y. and Kellay, H., 2011, "Large Velocity Fluctuations in Small-Reynolds-Number Pipe Flow of Polymer Solutions," Physical Review, Vol. 84(4), p.045301.

Burghelea, T., Segre, E. and Steinberg, V., 2007, "Elastic Turbulence in Von Karman Swirling Flow between Two Disks," Physics of Fluids, Vol. 19(5), p.053104.

Burghelea, T., Segre, E., Bar-Joseph, I., Groisman, A. and Steinberg, V., 2004, "Chaotic Flow and Efficient Mixing in a Microchannel with a Polymer Solution," Physical Review E, Vol. 69(6), p.066305.

Burnishev, Y. and Steinberg, V., 2014, "Torque and Pressure Fluctuations in Turbulent Von Karman Swirling Flow between Two Counter-Rotating Disks," Physics of Fluids, Vol. 26(5), p.055102.

Caruso, M.M., Davis, D.A., Shen, Q., Odom, S.A., Sottos, N.R., White, S.R. and Moore, J.S., 2009, "Mechanically-Induced Chemical Changes in Polymeric Materials," Chemical Reviews, Vol. 109(11), pp.5755-5798.

Chenyakin, Y., Ullmann, D.A., Evoy, E., Renbaum-Wolff, L., Kamal, S. and Bertram, A.K., 2017, "Diffusion Coefficients of Organic Molecules in Sucrose–Water Solutions and Comparison with Stokes–Einstein Predictions," Atmospheric Chemistry and Physics, Vol. 17(3), pp.2423-2435.

De Gennes, P.G., 1974, “Coil-Stretch Transition of Dilute Flexible Polymers under Ultrahigh Velocity Gradients,” Journal of Chemical Physics, Vol. 60(12), pp. 5030-5042.

Del Giudice, F., Haward, S.J. and Shen, A.Q., 2017, “Relaxation Time of Dilute Polymer Solutions: A Microfluidic Approach,” Journal of Rheology, Vol. 61(2), pp.327-337.

Duda, J.L., 1985, “Molecular Diffusion in Polymeric Systems,” Pure and Applied Chemistry, 57(11), pp.1681-1690.

Fouxon, A. and Lebedev, V., 2003, “Spectra of Turbulence in Dilute Polymer Solutions,” Physics of Fluids, Vol. 15(7), pp.2060-2072.

Gan, H.Y., Lam, Y.C. and Nguyen, N.T., 2006, “Polymer-based Device for Efficient Mixing of Viscoelastic Fluids,” Applied Physics Lletters, Vol. 88(22), p.224103.

Gan, H.Y., Lam, Y.C., Nguyen, N.T., Tam, K.C. and Yang, C., 2007, “Efficient Mixing of Viscoelastic Fluids in a Microchannel at low Reynolds Number,” Microfluidics and Nanofluidics, Vol. 3(1), pp.101-108.

Gerashchenko, S., Chevallard, C. and Steinberg, V., 2005, “Single Polymer Dynamics: Coil-Stretch Transition in a Random Flow,” Europhysics Letters, Vol. 71(2), p.221.

Groisman, A. and Steinberg, V., 1998, “Elastic vs. Inertial Instability in a Polymer Solution Flow,” Europhysics Letters, Vol. 43(2), p.165.

Groisman, A. and Steinberg, V., 1998, "Mechanism of Elastic Instability in Couette Flow of Polymer Solutions: Experiment," Physics of Fluids, Vol. 10(10), pp.2451-2463.

Groisman, A. and Steinberg, V., 2000, "Elastic Turbulence in a Polymer Solution Flow," Nature, Vol. 405(6782), p.53

Groisman, A. and Steinberg, V., 2001, "Efficient Mixing at Low Reynolds Numbers using Polymer Additives," Nature, 410(6831), p.905.

Groisman, A. and Steinberg, V., 2004, "Elastic Turbulence in Curvilinear Flows of Polymer Solutions," New Journal of Physics, Vol. 6(1), p.29.

Hartnett, J. P. and Kostic, M, 1985, "Heat Transfer to a Viscoelastic Fluid in Laminar Flow through a Rectangular Channel," International Journal of Heat and Mass Transfer, Vol. 28(6), pp. 1147-1155.

Hartnett, J.P., 1992, "Viscoelastic Fluids: A New Challenge in Heat Transfer," Journal of Heat Transfer (Transactions of ASME), Vol. 14, pp. 296-303.

James, D.F., 2009, "Boger Fluids," Annual Review of Fluid Mechanics, Vol. 41, pp.129-142.

Jun, Y. and Steinberg, V., 2009, "Power and Pressure Fluctuations in Elastic Turbulence over a Wide Range of Polymer Concentrations," Physical Review Letters, Vol. 102(12), p.124503.

Jun, Y. and Steinberg, V., 2011. "Elastic Turbulence in a Curvilinear Channel Flow," Physical Review E, Vol. 84(5), p.056325.

Lam, Y.C., Gan, H.Y., Nguyen, N.T. and Lie, H., 2009, "Micromixer Based on Viscoelastic Flow Instability at Low Reynolds Number," Biomicrofluidics, Vol. 3(1), p.014106.

Larson, R.G., 1992, "Instabilities in Viscoelastic Flows," Rheologica Acta, Vol. 31(3), pp.213-263.

Larson, R.G., Shaqfeh, E.S.G. and Muller, S.J., 1990, "A Purely Elastic Instability in Taylor-Couette Flow," Journal of Fluid Mechcanics, Vol. 218, pp.573-600.

Lee, S., Lee, H.Y., Lee, I.F. and Tseng, C.Y., 2004, "Ink Diffusion in Water," European journal of physics, 25(2), p.331.

Li, D.Y., Li, X.B., Zhang, H.N., Li, F.C., Qian, S. and Joo, S.W., 2017, "Efficient Heat Transfer Enhancement by Elastic Turbulence with Polymer Solution in a Curved Microchannel," Microfluidics and Nanofluidics, Vol. 21(1), p.10.

Li, F.C., Kinoshita, H., Li, X.B., Oishi, M., Fujii, T. and Oshima, M., 2010, "Creation of Very-Low-Reynolds-Number Chaotic Fluid Motions in Microchannels using Viscoelastic Surfactant Solution," Experimental Thermal and Fluid Science, Vol. 34(1), pp. 20-27.

Li, F.C., Oishi, M., Kawaguchi, Y., Oshima, N. and Oshima, M., 2007, "Experimental Study on Symmetry Breaking in a Swirling Free-Surface Cylinder Flow Influenced by Viscoelasticity," Experimental Thermal and Fluid Science, Vol. 31(3), pp.237-248.

Li, X.B., Oishi, M., Matsuo, T., Oshima, M. and Li, F.C., 2016a, "Measurement of Viscoelastic Fluid Flow in the Curved Microchannel Using Digital Holographic

Microscope and Polarized Camera," Journal of Fluids Engineering, Vol. 138(9), p.091401.

Li, X.B., Oishi, M., Oshima, M., Li, F.C. and Li, S.J., 2016b, "Measuring Elasticity-Induced Unstable Flow Structures in a Curved Microchannel Using Confocal Micro Particle Image Velocimetry," Experimental Thermal and Fluid Science, Vol. 75, pp.118-128.

Ligrani, P.M. and Hedlund, C.R., 2003, "Experimental Surface Heat Transfer and Flow Structure in a Curved Channel with Laminar, Transitional, and Turbulent flows," Journal of Turbomachinery (Transactions of ASME), Vol. 126(3), pp. 414-423.

Ligrani, P.M. and Niver, R.D., 1988, "Flow Visualization of Dean Vortices in a Curved Channel with 40 to 1 Aspect Ratio," The Physics of Fluids, Vol. 31(12), pp.3605-3617.

Ligrani, P.M., Choi, S., Schallert, A.R. and Skogerboe, P., 1996, "Effects of Dean Vortex Pairs on Surface Heat Transfer in Curved Channel Flow," International Journal of Heat and Mass Transfer, Vol. 39(1), pp.27-37.

Ligrani, P.M., Copeland, D., Ren, C., Su, M., and Suzuki, M., 2018, "Heat Transfer Enhancements from Elastic Turbulence Using Sucrose-Based Polymer Solutions," Journal of Thermophysics and Heat Transfer, Vol. 32(1), pp.51-60.

Liu, Y. and Steinberg, V., 2010a, "Molecular Sensor of Elastic Stress in a Random Flow," Europhysics Letters, Vol. 90(4), p.44002.

Liu, Y. and Steinberg, V., 2010b, "Stretching of Polymer in a Random Flow: Effect of a Shear Rate," Europhysics Letters, Vol. 90(4), p.44005.

McKinley, G. H., Pakdel, P. and Oztekin, A., 1996, "Rheological and Geometric Scaling of Purely Elastic Flow Instabilities," Journal of Non-Newtonian Fluid Mechanics. Vol. 67, pp.19-47.

Meulenbroek, B., Storm, C., Morozov, A.N. and van Saarloos, W., 2004, "Weakly Nonlinear Subcritical Instability of Visco-Elastic Poiseuille Flow," Journal of Non-Newtonian Fluid Mechanics, Vol. 116(2-3), pp.235-268.

Morozov, A.N. and van Saarloos, W., 2005, "Subcritical Finite-Amplitude Solutions for Plane Couette Flow of Viscoelastic Fluids," Physical Review Letters, Vol. 95(2), p.024501.

Morozov, A.N. and van Saarloos, W., 2007, "An Introductory Essay on Subcritical Instabilities and the Transition to Turbulence in Visco-Elastic Parallel Shear Flows," Physics Reports, Vol. 447(3-6), pp.112-143.

Muller, S.J., Larson, R.G. and Shaqfeh, E.S., 1989, "A Purely Elastic Transition in Taylor-Couette Flow," Rheologica Acta, Vol. 28(6), pp.499-503.

Naschie, M.S.E., Athel, S.A. and Kapitaniak, T., 1992, "A Note on Elastic Turbulence and Diffusion," Journal of Sound and Vibration, Vol. 155(3), pp. 515-522.

Ottino, 1989, "The Kinematics of Mixing: Stretching, Chaos and Transport," Cambridge University Press.

Pamies, R., Cifre, J.G.H., Martínez, M.D.C.L. and De la Torre, J.G., 2008, "Determination of Intrinsic Viscosities of Macromolecules and Nanoparticles. Comparison of Single-Point and Dilution Procedures," Colloid and Polymer Science, Vol. 286(11), pp.1223-1231.

Pan, L., Morozov, A., Wagner, C. and Arratia, P.E., 2013, "Nonlinear Elastic Instability in Channel Flows at Low Reynolds Numbers," Physical Review Letters, Vol. 110(17), p.174502.

Pathak, J.A., Ross, D. and Migler, K.B., 2004, "Elastic Flow Instability, Curved Streamlines, and Mixing in Microfluidic Flows," Physics of Fluids, Vol. 16(11), pp.4028-4034.

Qin, B. and Arratia, P.E., 2017, "Characterizing Elastic Turbulence in Channel Flows at Low Reynolds Number," Physical Review Fluids, Vol. 2(8), p.083302.

Qin, B., Salipante, P.F., Hudson, S.D. and Arratia, P.E., 2019a, "Flow Resistance and Structures in Viscoelastic Channel Flows at Low Re," submitted manuscript.

Qin, B., Salipante, P.F., Hudson, S.D. and Arratia, P.E., 2019b, "Upstream Vortex and Elastic Wave in the Viscoelastic Flow around a Confined Cylinder," submitted manuscript.

Rao, M.A. and Tattiyakul, J., 1999, "Granule Size and Rheological Behavior of Heated Tapioca Starch Dispersions," Carbohydrate Polymers. Vol. 38(2), pp.123-132.

Schiamberg, B.A., Shereda, L.T., Hu, H. and Larson, R.G, 2006, "Transitional Pathway to Elastic Turbulence in Torsional, Parallel-Plate Flow of a Polymer Solution," Journal of Fluid Mechanics, Vol. 554, pp. 191-216.

Shaqfeh, E.S., 1996, "Purely Elastic Instabilities in Viscometric Flows," Annual Review of Fluid Mechanics, Vol. 28(1), pp.129-185.

Sousa, P.C., Pinho, F.T. and Alves, M.A., 2018, "Purely-Elastic Flow Instabilities and Elastic Turbulence in Microfluidic Cross-Slot Devices," Soft Matter, Vol. 14(8), pp.1344-1354.

Sunthar, P., 2010, "Polymer Rheology," Rheology of Complex Fluids, Springer, New York, NY, pp. 171-191.

Tai, J., and Lam, Y.C., 2019, "Elastic Turbulence of Aqueous Polymer Solution in Multi-Stream Micro-Channel Flow," Micromachines, Vol. 10(2), p.110.

Tai, J., Lim, C.P. and Lam, Y.C., 2015, "Visualization of Polymer Relaxation in Viscoelastic Turbulent Micro-Channel Flow," Scientific Reports, Vol. 5, p.16633.

Traore, B., Castelain, C. and Burghelea, T., 2015, "Efficient Heat Transfer in a Regime of Elastic Turbulence," Journal of Non-Newtonian Fluid Mechanics, Vol. 223, pp. 62-76.

Whalley, R.D., Abed, W.M., Dennis, D.J.C. and Poole, R.J., 2015, "Enhancing Heat Transfer at the Micro-Scale Using Elastic Turbulence," Theoretical and Applied Mechanics Letters, Vol. 5, pp. 103-106.

Yasuda, K., Armstrong, R.C. and Cohen R. F., 1981, "Shear Flow Properties of Concentrated Solutions of Linear and Star Branched Polystyrenes," Rheologica Acta, Vol. 20(2), pp.163-178.

Zimm, B.H., 1956, "Dynamics of Polymer Molecules in Dilute Solution: Viscoelasticity, Flow Birefringence and Dielectric Loss," Journal of Chemistry Physics, Vol. 24(2), pp.269-278.